



Device characteristics and material developments of indoor photovoltaic devices



Addanki Venkateswararao^a, Johnny K.W. Ho^b, Shu Kong So^{b,**}, Shun-Wei Liu^{c,d,***}, Ken-Tsung Wong^{a,e,*}

^a Department of Chemistry, National Taiwan University, Taipei 10617, Taiwan

^b Department of Physics and Institute of Advanced Materials, Hong Kong Baptist University, Kowloon Tong, Hong Kong, China

^c Department of Electronic Engineering, Ming Chi University of Technology, New Taipei City 24301, Taiwan

^d Organic Electronics Research Center, Ming Chi University of Technology, New Taipei City 24301, Taiwan

^e Institute of Atomic and Molecular Science, Academia Sinica, Taipei 10617, Taiwan

A B S T R A C T

Indoor photovoltaics (IPVs), which convert the indoor light energy into direct electricity, have attracted research attention due to their potential use as an excellent amicable solution of sustainable power source to drive low-power-needed sensors for the internet of things (IoT) applications. Our daily life adopts various indoor light sources, such as indirect sunlight, incandescent lamps, halogen lamps, fluorescent lamps, and LED bulbs, that typically deliver lower light intensity (200–1000 lux) as compared to that of sun light (~100,000 lux). In this review, we firstly classified the indoor lights depending on their working mechanism and resulting emission spectrum. Because the indoor light intensities are rather low that may lead to overestimate/underestimate the power conversion efficiency (PCE) of IPV devices, then, the cautious points for correctly measuring the indoor light intensity as well as the device characteristics are summarized. Several light sources with various light intensities are reported so far, but for lack of common or standard calibration meter that induces a ambiguity in PCE determination, so we suggest/propose to use a universal LED lux meter with NIST-traceable calibration (e.g. Extech LT40-NIST) and also recommended the device results are expressed in maximum power point P_{max} along with PCE values. It is generally believed that the materials play key roles on the performance of the IPV devices. Since the indoor light intensity is much weaker as compared to that of outdoor irradiation, the typical inferior photo-stability of organic materials under sunlight may not be as crucial as we considered to harvest indoor light energy, opening a great room for organic IPV material developments. In principle, all materials for outdoor PVs may also be useful for IPVs, but the fundamental material requirement for IPVs which needs sufficiently covering the absorption range between the 350–700 nm with high molar extinction coefficient should be primarily concerned. In order to get the thorough knowledge of materials for achieving better efficient IPVs, the reported IPVs were collected and summarized. According to these reports, the materials utilized for IPVs have been classified into two major groups, inorganic and organic materials, then divided them into several sub-classes, including (1) silicon and III-V semiconductor photovoltaics, (2) dye-sensitized photovoltaics, (3) organic photovoltaics, and (4) perovskite-based photovoltaics, depend on their structural nature and device working

Abbreviations: -A, electron acceptor; AM1.5 G, air mass 1.5 global; ANSI, American National Standards Institute; BHJ, bulk heterojunction; CCT, correlated color temperature; CFL, compact fluorescent lamp; CIE, Commission Internationale de l'Eclairage (International Commission on Illumination); CSIRO, Commonwealth Scientific and Industrial Research Organisation; D, electron donor; DSSC, dye-sensitized solar cell; e-h, electron-hole; ETL, electron-transporting layer; V_{OC} , open circuit voltage; J_{SC} , short circuit current density; FF, fill factor; R_{sh} , shunt resistance; R_s , series resistance; P_{in} , incident power intensity; P_{out} , output power; NIST, National Institute of Standards and Technology; V_{max} , maximum power; PVs, photovoltaics; FTO, fluorine-doped tin oxide; HOMO, highest occupied molecular orbital; HTL, hole-transporting layer; IoT, internet of things; IPVs, indoor photovoltaics; IR, infrared; ITO, indium tin oxide; LED, light-emitting diode; LUMO, Lowest unoccupied molecular orbital; MPP, maximum power point; MPPT, maximum power point tracking; NIR, near infrared; NREL, National Renewable Energy Laboratory; OLED, organic light-emitting diode; OSC, organic solar cell; PCE, power conversion efficiency; PSC, perovskite solar cell; PV, photovoltaic; QS, quasi-solid-state; SMCF, spectral mismatch correction factor; SPD, spectral power distribution; SQ, Shockley-Queisser; SSL, solid-state lighting; UV, ultraviolet; UV-vis, ultraviolet-to-visible

* Corresponding author at: Department of Chemistry, National Taiwan University, Taipei 10617, Taiwan.

** Corresponding author at: Department of Physics and Institute of Advanced Materials, Hong Kong Baptist University, Kowloon Tong, Hong Kong, China.

*** Corresponding author at: Department of Electronic Engineering, Ming Chi University of Technology, New Taipei City 24301, Taiwan.

E-mail addresses: skso@hkbu.edu.hk (S.K. So), sqliu@mail.mcut.edu.tw (S.-W. Liu), kenwong@ntu.edu.tw (K.-T. Wong).

principle. For every individual class, the structure-property-efficiency relationship of the materials was analyzed together with the highlights on the best efficiency material, challenge and perspective. For inorganic IPV materials, III-V semiconductor GaAs-based IPVs performed a very impressive PCE (28%). For dye sensitizers, there are more flexible strategies to modulate the absorption profiles of organic materials. A high efficiency dye-sensitized solar cell (DSSC)-based IPV with a PCE up to 32% has been successfully realized with co-sensitized dyes. For organic solar cell (OSC)-based IPVs, fullerene-based acceptors are advantageous for their well-matching desired absorption range and superior electron transport features. A recent OSC-based IPV with the active layer composed of dithienobenzene-based donor and fullerene acceptor was reported to deliver a PCE of 28%. Among these emerging photovoltaic materials, it is no doubt that perovskites (e.g. $\text{CH}_3\text{NH}_3\text{PbI}_3$) are superior for solar energy conversion due to the crystallinity for good charge transport, better spectral coverage and the low exciton binding energy. Until very recent, a perovskite-based IPV with a PCE of 35% was reported with good stability by the incorporation of an ionic liquid for effectively passivating the surface of the perovskite film, indicating the bright prospect of perovskite for IPV application. Overall, the review on these reports implies the essential criteria of materials suitable for IPVs that may trigger new ideas for developing future champion materials for various devices and the realization of practical IPV applications.

1. Introduction

The internet of things (IoT) technology is optimistically expected to benefit our daily life quality with various smart ways. The success of IoT technology will strongly rely on the function and number of end nodes (sensors and actuators), which detect the conditions of environment and/or appliances and communicate each other and/or link to gateway by wireless network [1–10]. The usage of IoT end nodes would expect to reach tens of billions by the end of this decade (2020). Even though they are designed to operate periodically and consume low power (microwatt to milliwatt), however, the long-term power supply without cautious care and maintenance is a quite challenging task, which is the crucial factor for the success of IoT technology. In this regard, the combined “energy-harvesting system” for collecting environmental light, mechanical and thermal energy is anticipated to serve as alternative power supply of currently dominated power source from battery. Along this line, high efficiency indoor photovoltaics (IPVs), which harvest the ambient light energy from day light and/or indoor illumination will be an excellent and amicable solution for providing sustainable power to drive these devices [11–13]. The utilization of IPVs can drastically reduce the maintenance cost of installed indoor electronic devices. Thus, the developments of IPVs are emerging as an important technology suited for IoT applications, household and various electronic applications.

Importantly, IPVs can effectively convert ambient light coming from the direct or indirect day light from sunlight, however, the reliable ambient lightings of building or office environment are from electrically powered light sources such as incandescent lamp, fluorescent lamps, compact fluorescent lamp (CFL), halogen lamps and light emitting diode (LED) bulbs, and so on [14]. These reliable indoor light sources are in different emission spectra, typically covering only visible region, and 100–1000 times lower intensity as compared to standard sun conditions (100 mW cm^{-2} or 1-sun AM1.5 G). To better understand about light sources for IPV applications, the detailed classifications, characteristics and mechanisms of various indoor lightings are summarized in Section 2 of this review. For comparison, the emission spectra of indoor light sources along with solar spectrum are shown in Fig. 1. It is obvious that the emission spectrum of incandescent lamp covers a wide range of visible wavelength and extends to the near infrared (NIR) range, therefore, the material of IPV designed for harvesting the light energy of incandescent lamp needs to consider the spectral response up to NIR range. However, from the energy saving point of view, fluorescent lamps and LEDs currently attract significant interests and dominate over incandescent lamps in the market. The emission spectra of fluorescent lamps and LED-based lights are mainly covering on the visible region, which provides a great opportunity of developing IPVs employing wide band gap materials.

Till date, several types of IPVs responding to different indoor light sources of various intensities and emission spectra are reported. Though

outdoor solar cells have one standard solar condition (AM1.5 G or 100 mW cm^{-2}), however, till now no standard condition was set for the IPVs, but a number of light sources were used to determine the power conversion efficiency (PCE) of focused IPVs [15]. In a general comparison, the maximum power point (P_{\max}) of indoor devices are lower than the outdoor devices under direct sunlight. The main difference between the IPVs and outdoor solar cells coming from the measurement errors such as spectral mismatch error, sweep time effect, and light-soaking effects [16]. Therefore, how to precisely measure the efficiency of IPVs is extremely important. The focused issues addressing these concerns will be presented in the Section 2.2.

Currently, it has been estimated that around 20% of global electricity was consumed by lighting sources, which can be used not only to create high quality indoor illumination, but also provide a potential indoor light energy for driving lower-power demanded devices [17]. The selection of a particularly interested IPV for indoor light sources is of utmost important and vice versa, and is quite a challenging task for researchers. In general, the power available from the indoor lighting is very low ($100 \mu\text{W}$). So the fabrication of limited size IPVs with ultra-low power circuits as well as maximum power point tracking (MPPT) method extracting maximum power from ambient lighting is highly desired [18,19]. Therefore, new approaches for the developments of IPVs should be implemented not only in material designs but also for device configurations. Fortunately, since the intensity of indoor light is much weaker as compared to that of outdoor sunlight, the inferior photo-stability of organic materials may not be as crucial as we typically considered for conventional photovoltaics (PVs). This opens a great space for introducing organic functional materials into this field. In principle, all materials for outdoor PVs may also be useful for IPVs,

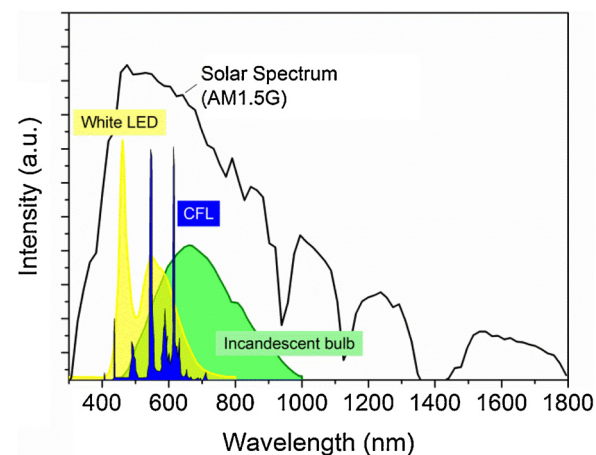


Fig. 1. The emission spectra of the indoor light sources and standard solar spectrum. Adapted from ref. [14].

but there are some fundamental requirements for IPV materials. Particularly, in contrast to materials with NIR absorption for outdoor PVs, materials covering the absorption range between 350–700 nm with high molar extinction coefficient are sufficiently potential candidates for IPVs [11–13]. Materials with the longer wavelength absorption (> 700 nm) are additional since the indoor irradiance, except for incandescent lamp, is out of this region.

Depending on the nature of materials, they were basically inorganic, organic and organometallic materials used for various types of photovoltaic techniques. In the case of inorganic semiconductors, both silicon and III-V semiconductor-based solar cells are mostly popular. Since the first silicon-based solar cell was reported in 1941, substantial researches have been done on this technology to attain a continuously improvement of the PCE [20]. After various improvements/modifications and device engineering on fabrication process, crystalline silicon-based PVs had achieved a very high PCE of 26% under standard solar conditions [21]. It is nature to extend this type of PVs for harvesting the indoor light energy. In early 1970s, amorphous silicon has been started to use as IPVs for powering watches and calculators via harvesting the ambient light energy [22]. However, the production cost and tedious purification of Si in conjunction with the moderate device performance, stimulated the developments of the new era materials for photovoltaic technologies. The current status of Si-based IPVs together with new developments of inorganic semiconductors for IPVs will be highlighted in Section 3.1.

Nowadays, in addition to crystalline/poly-crystalline silicon-based solar cells, which share the majority current PV market, the other emerging technologies such as dye-sensitized solar cells (DSSCs), organic solar cells (OSCs) and perovskite solar cells (PSCs) have gained immense research attentions due to the potential advantages such as low cost, light weight, flexible, transparent, low fabrication temperatures, and particularly short energy payback times [23]. In contrast to inorganic silicon and III-V semiconductors, organic materials attracted particular attention because of their tunable optical and electronic properties, which can be subtly manipulated by various suitable molecular designs. By a suitable modification on end/terminal groups or molecular core skeletons, organic materials can be used as photoactive materials in various PV technologies. For example, dye sensitizer for DSSCs, donor or acceptor of active blend for OSCs, and hole-transferring layer (HTL) or electron-transporting layer (ETL) in PSCs. The materials with required properties for these emerging photovoltaic techniques are different/specific. For each one, their structural/photophysical properties, molecular interactions/packing and morphology need specifically tune in order to achieve promising performance. Among these new PV technologies, DSSCs attracted worldwide attention since the breakthrough made by Grätzel in 1991 [24]. The PCE of DSSCs steadily increased from 7.9% to a recent 14.3% under standard solar AM1.5 G conditions [25]. The dyes suitable for DSSCs typically exhibit strong absorbance in the visible light range, which is highly beneficial for their IPV applications. For giving the absorption ranging between 350 and 700 nm requires the molecule with limited molecular π -conjugation, which will reduce the synthetic complexity for constructing the desired dyes. In addition, smaller dyes with compact packing on TiO_2 will limit the flexibility of anchoring modes, which can effectively reduce electron recombination processes, leading to higher efficiency. Grätzel and co-workers successfully made indoor DSSC for the first time by using N719 dye [26]. After then, the PCE of DSSCs for indoor light energy harvesting was significantly improved. Recently, Grätzel and co-workers used a judicious combination of co-sensitized dyes (XY1b:Y123, Section 3.2), which help to broad the ultraviolet-to-visible (UV-vis) spectral coverage, along with dye-impregnated mesoscopic TiO_2 films attached with porous paper to avoid direct contact between PEDOT counter electrode and redox electrolyte. The resulting new generation co-sensitized DSSC produced the highest record PCE of 31.80% under a white fluorescent light of 1000 lx illumination [27]. When DSSCs and silicon solar cells illuminated with the same indoor

lighting, both devices produce the similar short circuit current density (J_{SC}), but DSSC showed higher overall outputs due to their high band gap, which is beneficial for obtaining higher open circuit voltage (V_{OC}) of ~ 0.65 V as compared to that V_{OC} (0.3–0.4 V) of silicon-based solar cells [28,29]. Although there is critical issue on the liquid electrolyte for long-term use, nevertheless, the solid state and flexible DSSC are under extensive investigations for conquering such challenge as well as getting higher PCE for possible commercialization, rendering the future of DSSC for IPV application feasible. The developments of DSSC-based IPVs will be summarized in Section 3.2.

On the other hand, OSCs employing the bulk heterojunction (BHJ) of organic electron donor and electron acceptor as active layer have gained enormous research interests due to their advantages such as lightweight, low cost, transparent, colorful, flexible and large panels, and easy fabrication with cost-effective production, as compared to those of solar cells using silicon and GaAs. There are many groups working on the development of donor and/or acceptor as well as device engineering for creating high efficiency OSCs. Since the first report made by Tang on bilayer OSC, the PCE steadily increases from 1% to higher than 14%, even more a PCE up to 16.5% was reported recently [30–39]. Beyond the application for solar energy harvesting, indoor OSCs also gain great research interest, particularly aim for self-powering IoT. Therefore, the number of reports on OSCs for ambient light harvesting increases quickly. For indoor OSCs, the active blend absorption should have cover the indoor lighting, in addition to exhibit nanophasse separation and appropriate crystalline size of donor and/or acceptor for the efficient diffusion of exciton as well as the balance of charge carrier transportation. In spite of innovative molecular design ideas, feasible approaches that enable organic materials to form appropriate crystalline sizes together with face-on morphology in active layer for enhancing shunt resistance (R_{SH}) and then high V_{OC} are highly desired [11–13]. As compared to DSSCs, OSCs enable the flexibility for tuning donor and/or acceptor units of active layer, giving more spaces for improving the ultimate efficiency. There are some suspicious issues that dim the future of OSCs, particularly the photo-stability of organic materials as well as device under continuous light soaking. However, as just mentioned, the intensity of indoor lighting is significantly lower as compared to sunlight, therefore, the photo-bleaching of organic active layer is no longer a big issue as we consider OSCs for IPV applications [40,41]. The first report of OSC for IPV application was disclosed by Minnaert and co-workers, using P3HT:PCBM as an the active layer under 500 lx of a LED light illumination [40,41]. They concluded that the BHJ OSCs are well suited for IPVs and showed a relatively higher PCE of 27% for single junction OSC and 70% for tandem OSCs as compared with standard silicon solar cell under the same illumination conditions [40]. After then, the PCE was improved by Tsoi and co-workers with an active layer composed of dithienobenzene-based donor (BTR) and fullerene acceptor (PC71BM), the current case has reached to a PCE of 28% under a fluorescent lamp (1000 lx) illumination [42]. Considering the organic composition and environmental benign fabrication process of OSCs, the role-play of OSCs in IPV applications should be eye-catching if the PCE and stability could be continuously improved. The materials and progresses of OSC-based IPVs will be summarized in Section 3.3.

Recently, organic-inorganic hybrid perovskites are emerging as excellent light harvesting materials mainly attributed to their high extinction coefficient, long charge carrier diffusion length, high carrier mobility, low cost fabrication and high PCEs [43]. Most of perovskite-based PVs adopt an organometallic active material with $CH_3NH_3PbI_3$ configuration, mainly due to the crystallinity and stability issues together with better spectral coverage matching with solar radiation [44–46]. In contrast to OSCs, in which the exciton with binding energy < 50 meV which is close to room temperature thermal energy, perovskites typically exhibit very low exciton binding energy [47]. In addition, perovskites are feasibly to act as an ambipolar material that can smoothly transport both hole and electron to counter electrodes

either with conventional or inverted configuration. Although, PSCs are suffering from the energy loss of exciton migration and dissociation, but they possess lower geminate recombination and thus produce high photocurrent density. The PCE was drastically improved from 3.8% in 2009 to a recent 23.2% [48,49]. These perovskite materials are soluble in polar solvents, which limit the progress of solution processing until a breakthrough made by Grätzel using perovskite layer in combination with Spiro-MeOTAD as HTL for producing a PCE of 10.9% [50]. After then, many research endeavors devote to make high crystallinity of perovskite film, to develop strategies for conquering the low stability and degradation of device, which are generally believed the bottleneck towards commercialization [46]. There is always a serious concern about the water-soluble issue of Pb ion of perovskite. In this regard, researchers trigger the activity to develop Pb-free perovskite materials to reduce the potential toxicity by incorporating Cs, Sn, Ge, etc. as alternative metal ion of perovskite, which can also extend the absorption and decrease the band gap of the material. Among various physical characteristics of perovskites, the low exciton binding energy is particularly interesting, which should be advantageous for indoor applications. Definitely, there are more opportunities of utilizing perovskites for IPVs after adjusting the physical characteristics by tuning the composition of $\text{CH}_3\text{NH}_3\text{PbX}_3$. For example, using X = Br or Cl can shift the absorption to shorter wavelength, or partially replacing CH_3NH_3^+ with different organic or inorganic cations [46]. The first work of PSC

for IPV application was reported by Lin and co-workers with two-step deposited **PC61BM** as ETL, achieving a high V_{OC} of 0.85 V and PCE of 27% under dim light illumination [51]. After then, the progress was significantly improved, the current case has reached to a PCE of 35.2% by Wang and co-workers by incorporating an ionic liquid [BMIM]BF₄ for efficient surface traps passivation and favorable electron extraction and transportation under 1000 lx luminance of a fluorescent lamp illumination [52]. The progress of perovskite-related researches for IPVs will be summarized in Section 3.4.

It is obvious that the progress of IPVs with different aspects of materials is continuously growing. In order to achieve better PCEs and higher stability of IPVs, it is essential to get the thorough knowledge of device characteristics as well as materials developed so far from related reports. In this review, the literatures of IPVs mainly covering on silicon, III-V semiconductors, DSSCs, OSCs, and PSCs are collected and summarized to establish the structure-property-efficiency relationship. The reported IPV materials, are classified into four major groups, in which some of them are divided into several sub-classes depending on their structural nature and properties. The importance of IPV material within individual class is highlighted. The material for giving the best efficiency will be especially emphasized, and then the challenges and perspectives in each class will also be pointed out. From this summarized report, we hope that the researchers can be inspired to have new material design ideas according to the different photovoltaic

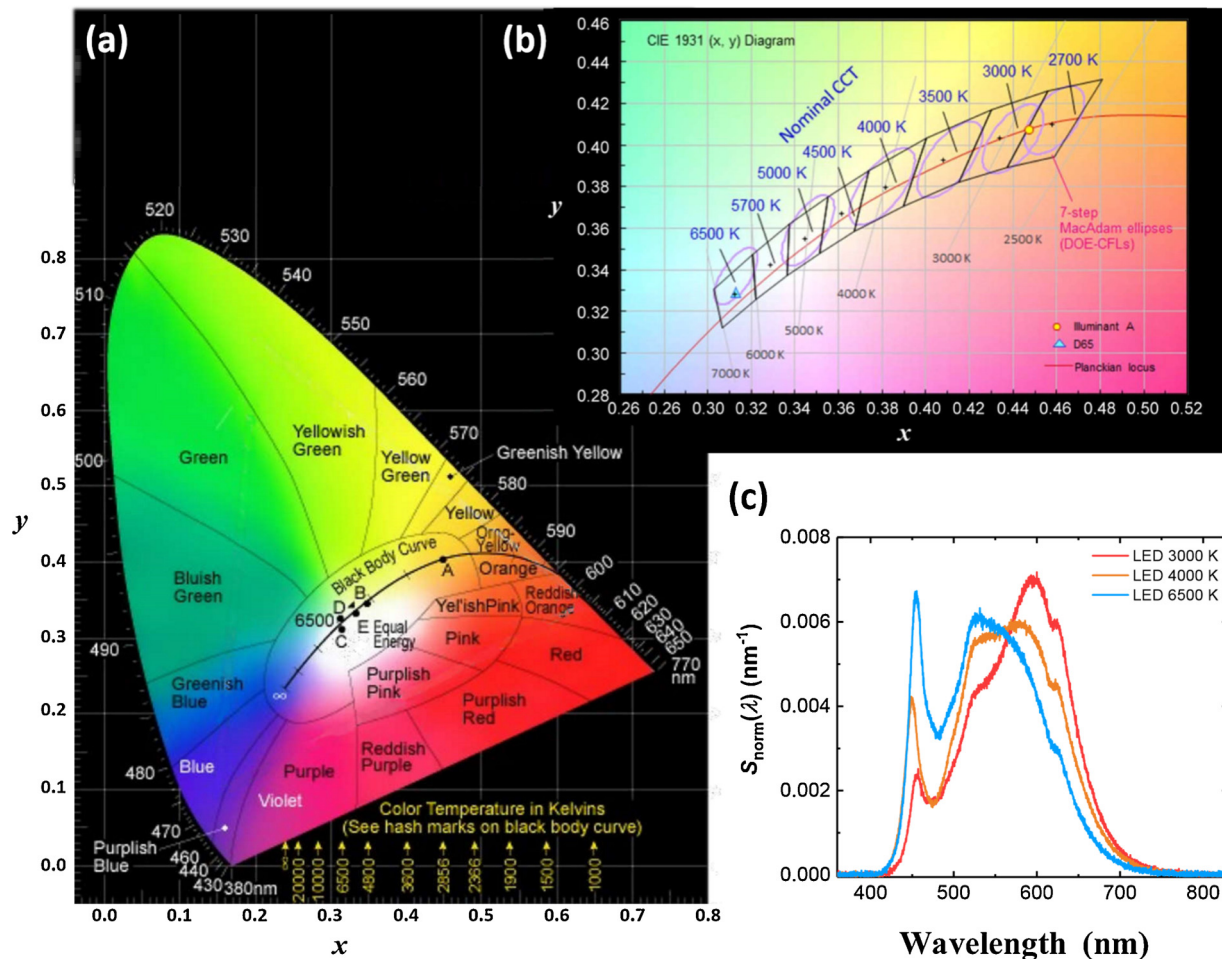


Fig. 2. (a) The CIE 1931 2° chromaticity diagram, with the curved perimeter representing the monochromatic light colors, and a black line (planckian locus) in the region depicting the color of blackbody at different temperatures (also known as (correlated) color temperature, CCT). The diagram is divided into different regions with labelled colors, and the oval-like region at the center is the region of white light. Adapted from ref. [53]. (b) Magnified region of (a) around the planckian locus, with drawn parallelograms representing regions of different CCTs according to the American National Standards Institute (ANSI) standard (C78.377-2001). Adapted from ref. [54]. (c) Spectral power distribution (SPD) of three LED sources with CCTs 3000 K (warm white), 4000 K (natural white) and 6500 K (cool white). Adapted from ref. [55].

technologies for further improving the efficiency and stability of IPVs, rendering the practical applications of this indoor light harvesting technology for IoT feasible.

2. Review of indoor lighting and photovoltaic devices

2.1. Indoor light source classification and features

Since the realization of the first commercialized light bulb by Thomas Edison in 1879, artificial lighting has brought drastic technological advancements, and becomes a necessity in the daily life of human beings. Various forms of lighting have been developed. Domestic lighting nowadays includes incandescent lamps, halogen lamps, fluorescent tubes, CFLs and LEDs. They possess distinct spectral features due to their light production mechanisms and color rendered due to choice of materials. The details of the two classifications are outlined below.

Light sources can be classified by their colors. The color of a light source can be quantified in the CIE (x, y) space [Fig. 2(a)]. [53] The curved boundary, known as the spectral locus, gives the colors of monochromatic light at visible wavelengths. Colored light sources are characterized with the chromaticity coordinates, also known as CCx and CCy values. There is a whitish region in the space, defining the range of colors as "white". The region covers most of the planckian locus, the colors of blackbodies at different temperatures. In light of this, the correlated color temperature (CCT), also conventionally called color temperature, is defined for characterizing white light sources [Fig. 2(b)]. [54] Conventionally, three kinds of color temperature can be seen in domestic light sources: warm white (2700–3000 K), natural white (4000–4500 K) and cool white (5000–6500 K). A higher color temperature gives more bluish light, expecting relatively more emissions at the short wavelength region [Fig. 2(c)]. [55]

The two main light production mechanisms are incandescence and luminescence. Inside an incandescent lamp, a resistively heated metal (usually tungsten) emits thermal radiation. The emitted radiation resembles a blackbody with a characteristic spectral power distribution (SPD) [Fig. 3(a)], [56] featured by a large proportion as high as 90% of infrared (IR) radiation. Therefore, these light sources are often called hot light sources. Traditional incandescent light bulbs and halogen lamps emit light with this mechanism. Household has used incandescent light bulbs for more than 130 years. Halogen lamps give greater lumen output, and are used in areas requiring quality light such as food preparation and display of paintings, products and so on.

In contrast to incandescent lamps, luminescent lamps do not produce light by heat and are often called cold light sources. Cold light sources may produce light by gas discharge, which can be found in fluorescent tubes and CFLs, or by electroluminescence, which can be found in LEDs. For fluorescent tubes and CFLs, light is produced by emission from electronically excited Hg vapor inside the gas discharge tube under an applied voltage, together with the Hg-emission-induced fluorescence generated by phosphors coated on the inner surface of the tube, producing SPDs of characteristic peaks of narrow bands [Fig. 3(a)]. Fluorescent phosphors are employed in fluorescent lamps for converting the UV light to the visible. LEDs produce light through electroluminescence. Electrons and holes flow into the semiconductor junction from the electrodes. A photon is released when an electron and a hole recombine. Light sources with LEDs are also called solid-state lighting (SSL). A single-junction LED emits colored light characteristic to the semiconductor material used, and the corresponding emission spectrum is usually narrow. [57] To make white LEDs, two major approaches may be used. For the most widely used phosphor LEDs, light is produced by emission from a combination of a GaN blue LED and yellow phosphors, giving broad band spectra with peak in the blue region [Fig. 3(a)]. The color temperature can be tuned by adjusting the thickness of the phosphor coating. Alternatively, white light can be generated by RGB LEDs. Here, three LEDs, red, green and blue, are

made in one module, producing white light by means of the additive color method. Usually three distinct peaks can be observed in the SPD [Fig. 3(b)]. [58] Other variations of white LEDs are based on these two approaches of the use of phosphor materials (wavelength converter) and color mixing of individual LEDs, ranging from dichromatic to tetrachromatic sources. It should be noted that all these white LED variants have distinct SPD features from one to another.

2.2. Measurement of incident power intensity

PCE determination involves both the incident and the output powers. The incident power intensity under AM1.5 G is fixed at 100 mW cm⁻². For IPVs, the incident power intensity varies with the illuminance and the indoor light source. For the same model of light source, and with a particular PV device, large variations in PCE have been reported across different laboratories. The variations can be traced to different reported incident power intensities even though the same model of light source and illuminance was specified. [59] Accurate indoor PCE calculation, therefore, requires reliable incident power measurement.

Indoor lighting is artificially designed for human vision. The brightness of an indoor light source is subject to visual perception of human eyes. Therefore, it is necessary to quantify brightness with photometric quantities which is weighed by the spectral sensitivity of human vision instead of radiometric quantities. A measure of brightness is illuminance, also known as luminous flux intensity, with the SI unit lux (lx). Naturally, lux becomes a specification of performance evaluation conditions for IPV devices. Nonetheless, PCE calculation for an IPV cell requires knowledge of the incident power intensity, in W cm⁻². Therefore, conversion from a measured illuminance L to incident power

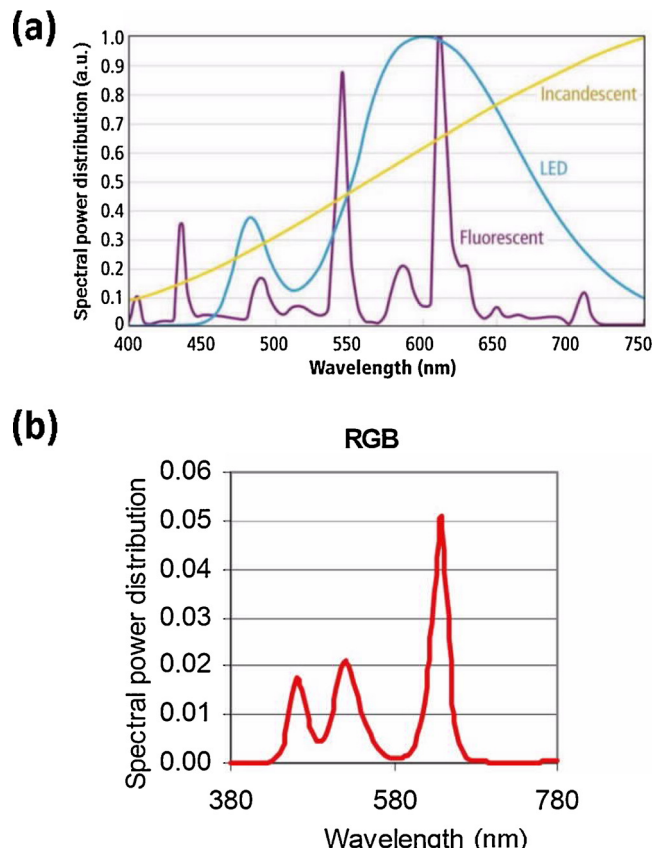


Fig. 3. (a) Relative spectral power distributions (SPDs) of incandescent lamp, fluorescent lamp and phosphor LED. All light sources have a color temperature of 3000 K. Adapted from ref. [56]. (b) SPD of an RGB LED. Adapted from ref. [58].

intensity (P_{in}) is needed for indoor PCE calculation. The conversion can be defined by [55]

$$L = K_r P_{in} \int_{360 \text{ nm}}^{830 \text{ nm}} S_{\text{norm}}(\lambda) V(\lambda) d\lambda \quad (1)$$

where

$$S_{\text{norm}}(\lambda) = \frac{S(\lambda)}{\int_0^{\infty} S(\lambda) d\lambda} \quad (2)$$

is the SPD of the light source $S(\lambda)$ (usually in arbitrary unit) under the normalization condition $\int_0^{\infty} S(\lambda) d\lambda = 1$. $K_r = 683.002 \text{ lm W}^{-1}$ is the maximum spectral luminous efficacy for human photopic vision, and $V(\lambda)$ is the spectral luminous efficiency function for human photopic

vision ($> 5 \text{ lx}$) characterizing the spectral sensitivity of human eyes. [60,61] The range of the integrals from 360 nm to 830 nm in Equation (1) is set according to the definition of $V(\lambda)$, in which the color-matching function of the CIE 1931 2° standard colorimetric observer of 1°–4° field of view is adapted. It is the standard for most commercially available photometric instruments. [62–65] The denominator in Equation (2) is the normalization constant for $S(\lambda)$, separating the magnitude of the power intensity from the relative spectral features. A scheme of P_{in} determination is given in Fig. 4 and described as follows.

$S(\lambda)$ can be measured by a spectroradiometer. The area A under $S(\lambda)$ from 360 to 830 nm is calculated. Then $S(\lambda)$ is divided by A to get $S_{\text{norm}}(\lambda)$. During PV measurement, a calibrated lux meter is placed at the device position. The target illuminance can be obtained by

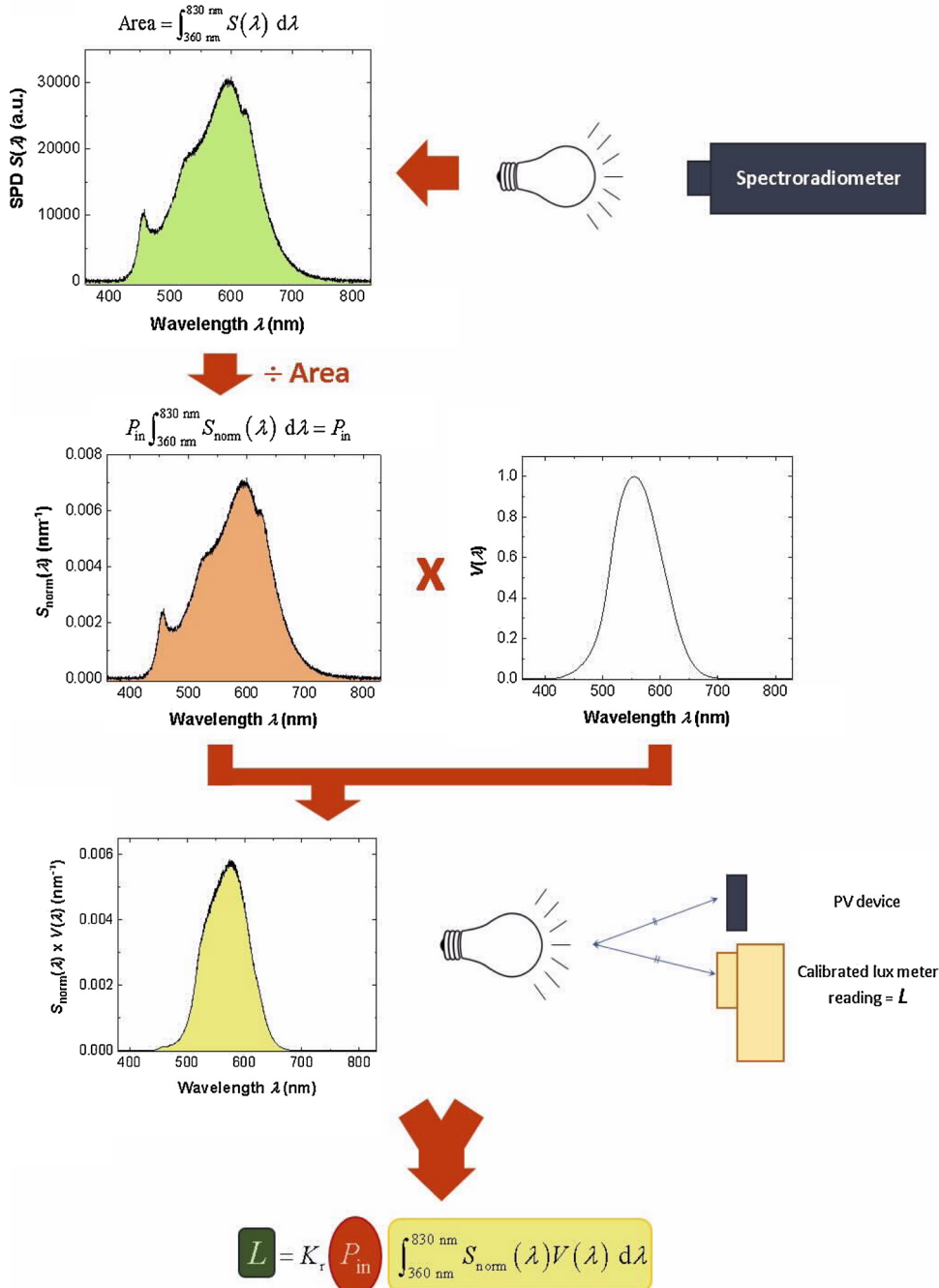


Fig. 4. A calculation scheme of determining incident power intensity of a light source P_{in} from the illuminance reading L of a calibrated lux meter. The integral filled in yellow is the area under curve in the $S_{\text{norm}}(\lambda) \times V(\lambda)$ plot. (For interpretation of the references to colour in this figure legend, the reader is referred to the web version of this article).

adjusting the distance between the light source and the lux meter. After that, the device and the light source are fixed for device performance evaluation. As the relative spectral features are invariant to the irradiance under particular operating conditions, $S_{\text{norm}}(\lambda)$ remains unchanged for the same light source. Changing the source-device distance, i.e. L , only alters P_{in} . Then the incident power intensity can be determined. The integral in Equation (1) indicates the degree of matching of the light source SPD to the spectral sensitivity of human vision. The larger the value, the smaller the P_{in} for the same L due to the perception of increased brightness. Therefore, the same illuminance generally corresponds to different P_{in} according to the light source. Previous reports have a wide range of P_{in} -to- L ratio of 25–60 $\mu\text{W cm}^{-2}$ per 100 lx. [13,42,55,66–72] $S(\lambda)$ varies from the type of light source (e.g. fluorescent lamps and LEDs) to the color of the light, or the color temperature for white light sources. Even for the same type of light source and same color temperature, SPD variation across manufacturers and batches can be significant. [73] It can be illustrated by comparing the spectra of two distinct 4000 K fluorescent lamps provided by previous reports [55,74]. Differences in spectral features can be observed, and a P_{in} difference of 16% for the same illuminance is obtained using Equation (1). An even more dramatic, greater than 57% difference is found when comparing the SPDs of another pair of fluorescence lamp sources with the same approach. [55,75] This shows that the value of P_{in} can have great variation owing to its SPD features despite the same lamp type and color temperature. Therefore, prior knowledge of the light source spectrum is highly recommended in order to get a more accurate P_{in} from L . In addition, it is also recommended that the model of the light source, its type, color temperature and SPD as well as the illuminance level should be specified so that comparison of device performance is sensible. Fig. 5 shows a typical example of the incident power intensity as a function of illuminance in the domestic range, i.e. 200–1000 lx [76,77], for fluorescent and LED lamps with different color temperatures. Table 1 provides the numerical values of P_{in} under different illuminances.

Another crucial factor of getting an accurate P_{in} is the determination of L in Equation (1) which is usually measured by a lux meter (also known as photometer, illuminometer and light meter). The general $V(\lambda)$ mismatch index f_1' , which reveals the quality of the lux meter, is usually stated in the specification. [62,78] The f_1' value classifies lux meters into Class L ($< 1.5\%$), A ($< 3\%$), B ($< 6\%$) and C ($< 9\%$) according to the DIN 5032 Part 7 standard. [79] A high quality lux meters usually have small f_1' values [Fig. 6(a)]. At least Class A lux meters are recommended when the spectral mismatch correction cannot be performed. [80] The accuracy of the lux meter reading for a particular light source depends on the instrumentation and its initial calibration during manufacture. As shown in Fig. 6(b), before reaching the detector head, light first passes through an optical filter with a spectral response $s_{\text{rel}}(\lambda)$ to mimic $V(\lambda)$. $s_{\text{rel}}(\lambda)$ usually differs from $V(\lambda)$ and is therefore not perfect. So the lux meter is calibrated to compensate the mismatch between $s_{\text{rel}}(\lambda)$ and $V(\lambda)$. For conventional lux meters, illuminant A, which is a tungsten light source, is used as the calibration source. [81,82] A reading difference of the lux meter from a reference reading would be calibrated with a single scaling factor. However, the calibration factor is only applicable to a particular light source [62,78]. In other words, deviated reading is expected when the lux meter is used for measurement of light sources other than tungsten lamps. The greater the difference of spectra between the light source and the reference standard illuminant, the greater the expected deviation [78,83,84]. Such deviations can be reduced by using a quality lux meter whose $s_{\text{rel}}(\lambda)$ matches $V(\lambda)$ well, characterized by the small f_1' . [62,78] The error of illuminance reading of a Class A lux meter for a broad-band white light source could go down to 2% [82,84]. It should be noted that, however, f_1' serves only as an indicator of the suitability of the lux meter to an arbitrary light source, since f_1' works in principle for tungsten lamp source only. It does not guarantee a good mismatch descriptor for narrow band sources with abrupt spectral slopes as the V

(λ)-mismatch can be large at the particular emission peak even though the overall value is small. [82,85] Significant deviations could be found particularly in the blue-end region [82,86].

To obtain highly reliable lux measurements with the instrumental error of the lux meter removed, the following approaches could be considered. (1) An illuminance spectrophotometer can be used. [87] They measure the light spectrum with the $V(\lambda)$ calculated with the internal software to give the illuminance level [Fig. 6(b)], and thus the accuracy is light source independent. An economic alternative is an LED light meter. LED light meters possess a white LED calibration and gives more accurate lux reading ($< 0.9\%$) compared to a conventional lux meter. [88] A small instrumental error due to spectral diversity of white LED light sources may still persist owing to difference in color temperature and design variations across manufacturers. Since there are a great variety of choices of the white LED sources for calibration, an LED lux meter with NIST-traceable calibration (e.g. Extech LT40-NIST) is recommended [89]. This can ensure the consistency of the lux meter reading across the community, and the difference in P_{in} can then be attributed to difference in light source SPD and measurement techniques. (2) If only a conventional lux meter is available, or illuminance levels have been obtained with a conventional lux meter, the readings could be calibrated with the following procedures. To begin with, the spectral responsivity $s(\lambda)$ of the lux meter is measured. Depending on the procedures, $s(\lambda)$ may be expressed in different units. In lm W^{-1} , $s(\lambda)$ can be expressed as [90,91]

$$s(\lambda) = \frac{L(\lambda)}{S(\lambda)} \quad (3)$$

assuming a linear response of the lux meter. $s(\lambda)$ can be determined by a lamp-monochromator set-up. Light from a test light source of stable, known spectral irradiance [$S(\lambda)$] enters a monochromator and then the lux meter. The detector is overfilled during the measurement and the values of $L(\lambda)$ are recorded. The spectral interval of 5 nm is recommended according to the National Institute of Standards and Technology (NIST). [92] Relative value of $s(\lambda)$ is adequate. More details are available in previous reports. [90,93,94] Then the true illuminance can be calculated by multiplying the lux meter reading to the spectral mismatch correction factor (SMCF), given by [62,78,90]

$$F^* = \frac{s_{\text{cal}}}{s} = \frac{\int_{360 \text{ nm}}^{830 \text{ nm}} S(\lambda) V(\lambda) d\lambda \int_0^\infty S_{\text{cal}}(\lambda) s(\lambda) d\lambda}{\int_{360 \text{ nm}}^{830 \text{ nm}} S_{\text{cal}}(\lambda) V(\lambda) d\lambda \int_0^\infty S(\lambda) s(\lambda) d\lambda} \quad (4)$$

where s_{cal} and s are the luminous responsivities of the lux meter under the calibration light source and the test light source respectively. $S_{\text{cal}}(\lambda)$ is the SPD of the calibration light source for the lux meter. Similar to the

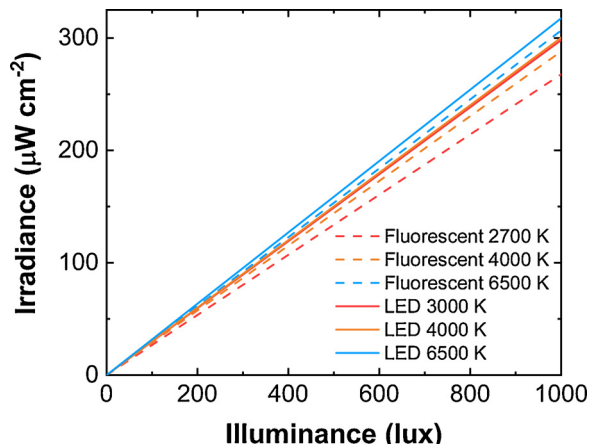
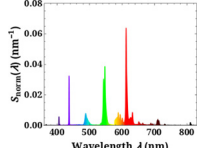
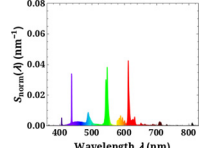
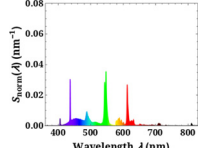


Fig. 5. Irradiance vs illuminance of fluorescent and LED lamps at warm white (2700–3000 K), natural white (4000 K) and cool white (6500 K) color temperatures. The numerical values and the model numbers of the lamps are given in Table 1.

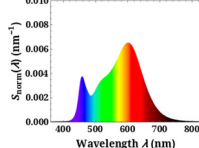
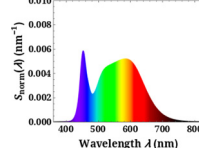
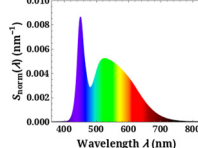
Table 1

Computed values of incident power intensity P_{in} at various illuminance levels for T5 lamp tubes of different color temperatures. The model number (after the “#” symbol), color temperature and normalized emission spectrum of each light source are shown. The color temperature depicted in the format of “nominal/calculated from emission spectrum”. The photopic matching index ϕ for the light sources is included, defined as $\phi = \int_{360 \text{ nm}}^{330 \text{ nm}} S_{\text{norm}}(\lambda) V(\lambda) d\lambda$. The values serve as an example; they may vary according to the light source model and thus are for reference only.

(a) Fluorescent lamps, in conjunction with electronic ballasts (PAK, PAK300408).

Illuminance (lux)	 Warm white (2700/2928 K) #PAK090481 $\phi = 0.5478$ $P_{in} (\mu\text{W cm}^{-2})$		
	 Natural white (4000/4265 K) #PAK090491 $\phi = 0.5090$ $P_{in} (\mu\text{W cm}^{-2})$		
	 Cool white (6500/6400 K) #PAK090501 $\phi = 0.4781$ $P_{in} (\mu\text{W cm}^{-2})$		
100	26.8	28.8	30.7
200	53.5	57.6	61.3
300	80.3	86.4	92.0
400	107.1	115.2	122.7
500	133.8	144.0	153.3
600	160.6	172.8	184.0
700	187.4	201.6	214.7
800	214.1	230.4	245.4
900	240.9	259.2	276.0
1000	267.7	288.0	306.7

(b) LED lamps.

Illuminance (lux)	 Warm white (3000/3328 K) #PAK-LED-T5-4WF-830 $\phi = 0.4920$ $P_{in} (\mu\text{W cm}^{-2})$		
	 Natural white (4000/4624 K) #PAK-LED-T5-4WF-840 $\phi = 0.4883$ $P_{in} (\mu\text{W cm}^{-2})$		
	 Cool white (6500/6994 K) #PAK-LED-T5-4WF-865 $\phi = 0.4618$ $P_{in} (\mu\text{W cm}^{-2})$		
100	29.8	30.0	31.8
200	59.6	60.1	63.5
300	89.4	90.1	95.3
400	119.2	120.1	127.0
500	149.0	150.1	158.8
600	178.8	180.2	190.5
700	208.6	210.2	222.3
800	238.4	240.2	254.0
900	268.2	270.2	285.8
1000	298.0	300.3	317.5

protocol of incident power intensity evaluation as in Equation (1), SMCF is specific to a certain combination of light source and lux meter. Note that the SMCF correction is not applicable when $F^* < 0.5$ or $F^* > 2$ [95], so a sufficiently quality lux meter is still essential. It should be regularly (usually annually) calibrated, and the aging of optical filter which affects the $V(\lambda)$ mismatch should be monitored.

Several conditions set by the Commission Internationale de l'Eclairage (CIE) for standardizing LED lighting product testing reveal possible suggestions for better incident power intensity measurement for PCE evaluation using LED lamps. [96] Stable ambient temperature ($(25 \pm 1.2)^\circ\text{C}$) and little air movement ($< 0.25 \text{ m s}^{-1}$) are stated for reducing irradiance uncertainty. Due to the much more diffused light for indoor illumination compared to the sunlight, the directional response index for illuminance f_2 of the lux meter, which describes the accuracy of the angular responsivity, should be smaller than 15%. Class A or L ($f_1' < 3\%$) lux meters are recommended. Moreover, it is known that certain fluorescent lamps require a warm-up period before the

illuminance becomes steady, and both LED and fluorescent lamps have decreased irradiance due to the hotter junction or ambient temperature. [59,97] So the illuminance level should be regularly checked for confirming stable irradiance during measurement. The diffuse indoor lighting environment implies an appreciable portion of light coming from reflection, and the illuminance level and spectral alternation due to difference between the reflection spectrum and the light source spectrum should be kept invariant. A difference in illuminance level of more than 10% could be observed depending on the reflection environment.

2.3. Device parameters and output power

2.3.1. Limiting efficiency and power output

The classical Shockley-Queisser (SQ) limit predicts the maximum possible efficiency of a single $p-n$ junction PV cell. The limiting efficiency (η_{SQ}) is given by [98]

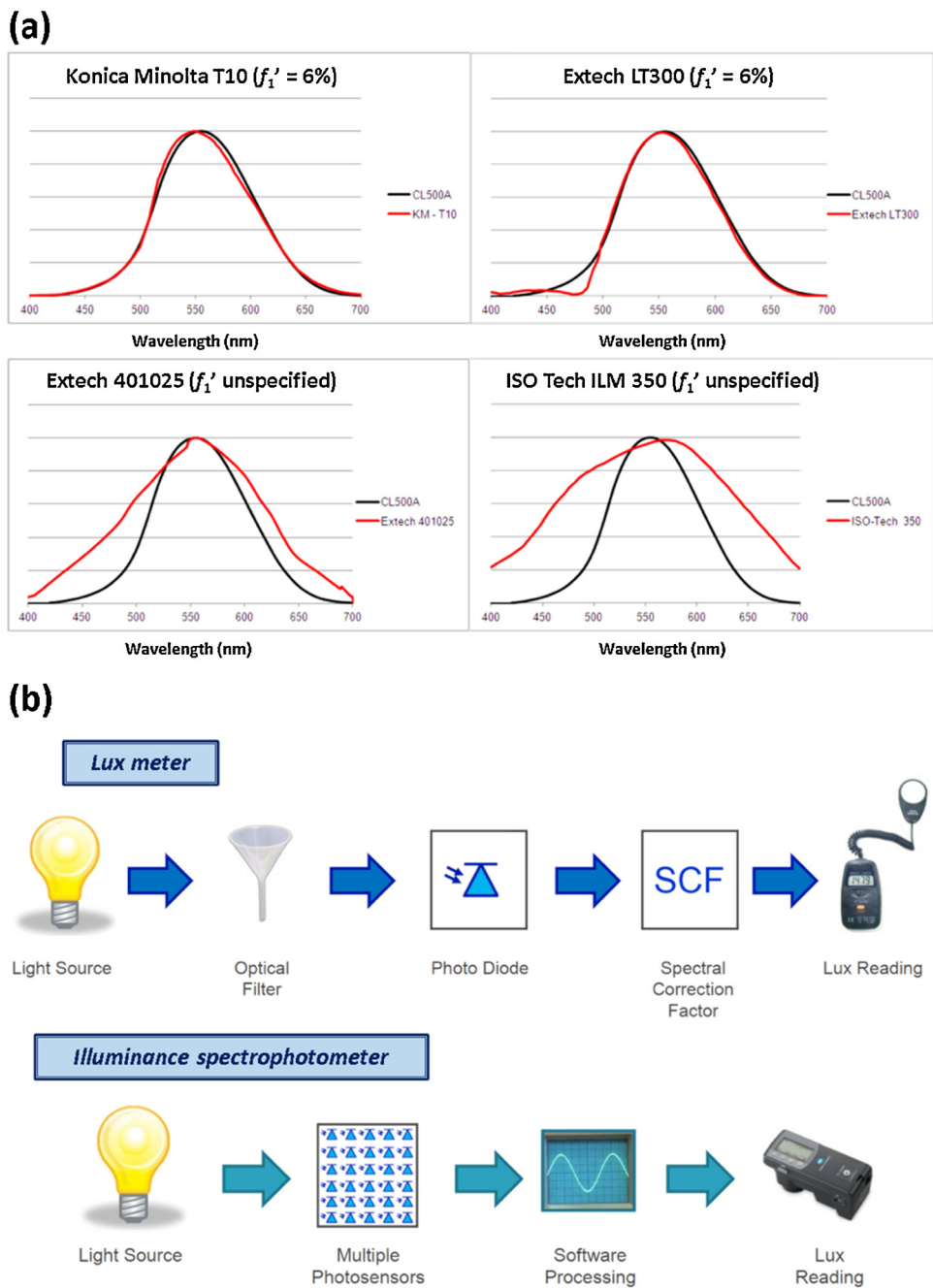


Fig. 6. (a) Relative spectral responsivities $s_{\text{rel}}(\lambda)$ of four lux meters compared to that of the Konica Minolta CL-500A illuminance spectrophotometer. CL-500A possesses an internal computerized spectral responsivity function ensembling $V(\lambda)$ with very good accuracy ($f'_1 < 1.5\%$, Class L). Konica Minolta T10 and Extech LT300 have the same f'_1 value of 6% (Class B). The f'_1 values are unspecified for Extech 401025 and ISO Tech ILM 350. (b) Schematic working principles of a lux meter and an illuminance spectrophotometer. Adapted from ref. [87].

$$\eta_{\text{SQ}} = \eta_u \times \eta_d \times \eta_{\text{FF}}. \quad (5)$$

In Equation (5), η_u is the ultimate efficiency subject to sub-bandgap photon loss; η_d is the detailed-balance efficiency limited by the radiative recombination of the device at nonzero temperatures; η_{FF} is the fill factor (FF) loss due to the non-square diode behavior of the current-voltage characteristics. η_{SQ} can be evaluated by assuming an incoming photon with energy $h\nu$ above the bandgap energy E_g (in eV) excites one and only one electron-hole (e-h) pair. Excess energy ($h\nu - E_g$) is lost due to thermal relaxation of the hot carriers. Radiative recombination in the form of blackbody radiation is regarded as the only unavoidable recombination in this ideal device. Freunek and co-workers reported the maximum efficiencies of IPV devices with various light sources.

[99] One major implication of this is that the efficiency limits of PV devices illuminated by narrow band cold light sources, e.g. fluorescent lamp and phosphor LEDs, can be significantly higher (50–57%) than that under AM1.5 G illumination (~ 30%) (Fig. 7). [100,101] In the case of AM1.5 G, the IR portion of the spectrum contributes only to the incident power but not to the output power (P_{out}), resulting in a maximum $\eta_{\text{SQ}} \approx 30\%$. In addition, the narrower emission band of a cold light source diminishes energy loss due to thermal relaxation of photons of energy greater than the bandgap energy. The absence of IR emission in cold light sources shifts up the optimal bandgap energy from ≈ 1.3 eV to 1.9–2.0 eV. If a PCE ≈ 50% can be achieved and with an illuminance 100–1000 lx, the SQ-limited output power intensity could reach $41 \mu\text{W cm}^{-2}$ at 300 lx, and $136 \mu\text{W cm}^{-2}$ at 1000 lx. The level of

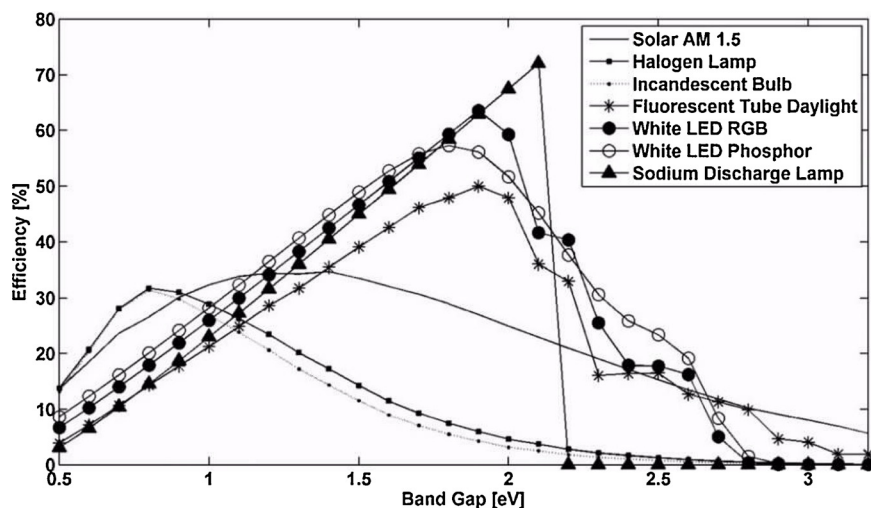


Fig. 7. Shockley-Queisser limiting efficiencies of an ideal photovoltaic converter as a function of bandgap energy E_g under illumination of various light sources. Adapted from ref. [100].

power output should be sufficient to drive different IoT devices. [102] In other words, the visible-only emission of cold light sources could allow for self-powered IoT modules in operation.

2.3.2. Conditions for attaining high performance indoor photovoltaics

The major goal of IPV is to drive standalone, small and off-grid objects like IoT. Therefore, the most important consideration of industrial realization of IPV is the output power and voltage. The greater the efficiency, the larger the output power intensity. In addition, a large output voltage is required to turn on an electrical appliance. This voltage can be taken as the voltage at the point of maximum power (V_{max}) of an IPV cell, where $V_{max} \approx (0.72\text{--}0.78) V_{OC}$. [103] So both optimized PCE and V_{OC} are essential to drive electronic devices. For an organic PV cell, the open-circuit voltage V_{OC} can be described by the empirical relation [104]

$$V_{OC} = \frac{1}{q}(|E_{HOMO}^D| - |E_{LUMO}^A|) - 0.3 \quad (5)$$

where q is the electronic charge, and E_{HOMO}^D and E_{LUMO}^A are energy levels of the highest occupied molecular orbital (HOMO) of the donor material and the lowest unoccupied molecular orbital (LUMO) of the acceptor material respectively. $|E_{HOMO}^D| - |E_{LUMO}^A|$ is known as the effective bandgap energy. So an organic PV material with a larger effective bandgap would be generally favorable for large V_{OC} devices. Realization of a large V_{OC} can be achieved by rational molecular design and synthesis. In contrast, silicon-based IPVs lacks such a freedom for V_{OC} . The maximum voltage output under indoor illumination is ~ 0.4 V. A series of 3 silicon IPV cells is needed to drive IoT objects with input voltage of 1 V or above. It should be noted that, according to Equation (6), when designing IPV devices, not only the bandgap of the donor but also the acceptor should be considered.

To enable large power output, a large J_{SC} is also needed as $P_{out} = VI$. In the SQ limit calculation, a perfect absorber is assumed and all e-h pairs generated dissociate into electric current. In real devices, there is only finite absorption and so the photocurrent is smaller than the ideal, implying possibility of device optimization through improved light absorption. Lee and co-workers demonstrates that P_{max} is directly proportional to illuminance, so is J_{SC} . On the other hand, $V_{OC} \sim \ln L$; the logarithmic dependence implies a much smaller variation of V_{OC} with illuminance. [66] Then it can be induced the strong dependence of P_{max} on J_{SC} . For a certain illuminance, J_{SC} is primarily determined by the absorption of the device. Thus high performance of IPV devices can be achieved by maximizing light absorption with suitable materials. Further discussion will be given in Section 3.

2.3.3. Accurate characterization for indoor photovoltaics

There have been comprehensive discussions about solar cell characterization in the AM1.5 G context for accurate device parameter acquisition. [105,106] Similarly, there is a need of knowledge for accurate parameter measurements in IPV. The significant sweeping time effect in IPV has been demonstrated by Chen and co-workers [59]. For reduced hysteresis, much longer sampling delay time (> 1 s) is required for room light illumination when compared to the AM1.5 G testing conditions (several hundred ms). Strong hysteresis could be observed with short sampling delay time, accompanied by an underestimated V_{OC} and an overestimated J_{SC} , illustrating sweeping rate is a more decisive measurement parameter under indoor lighting. It was explained by the lower charge gradient across the device electrodes, and the electron diffusion coefficient is too small for the charges to respond quickly to the rapidly switching bias voltage, resulting in a longer device response time. It was suggested a wide range of the sampling delay time in both directions should be used during measurement to determine the conditions revealing the true device parameters.

Another issue known in both organic and inorganic solar cells is the light soaking effect. [107–110] In inverted OSCs, light soaking, irradiance given to a device for some time, causes a change of the PV parameters, and is usually associated with an increased conductivity and thus J_{SC} . [111] It is suggested from the studies of the P3HT:PCBM inverted devices that the interaction between the interfaces and UV photons plays a significant role. [112,113] For the indium tin oxide (ITO)/active layer interface, absorbed oxygen at the interface could contribute to the light soaking effect, via either by oxygen plasma or UV treatment. P3HT⁺ radical cations are generated in the process and the adsorbed oxygen on the ITO substrate acts as acceptor dopants for the photoexcited P3HT, removing the electron injection barrier between ITO and PCBM. Symonowicz and co-workers proposed dipole formation at the ZnO/P3HT:PCBM interface as the origin of the light soaking effect for devices with ZnO as the interfacial layer between ITO and P3HT:PCBM [111], leading to a reduced extraction barrier. Both involve a change in the effective electrode work function and improved energy level alignment under light soaking.

The measurement accuracy of perovskite devices is closely related to the sweeping time and light soaking effects from the report by Dunbar and co-workers. [114] They compared the fast-responding and the slow-responding PSCs ($\text{CH}_3\text{NH}_3\text{PbI}_3$), characterized by the time-scale of the metastable response t_s , which is the time required for the current to reach within tolerance of the final steady-state value without degradation. Fast-responding cells have small t_s . Device

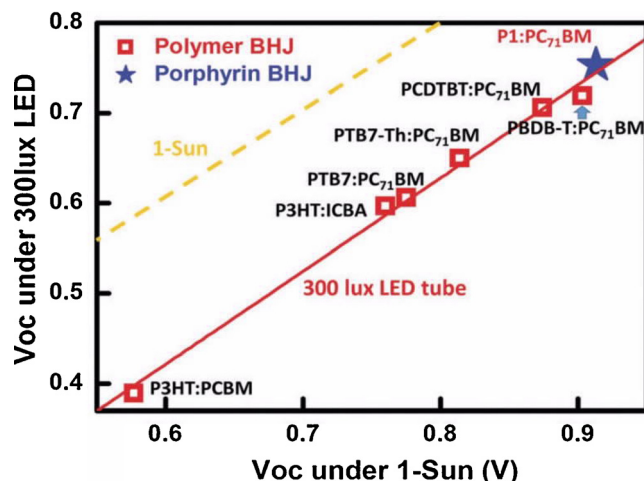


Fig. 8. Correlation plot relating V_{OC} under 300 lux LED (3000 K) illumination (V_{OC}^{room}) and V_{OC} under AM1.5 G (V_{OC}^{sun}). The line of V_{OC}^{room} (red) shows a constant downward offset of 0.17 V from the V_{OC}^{sun} line. Adapted from ref. [116].

characterization was done by two PV performance measurement accredited laboratories, National Renewable Energy Laboratory (NREL) and Commonwealth Scientific and Industrial Research Organisation (CSIRO), as well as eight PV research laboratories and their values were compared. They found a much larger variability for the slow-responding cell (~ 10 times) than the fast-responding cell (1.3 times) compared to that of the silicon cell. In addition, results using various measurement procedures, from pre-conditioning (e.g. light soaking) to scanning rate, were compared. While, for the fast-responding cell, the variability in measurement parameters across different procedures are comparable to that due to device aging, the process of measurement becomes the single dominant factor to the variability of the device parameters for the slow-responding cell. The hysteresis behavior is dominated by the dynamics between the interface trap density and the mobile ions. The dynamic approach of measurement was identified the generally most accurate steady-state measurement given a stable device. During the I - V scan, the cell is kept under illumination, and a point of measurement is taken only when the current at a particular voltage bias is sufficiently stable ($< 0.2\% \text{ min}^{-1}$). The drawbacks of this technique are that it takes a long time and is not applicable to short-lifetime devices. Alternatively, the repeat scan and the V_{max} -soak-fast-scan are considered the most reliable approaches. The repeat scan technique involves device pre-conditioning at open-circuit under ambient room light for 30 min or more, followed by repeatedly scanning the device in one direction at 150 mV s^{-1} until the efficiency becomes stable. The V_{max} -soak-fast-scan pre-conditions the device at the maximum power point (MPP) for 10 min, followed by immediate fast reverse and forward scans at 150 mV s^{-1} . The pre-conditioning manner also affects the device parameters. Light soaking near V_{max} gives the efficiency closest to the steady state measurement. Light soaking at the open-circuit (short-circuit) condition tends to give overestimated (underestimated) efficiencies. Based on the results, they concluded that the optimal measurement technique depends on the t_s value of the device. For small t_s devices, fast scans are preferred for the reduced measurement time as well as minimization of cell heating and fluctuations of irradiance and temperature. For large t_s devices, pre-conditioning is required for prior device stabilization. If the lifetime is short, coarse voltage spacing, or even limited I - V points near the MPP instead of the full I - V profile should be acquired. As a final remark, it is worth noting that the light soaking effect for indoor OSCs and PSCs still lacks detailed investigation, and its significance is to be reviewed.

2.3.4. Device parameters for indoor photovoltaics

One major difference between the sunlight and the IPVs is the

change in illuminance. The typical incident power intensity of indoor light sources is around 300–5000 times smaller than that under the AM1.5 G condition, and the output power intensity of indoor solar cells is 100–1000 times smaller than the sunlight PV devices. Given the greatly reduced output power intensity, it is readily seen that the device parameters, V_{OC} , J_{SC} and FF, should show certain degree of deviation under indoor illumination conditions from those evaluated under AM1.5 G. Since $L \propto P_{in} \propto J_{SC}^\alpha$, where $\alpha \approx 1$ for quality devices [66,115], the value of J_{SC} is lowered with a similar ratio when switching to indoor light sources, i.e. $\sim 10\text{--}100 \mu\text{A cm}^{-2}$. Similarly, V_{OC} under room lighting (V_{OC}^{room}) is smaller than that under AM1.5 G evaluation (V_{OC}^{sun}) due to reduced illuminance. The V_{OC} loss ΔV_{OC}^L can be expressed as [55]

$$\Delta V_{OC}^L = V_{OC}^{sun} - V_{OC}^{room} \sim \frac{n k_B T}{q} \ln \frac{P_{in}^{sun} \theta}{P_{in}^{room}} \quad (6)$$

where $P_{in}^{sun} = 100 \text{ mW cm}^{-2}$ and P_{in}^{room} are the incident power intensities of sunlight and room light, n is the ideality factor, T is the device temperature and k_B is the Boltzmann constant. $\theta \approx 56.65\%$ is the fraction of solar power of energy in the visible range and above. $P_{in}^{sun} \theta$ gives the effective incident power intensity on the PV device, excluding the IR radiation which does not contribute to photo-generation (and hence V_{OC}). In the range of 100–1000 lx, 0.22–0.16 V of V_{OC} loss based on the so-called one-sun V_{OC} would be observed. It is worth noting that, according to Equation (7), this V_{OC} loss is barely dependent on the choice of materials. Fig. 8 shows V_{OC}^{room} vs V_{OC}^{sun} under an illumination $L = 300 \text{ lx}$ for different organic PV cells. Indeed, a linear correlation can be found and in good agreement with Equation (7). [116]

There have been reports on the dependence of FF on the incident light intensity [115,117] in terms of the equivalent circuit model. Both of them suggested increasing FF at low illuminance, and a certain extent of decrease at high illuminance. At the low intensity regime, FF is dominantly affected by R_{sh} . Assuming a device with only bimolecular recombination, small R_{sh} , which may be caused by the pin holes in the photoactive blend, leads to a drop of FF at low light intensity. The smaller the R_{sh} , the more sensitive the FF drop. At high intensities, the larger photocurrent gives rise to more bimolecular recombination and a more dominant effect contributed by the series resistance (R_s), and hence the FF decreases. The light intensity corresponding to the turning point of the maximum FF increases with decreasing R_{sh} .

While V_{OC} , J_{SC} , FF and PCE are the key device parameters for reporting PV performance, the maximum power intensity generation (P_{max}), in the unit of $\mu\text{W cm}^{-2}$, under the illuminance of measurement is also recommended. Since the primary goal of IPV is to drive ultralow power nodes, in addition to the ambiguity of PCE evaluation due to the lack of common standard or calibration on the indoor light sources, P_{max} serves as a quick yet direct indicator in real applications such as how large the cell is needed for device operation. It should be noted, however, that the value of P_{max} is actually closely related to P_{in} even when comparing the same illuminance level. According to Equation (1), given an illuminance level, a large P_{in} is obtained if $S_{norm}(\lambda)$ does not match $V(\lambda)$ well. This is more evident in white phosphor LEDs with high color temperatures. With the intrinsic PCE, P_{max} likes to be larger under these light sources with the same illuminance. So the value of P_{max} of an IPV device at a particular illuminance is also subject to fluctuation.

In summary, we have discussed the diversity of IPV characterization. There are various types of indoor light sources, and nowadays the most popular sources emit cold light only. Each light source has its own characteristic emission spectrum which depends on the source type and color temperature. The illuminance level also varies from 200 to 1000 lx. A photometric (lux)-to-radiometric ($\mu\text{W cm}^{-2}$) conversion is needed for PCE evaluation. An illuminance spectrophotometer or an LED lux meter with NIST-traceable calibration is recommended for accurate and consistent illuminance measurement across the community. Conventional lux meters are not calibrated to cold light sources and produce measurement error. Class A or L instruments give small error

because of the small f_1' value ($< 3\%$). A number of portable illuminance spectrophotometers are commercially available, such as Konica Minolta CL-500A, InternationalLight ILT350 and Gossen Mavospec Base. Extech LT40-NIST is one representative LED light meter of NIST-traceable calibration. They should be regularly calibrated, say annually, to maintain the accuracy. A greater sampling delay time (> 1 s) is needed for reduced hysteresis during I - V measurements. Proper preconditioning should also be taken into consideration, especially in perovskite cells and DSSCs. When reporting device performance, the light source model, color temperature, emission spectrum and illuminance level should be specified. Besides V_{OC} , J_{SC} , FF and PCE, the incident power intensity and maximum power intensity generation should be given alongside each other. As revealed by the Shockley-Queisser limit, efficient IPV devices tend to possess large effective band gap (~ 1.9 eV) and thus V_{OC} , and the essentials are maximizing absorption and thus J_{SC} . Large V_{OC} materials evaluated under AM1.5 G should be potential candidates for IPV because they tend to have smaller fractional V_{OC} loss under reduced illumination.

3. Materials for indoor photovoltaics

Depending on the working mechanism of the photovoltaic technology, various photoactive materials including inorganic, organic, organometallic, organic-inorganic hybrid materials were adopted for making IPVs. In this review, we categorized current IPVs into four major photovoltaic technologies, namely, silicon or III-V semiconductor-based PVs, DSSCs, OSCs, and perovskite-based PVs. As mentioned previously, materials for IPVs should preferably possess absorption property in the region of 350–700 nm in addition to the suitable energy levels for constructing efficient devices. According to these four PV groups, photoactive materials depending on their nature, properties and device characteristics were thoroughly discussed in detail and compared within individual class and then compared in all classes.

3.1. Silicon and group III-V materials for indoor photovoltaics

Their design and working principle of inorganic semiconductors, such as silicon and III-V semiconductor-based solar cells are shown in Fig. 9. The device contains a planar junction of n-type and p-type of material sandwiched by a set of counter electrodes, which connected through external circuit. When sunlight falls on the device, some part of sunlight is absorbed by the p-n junction material and creates a pair of hole and electron. The electron moves through n-type material, hole moves through p-type material, and then complete circuit by generating the electric current. It is natural to extend this type of photovoltaic effect for harvesting the indoor light energy, in which the PCE of IPVs strongly depends on the purity and nature of silicon, which gives different absorption profile and degree of unwanted electron-hole recombination process. Therefore, for improving the efficiency of silicon-based IPVs, the judicious selection of the indoor light sources plays a major role. In addition to good surface passivation of device, we also need to find Si-based materials with the suitable optical energy gap to match the emission spectrum of the indoor lighting with low intensity.

Crystalline and amorphous silicon have been extensively studied and dominated for solar energy conversion due to their broad spectral response to sun irradiation. [118] Crystalline and amorphous silicon allotropes showed different photophysical properties as well as variable production costs. However, crystalline silicon is the commonly used and the best candidate for outdoor PV with a highest PCE achieved up to 26% under standard AM1.5 G solar condition [119–121]. Currently, silicon-based solar cells are also predominantly used in indoor applications. Basically, it can produce sufficient power if the function area is sufficiently large enough, serving as the power source for self-powered wireless devices. The improvement of parallel resistance is very important at low light intensity for optimizing the performance of IPVs

[122,123]. Crystalline silicon-based IPVs were studied under various low lighting intensity conditions and found that the PCEs mainly depend on the irradiance of light. The resulting IPV was successfully used to charge a lead battery for low energy storage [124,125]. In addition to the conventional hard module, flexible crystalline/amorphous silicon PVs were also demonstrated as efficient IPV with a high PCE of 9.1%. Due to their folding ability and good stability at ambient conditions in conjunction to the reduced installation cost, this technology paves a new way to make IPVs flexible, leading to new daily use applications [126,127]. As compared to crystalline silicon, amorphous silicon has advantages of high absorption coefficient and good capability of absorbing diffused light, rendering them more potential candidate for flexible panels IPVs. In this regard, Shieh and co-workers made a low-temperature growth of hydrogenated amorphous silicon carbide, that exhibits high molar absorptivity and low defect film density which can benefit to increase the V_{OC} of the device. The IPVs showed an impressive PCE up to 9.6% and P_{max} of $25.56 \mu\text{W cm}^{-2}$ under the illumination of a LED light at 500 lx. [128] Later, He and co-workers demonstrated omnidirectional organic/silicon hybrid device as a successful indoor light harvester with high V_{OC} under indoor light conditions. [129] In short, silicon-based IPVs shows so far the highest PCE of 9.6% under the illumination of a LED light. Although the existed massive uses of Si-based IPVs in various application, the high energy production and tedious purification of silicon-based materials together with the marginal PCE imply that Si-based IPVs is not sufficiently good as a reliable indoor light energy harvesting technology.

In addition to the well-developed Si-based PVs, the III-V semiconductors (GaAs) and other inorganic solid-state materials (CdS/CdTe and Cu(In/Ga)Se₂) are emerging as new inorganic PV materials due to their strong absorption and low carrier recombination rates which are essential parameters to make better IPVs. The GaAs-based PVs was reported to deliver a state of the art PCE up to 28% under standard illumination conditions. [14,130] From the property-modulation point of view, GaAs has the fundamental advantage of tuning the band gap, which allows the absorption matching to the emission of indoor light sources, thus renders the resulting IPV to produce enough power for perpetual operation of mm-scale devices [131,132]. For example, Al-GaAs exhibits a larger optical band gap, which is beneficial for indoor light harvesting, together with the low dark current, a high PCE of 21.1% was achieved under a LED light with irradiance of 580 lx [133]. In addition to GaAs, indium gallium phosphide (InGaP) material possesses the highest surface power density, which was employed to construct an IPV by choosing the indoor light source integrated with ZnS:Cu,Al as phosphor because of its band gap well matched to the

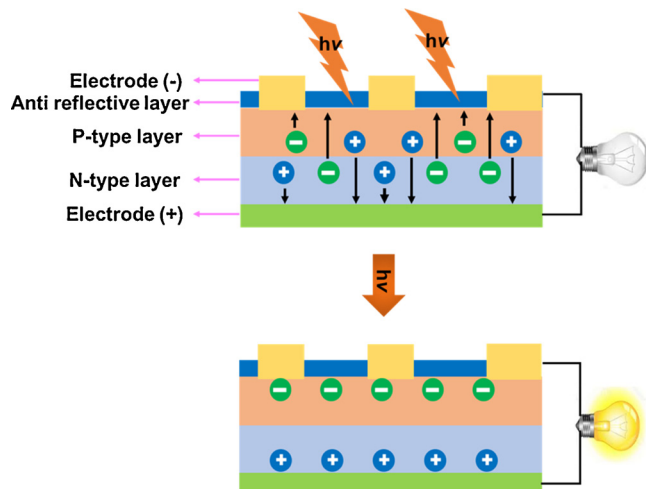


Fig. 9. Typical schematic device configuration and working principle of Si and III-V semiconductor-based solar cells.

InGaP material. The resulting IPV device produced a high PCE of 29% under $1 \mu\text{W}_{\text{opt}}\text{cm}^{-2}$ from a LED illumination with the central peak at 523 nm. [134] It is clear that crystalline GaAs- and InGaP-based IPVs outperform the silicon-based counterparts. In addition to III-V semiconductors, CdTe/CdS exhibits the advantages such as good abundance, cheap for material production and easy for device manufacturing, render them a rapid growth in solar cell market, leading to the second largest most utilized solar cell. However, the comparatively lower absorption capability makes the CdTe/CdS-based PV to reach a PCE of 22% under standard AM1.5 G solar conditions [120]. Interestingly, their absorption spectrum can better match to the emission spectrum of indoor light, giving the device to show a PCE of 8% under low irradiance [135]. For improving the absorption feature, Cu(In/Ga)Se₂ was developed. Indeed, the strong absorption character promoted the PCEs up to 23% under direct solar radiation, [136] however, the corresponding device only showed a poor PCE (2.64%) under a LED illumination [13]. When compared to silicon-based solar cells, Cu(In/Ga)Se₂ showed inferior PCEs and this can be tuned/boosted by suitable indoor lighting conditions, particularly incandescent lamps which can improve the performance. [137] Several groups studied and compared the various types of III-V group materials under various indoor light conditions and found that each material displays a better PCE in some selected indoor light sources, for example, indoor fluorescent lighting gave high relative efficiency when compared to LED and incandescent lighting [138].

Overall, the IPVs based on III-V semiconductors such as GaAs and InGaP showed high PCE (~ 28%) under the illumination of LED light. The high stability of inorganic photoactive materials is advantageous for long-lived IPV applications. To further improve the PCE of III-V group IPVs, fundamental understanding of the loss mechanisms such as transparency, recombination and resistance losses are necessary. Nevertheless, III-V semiconductors harvest photons extending to the NIR region, other suitable absorbing materials compatible to commonly used indoor lights are strongly encouraged for IPVs to achieve better PCEs. It can be envisioned that new inorganic materials with suitable optical energy gap nicely responding to indoor lightings are sufficiently potential candidates for IPVs. However, it is generally believed that the high cost for producing these inorganic materials will be the main obstacle for the cost-competitive production for practical commercialization.

3.2. Organic dye sensitizers for indoor photovoltaics

The typical DSSC device configuration and operational principle involved to generate electricity are shown in Fig. 10. The device contains mainly five components, namely, (1) a conductive fluorine-doped tin oxide (FTO) glass, (2) a nanocrystalline TiO₂ or ZnO semiconductor

thin film, (3) a dye sensitizer, (4) an electrolyte (I_3^-/Γ couple, Co(II)/Co(III) couple or Fc/Fc^+ couple) for liquid state DSSC or hole transport material for solid state DSSC, and (5) a counter electrode such as platinum or carbon-coated FTO glass. In a DSSC device, the working/operational process starts from the absorption of light by dye sensitizer followed by the electron injection from the excited state of dye to the conduction band of TiO_2 for creating the charge separation at dye/ TiO_2 interface. Then, charge collection at the anode substrate and regeneration of oxidized dye by gaining an electron from redox electrolyte or hole transport material. Finally, the oxidized electrolyte or hole transport material was regenerated at counter electrode by taking electrons from external circuit. For efficient DSSC, the molecular engineering on dye molecules are crucial for giving matched absorption spectra corresponding to the solar emission spectrum. Along with the strong absorption of dye sensitizer, it should contain (1) favorable molecular geometry to retard aggregation/electron recombination, (2) favorable HOMO/LUMO energy levels; LUMO of the dye must be higher than the conduction band of TiO_2 , and HOMO of dye should be lower than redox potential of electrolyte or hole transport material for better dye regeneration, (3) long term stability of dye as well as the cell. [139–148] To boost the PCE of DSSC, several strategies were developed such as the extension of π -conjugation by different spacers for strong absorption, [149–151] the incorporation of twisted/bulky groups to reduce aggregation [152–154], the attachment of long alkyl groups to minimize back electron transfer [155–157], and the development of di-anchoring dyes [158–160] for compact packing and stronger adsorption on TiO_2 , etc.

Since 1990, DSSC have been extensively studied because organic dyes possess more flexibility for molecular designs and high molar absorptivity in addition to the easy device fabrication, lower production cost and semi-transparent feature. [139–148] So far, the state of the art PCE of a single cell DSSC device has reached up to 14% under standard solar illumination [25]. Even though they showed high PCEs, researchers are struggling for highly efficient DSSC panel commercialization due to the lack of promising and stable dyes for NIR absorption as well as the long term stability of the device [161]. Interestingly, most of the active dyes show intense absorption profiles in UV-vis region enabling them better opportunity to match with indoor light conditions and produce better PCE when compared to silicon and group III-V materials. In this line, DSSCs turned to be very excited candidates for using in IPV applications [162]. Particularly, the weak intensity of indoor lights unlocks the photo-bleaching issues, which are usually significant challenges in organic dyes under sunlight, and thus opens a great avenue for molecular designs of new dyes for IPVs. Up to date, some reports made on feasible strategies to modulate the absorption profiles of organic materials using for DSSCs. In DSSCs, ruthenium-based metal complexes are pioneer dyes which have been extensively

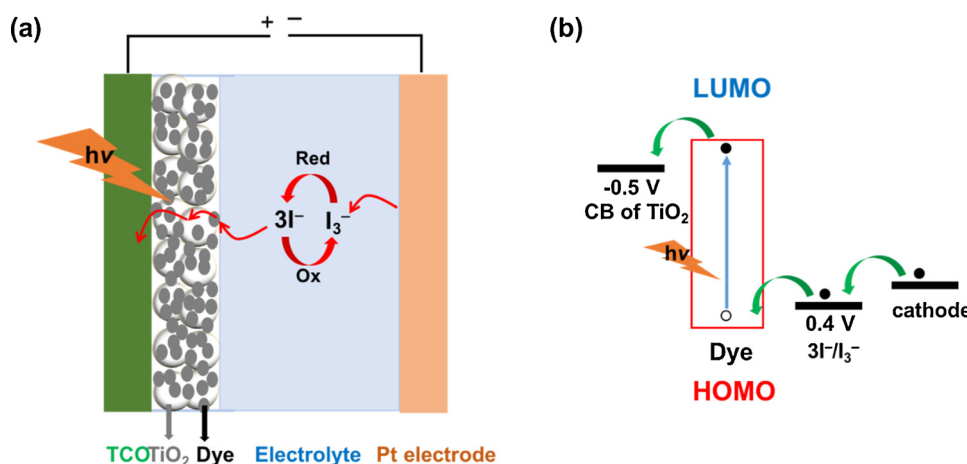


Fig. 10. Typical schematic (a) device configuration and (b) working principle of DSSCs.

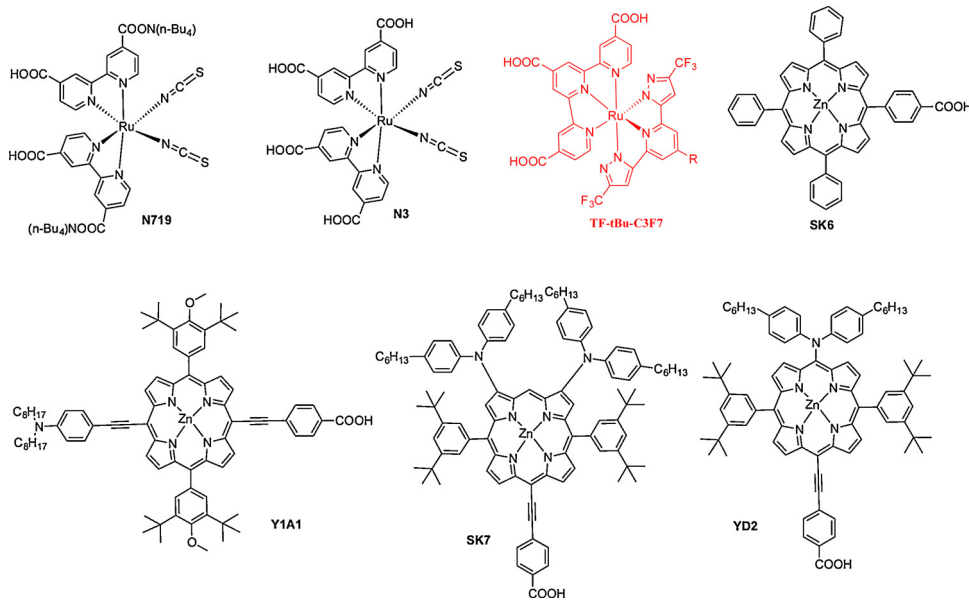
studied due to their broad metal-to-ligand charge transfer absorption bands and suitable HOMO and LUMO levels with respect to the conduction band of TiO_2 and redox electrolyte, respectively. [145] In 2000, Grätzel and co-workers, for the first time, constructed an indoor DSSC device by using the benchmark dye N719 (**Scheme 1**) under a Philips TLD 840 fluorescent tube of 250 lx, producing a P_{\max} of $69.8 \mu\text{W cm}^{-2}$, which is comparable with commercially available silicon-based PV panels of a P_{\max} of $70.1 \mu\text{W cm}^{-2}$. [164] Later, several groups studied N719-based DSSCs under low light intensity conditions and found that these devices are stable enough for industrial applications. [26,163–165] In addition, Segawa and co-workers found that decreasing the light intensity increases the PCE of N719-based DSSC, which is due to the internal capacitive current and hysteresis behavior of the *I-V* curve. [166] Along this line, Chen and co-workers made a roof-DSSC hybrid panels incorporated N719 dye to produce a high PCE of 8.20% with a main contribution from J_{SC} ($6 \mu\text{A cm}^{-2}$) (**Table 2**) under a dim light with the light intensity of 1000 lx. [167]

Further material developments have been implemented into DSSC technology. For example, He and co-workers introduced graphene dot incorporated PEDOT:PSS as counter electrode to improve the efficiency of a N719-based DSSC up to 7.36% under low light intensity conditions based on a dim light. The improved efficiency was ascribed to the high electron conductivity and the low charge transfer resistance. [168] Kapil and co-workers invented titanium (Ti)-coil based cylindrical N719-based DSSC cell, the PCE was significantly improved to 14.95% which is comparable to that of silicon-based solar cells. [169] Also, screen-printed DSSC employing N719 dye incorporated with $\text{TiO}_2\text{-ZnO}$ nanocomposites was successfully demonstrated for indoor application with a PCE of 5.22% under a white LED at 3333 lx. These DSSC devices exhibited better photovoltaic properties as compared to those of silicon-based solar cells. [170] Recently, Lee and co-workers made quasi-solid-state (QS) DSSC based on N719 dye by using polymer gel electrolyte. Its best QS-DSSC device showed high recombination resistance and high incident photon to current efficiency which increased V_{OC} (0.59 V) and J_{SC} ($92 \mu\text{A cm}^{-2}$) and then PCE of 20.63% and P_{\max} of $39.6 \mu\text{W cm}^{-2}$. [171] The success of N719 dye in DSSC application has stimulated the emergence of new Ru-based dyes, for example, Teng and co-workers studied N3 dye for indoor DSSC by using zinc-doped TiO_2 anode, which shows a high electron collection efficiency from the excited state of dyes. This indoor DSSC delivered a PCE of 0.04% under visible light. Later, Chi and co-workers designed and synthesized bis-trident ruthenium sensitizer named as TF-tBu-C3F7 (**Scheme 1**) with perfluoroalkyl

fragments on the ligand in order to balance the dye loading and charge recombination processes. The photovoltaic characteristics of TF-tBu-C3F7-based device were measured under indoor light sources such as LED (2400 lx) and T5 fluorescent lamp (2400 lx), achieved a high PCE of 16.05% and 20.37%, respectively. The better device performance under a T5 fluorescent lamp source has been attributed to its better absorption matching with the TF-tBu-C3F7 dye. [172] Apparently, new ruthenium-based dyes with strong absorption in UV-vis region together with high molecular extinction coefficients are required to deliver higher PCEs in future IPVs application.

However, the rarity of ruthenium due to the limited natural sources may shadow the future of large-scale applications of Ru-dyes-based DSSCs. Thus, new Ru-free metal-containing dyes are emerging as alternatives. In this context, porphyrin is potential candidate because of their superior light-harvesting ability in the visible region. [173] Additionally, the easy molecular structure engineering enables the tuning of optical and electrochemical properties very feasible. In this regard, Yeh and coworkers designed a simple push-pull porphyrin-based dye SK6 and an amine-substituted porphyrin dye Y1A1 for examining their IPVs applications under various indoor light sources. [70,174] The simplified porphyrin dye (SK6) under a T5 fluorescent lamp with 6000 lx illumination produced a PCE of 19.71%. However, Y1A1 exhibited a PCE of 19.50% under a LED light source because of the better matching absorption when compared to other light sources such as T5 and T8 fluorescent lamps. Later, the same group modified porphyrin by introducing one diarylamo group at the meso position for a new porphyrin derivative (YD2), in addition, incorporated two diarylamo groups at β position for another new porphyrin (SK7) for broadening the absorption profiles as well as red shifted absorption spectra. [175] These new dyes YD2 and SK7 were employed as sensitizers for constructing indoor DSSC devices and studied the device characteristics under a T5 light illumination (6000 lx), giving the impressive PCE of 20.0% (P_{\max} of $340 \mu\text{W cm}^{-2}$) and 19.7% (P_{\max} of $335 \mu\text{W cm}^{-2}$), respectively. The obtained high PCEs are arose from the introduced diarylamo substitution(s) which splits Soret band (400–500 nm region) and red shifted Q-band in the visible region, consequentially leading to better matching absorption toward the indoor light sources tested.

Another approach to overcome the possible drawbacks of Ru-based dyes focuses on metal-free organic dyes, that have attracted immense intentions owing to the flexible molecular designs, which allow strong UV-vis absorption, suitable HOMO/LUMO energy levels, and favorable



Scheme 1. Chemical structures of inorganic sensitizers for indoor DSSCs.

Table 2

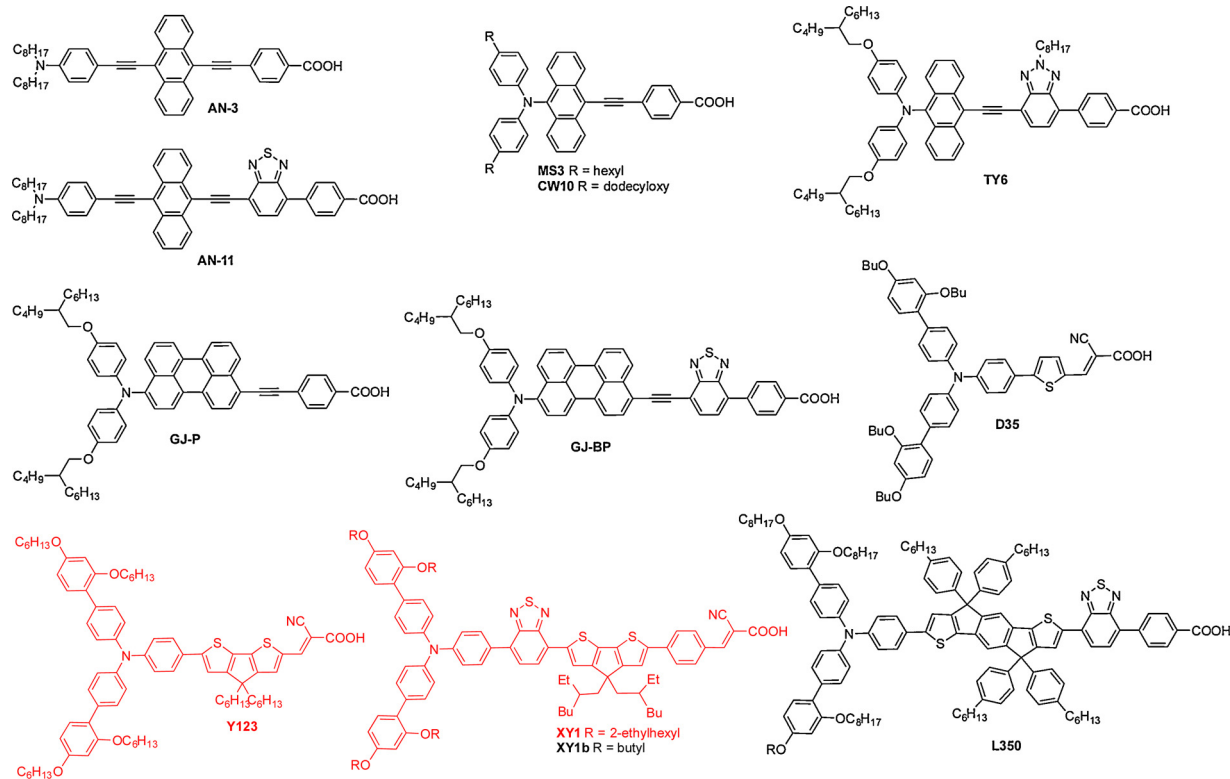
Optical, electronic and photovoltaic properties of organic dye sensitizer based IPVs.

Dyes	λ_{abs} (nm)	HOMO/LUMO vs NHE (eV)	Indoor Light Source	Light Intensity (lux)	J_{SC} ($\mu\text{A cm}^{-2}$)	V_{OC} (V)	FF	PCE (%)	P_{max} ($\mu\text{W cm}^{-2}$)	Ref.
N719	527	1.07/1.14	CFL	500	22	0.58	0.82	6.58	10.3	[162]
			LED	500	22	0.58	0.81	6.27	10.4	[162]
			Visible lamp	230	94	0.48	0.53	0.04	–	[170]
			White light	1533	89	0.57	0.68	14.95	34.4	[169]
			Dim-light simulator	1000	66	0.53	0.75	8.22	–	[167]
			T5 fluorescent light	600	92	0.59	0.72	20.63	39.6	[171]
TF-tBu-C3F7	675	0.93/0.93	LED	2400	270	0.59	0.73	16.05	–	[172]
Y1A1	678	0.85/0.99	T5-White fluorescent	2400	320	0.60	0.74	20.37	–	[172]
			T8-White fluorescent	300	46	0.47	0.77	17.00	16.5	[70]
			T5-White fluorescent	300	53	0.47	0.74	19.30	18.2	[70]
SK6	595	1.03/1.03	LED	350	57	0.48	0.76	19.50	20.3	[70]
			T5-White fluorescent	6000	827	0.58	0.76	19.71	366.0	[174]
			T5-White fluorescent	6000	739	0.58	0.78	19.70	335.0	[175]
YD2	645	0.89/1.09	T5-White fluorescent	6000	721	0.60	0.78	20.00	340.0	[175]
D35	445	1.04/1.37	Osram Dulux white fluorescent lamp	250	18	0.70	0.80	–	10.7	[176]
AN-3	499	0.64/1.19	T5-White fluorescent	1000	60	0.46	0.67	5.45	660.0	[177]
			T8-White fluorescent	1000	60	0.43	0.63	4.85	590.0	[177]
			LED	1000	50	0.45	0.66	4.94	560.0	[177]
CW10	507	0.74/1.48	T5-White fluorescent	6000	770	0.67	0.76	21.26	395.0	[174]
SK6+CW10			T5-White fluorescent	6000	883	0.65	0.75	22.91	426.0	[174]
N719			T5-White fluorescent	6000	912	0.65	0.73	23.43	435.0	[174]
TY6	516	0.95/1.21	T5-White fluorescent	6000	883	0.72	0.79	28.56	–	[72]
AN-11	528	1.09/1.35	T5-White fluorescent	1000	62	1.05	0.64	11.94	42.0	[178]
			LED	1000	53	1.04	0.65	11.26	36.0	[178]
GJ-P	520	0.80/1.34	T5-white fluorescent	6000	594	0.60	0.74	15.01	262.0	[179]
GJ-BP	541	0.78/1.25	LED planar light	6000	540	0.59	0.74	13.05	236.0	[179]
			T5-white fluorescent	6000	640	0.57	0.76	15.79	276.0	[179]
L350	519	1.04/0.94	LED planar light	6000	557	0.56	0.76	13.10	237.0	[179]
			White fluorescent Tube Light	1000	132	0.83	0.78	28.40	–	[181]
			Osram Warm White 930	1000	138	0.80	0.80	28.90	88.5	[180]
XY1	463:552	1.04/1.35:0.99/0.98	White Fluorescent Tube Light	1000	418	0.88	0.77	31.80	283.0	[27]
XY1b:Y123	552:530	0.99/0.98:1.08/1.09	LED	600	380	0.50	0.67	6.42	–	[182]
TKU-1	441	0.93/1.39	T5-White fluorescent	600	440	0.49	0.67	7.80	–	[182]
TKU-2	463	0.83/1.42	LED	600	560	0.57	0.73	11.71	–	[182]
TKU-3	441	0.88/1.49	T5-White fluorescent	600	600	0.55	0.71	12.73	–	[182]
TKU-4	470	0.85/1.37	LED	600	360	0.53	0.69	6.56	–	[182]
TKU-5	432	0.82/1.56	T5-White fluorescent	600	470	0.55	0.71	9.99	–	[182]
TKU-6	480	0.82/1.56	LED	600	560	0.60	0.70	11.49	–	[182]
TKU-6	480	0.78/1.36	T5-White fluorescent	600	500	0.59	0.73	10.76	–	[182]
LI-127	406	0.72/1.81	LED	600	600	0.60	0.71	12.73	–	[182]
LI-128	506	0.71/1.30	White LED light	0.56	0.106	0.57	0.72	8.16	–	[183]
LI-129	412	0.72/1.78	White LED light	0.56 ^a	0.154	0.54	0.60	8.66	–	[183]
LI-130	501	0.71/1.30	White LED light	1.39 ^a	0.198	0.62	0.79	7.03	–	[183]
MK-2	480	0.96/0.87	White LED light	1.39 ^a	0.5	0.63	0.57	11.63	–	[183]
			T5 fluorescent light ^a	1001	83	0.64	0.51	8.56	–	[184]
			T5 fluorescent light ^b	85	0.70	0.82	15.26	–	–	[184]
MD4	633	0.96/0.80	T5 fluorescent light	200	25	0.67	0.79	20.11	–	[185]
			T5 fluorescent light	6000	315	0.58	0.72	8.62	–	[187]
			T5 fluorescent light	6000	762	0.65	0.79	23.17	–	[187]
MD6	642	0.84/0.90	T5 fluorescent light	6000	562	0.63	0.77	16.86	–	[187]
MD7	532	0.88/1.13	T5 fluorescent light	6000	913	0.68	0.76	27.17	–	[187]
MM-1	435	0.74/1.57	TL84 fluorescent lamp	2500	120	0.46	0.64	7.72	–	[188]
MM-2	457	0.74/1.47	TL84 fluorescent lamp	2500	133	0.48	0.62	9.03	–	[188]
MM-3	427	0.71/1.83	TL84 fluorescent lamp	2500	131	0.49	0.70	9.86	–	[188]
MM-4	445	0.73/1.70	TL84 fluorescent lamp	2500	170	0.50	0.66	12.14	–	[188]
MM-5	470	0.54/1.56	TL84 fluorescent lamp	2500	248	0.57	0.65	19.89	–	[188]
MM-6	484	0.52/1.55	TL84 fluorescent lamp	2500	309	0.60	0.70	27.82	–	[188]
MM-6 + DCA			TL84 fluorescent lamp	2500	303	0.625	0.70	28.95	–	[188]
MM-6 + MM-3			TL84 fluorescent lamp	2500	312	0.62	0.73	30.45	–	[188]

^amW cm⁻²; ^bTiCl₄.

molecular interactions for compact packing on TiO₂ layer. In 2010, Hagfeldt and co-workers reported an organic dye **D35** (Scheme 2) configured with a typical donor-π-bridge-acceptor architecture, in which a tailor-made triarylamino group was introduced as donor for reducing dye aggregation as well as the recombination of electrons. The DSSC device employed **D35** as sensitizer in combination with [Co

(bpy)₃]^{3+/2+}-based electrolyte achieved a P_{max} of 10.7 μW cm⁻² under fluorescent light illumination of 250 lx. [176] Later, Lin and co-workers designed an anthracene-containing dye **AN3** and its indoor DSSC showed a moderate PCE of 5.45% and P_{max} of 660 μW cm⁻² under a T5 fluorescent lamp (1000 lx). The inferior efficiency was ascribed to poor absorption and low dye loading on TiO₂ film. [177] This result clearly



Scheme 2. Chemical structures of organic sensitizers for indoor DSSCs.

indicates that not only the red-shifted absorption of a target dye is important, the suitable HOMO and LUMO energy levels are also crucial for smoothly charge injection to the conduction band of photo-anode and dye regeneration by the redox electrolyte.

Furthermore, Yeh and co-workers carefully designed a new anthracene-containing dye **CW10** which contains alkoxy substituted diarylamine donor. [174] **CW10** exhibits strong absorption (507 nm) as well as high HOMO and low LUMO levels, as a result, these favorable properties lead the **CW10**-based indoor DSSC device to achieve a high PCE of 21.26% and P_{\max} of $395 \mu\text{W cm}^{-2}$ under the illumination of a T5 fluorescent light (6000 lx). In addition to this great achievement, the same group has made co-sensitized DSSC by adding dye **SK6**, which shows complimentary absorption to cover the UV-vis region, the resulting device further improved the PCE to 22.91% and P_{\max} of $426 \mu\text{W cm}^{-2}$ under the same irradiance conditions. Along this line, Yeh and co-workers made an anthracene-based dye **TY6** different from the **CW10** shown in Scheme 2 to further enhance the absorption feature by the incorporation of electron deficient benzothiadiazole unit into the molecular skeleton. [72] **TY6** showed as a further red-shifted absorption (516 nm) and higher HOMO level as compared to those of **AN-3** and **CW-10** dyes (Table 2). These new features allow the **TY-6**-based DSSC device to perform an outstanding PCE up to 28.56%, high J_{SC} ($883 \mu\text{A cm}^{-2}$) as well as high V_{oc} (0.72 V) under the T5 light irradiance of 6000 lx (Table 2). The similar approach of introducing component with quinoidal character was also reported by Lin and co-workers. A new anthracene-based dye **AN-11** incorporating benzothiadiazole together with modified dialkylamino donor was synthesized. [178] **AN-11** showed a further red-shifted absorption to 528 nm. It is worthy to note that the device is highly stable, for example, an **AN-11**-based flexible DSSC module was subjected to a stability test at 65 °C and 65% humidity conditions, the DSSC module retained its maximal output power up to 600 h. In addition, the device efficiency retains even in large size, for example, an **AN-11**-based rigid indoor DSSC with a large active area of 26.8 cm^2 reached an overall PCE of 11.94% under 1000 lx of a T5 fluorescent light.

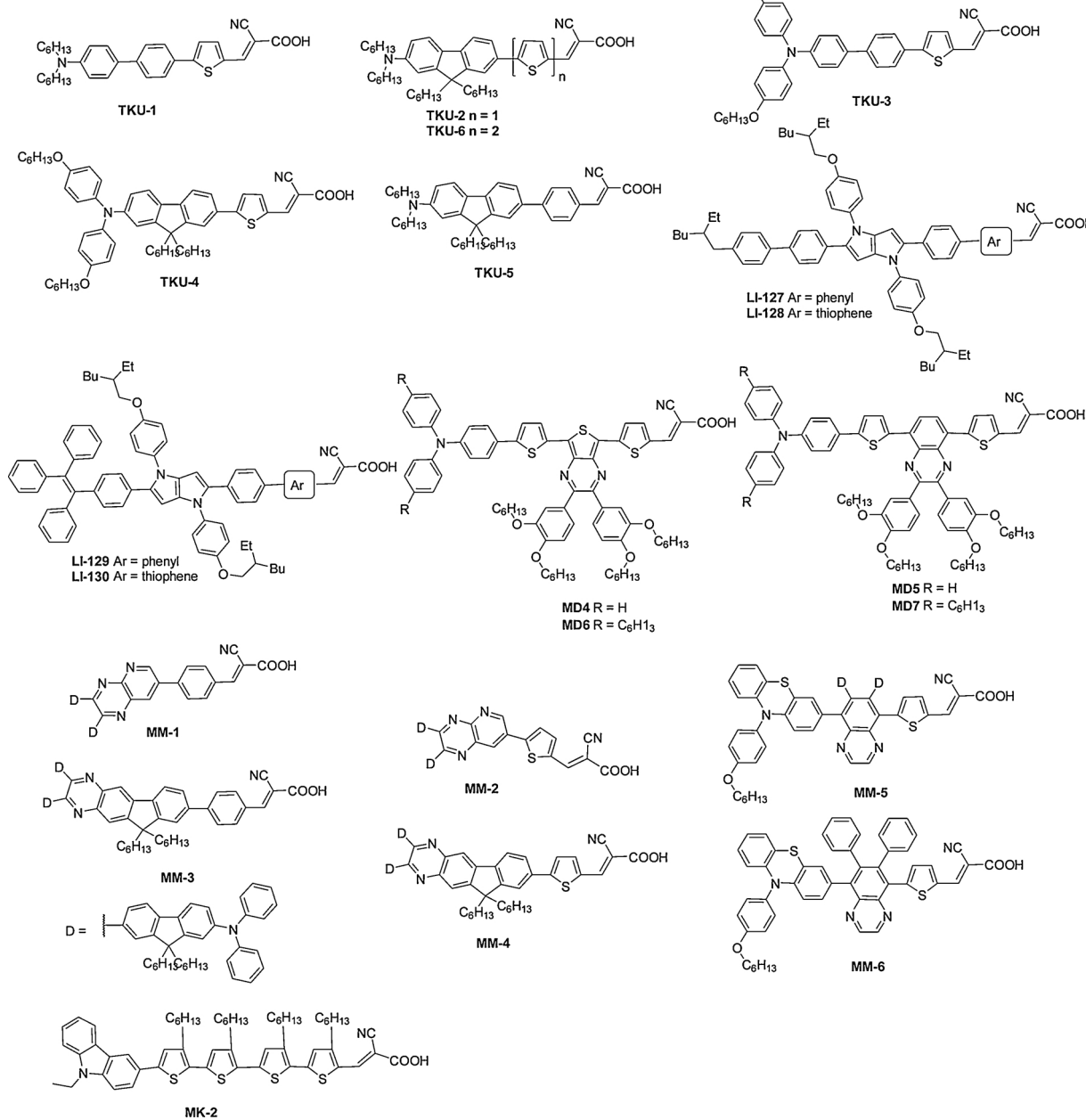
In line with the approach of incorporating polyaromatic arene as the constituent of DSSC dye, Yeh and co-workers introduced diarylaminostyrene into the conjugated system to make new dyes (**GJ-BP** and **GJ-P**) in combination with and without benzothiadiazole unit, respectively. [179] **GJ-BP** shows red-shifted absorption (541 nm) as compared to that of **GJ-P** (520 nm). Under a T5 fluorescent lamp (6000 lx), the DSSC device employing **GJ-BP** dye results a PCE of 15.79%, and P_{\max} of $0.28 \mu\text{W cm}^{-2}$ and J_{SC} of $640 \mu\text{A cm}^{-2}$ that are better than **GJ-P**-based device (PCE of 15.01%, P_{\max} of $0.26 \mu\text{W cm}^{-2}$ and J_{SC} of $594 \mu\text{A cm}^{-2}$) (Table 2). The dye **GJ-BP** incorporated with benzothiadiazole π-linker adjacent to benzoic acid acceptor/anchor shows better PCE due to its superior light-harvesting property, suitable HOMO level, and well-ordered dye arrangement on TiO_2 surface. The introduction of quinoidal type structure largely benefits to modulate the absorption profile of the resultant dye, for example, a panchromatic **XY1** dye containing benzothiadiazole and C-bridge bithiophene, was designed and synthesized by Hagfeldt and co-workers. [180] The DSSC device based on **XY1** dye together with **D35** as co-sensitizer for better spectral coverage delivered a high PCE of 28.90% and P_{\max} of $88.5 \mu\text{W cm}^{-2}$ under 1000 lx of white lamp. It is noteworthy to mention that the high PCE mainly originates from high external quantum efficiency of DSSC cell in the visible region. Later, Liu and co-workers reported a new dye **L350** incorporating indacenodithiophene and benzothiadiazole as the conjugated components which facilitate the tuning of optical and electronic properties for the better alignment with the redox of copper(I/II)-based electrolyte. [181] The indoor DSSC device with **L350** dye showed an impressive PCE of 28.4% under the illumination at 1000 lx of an Osram 930 warm-white fluorescent light tube. The great success of **XY1** dye in giving high efficiency renders the further investigation highly desirable. In this regard, Grätzel and co-workers used a judicious combination of **XY1** dye and co-sensitized **Y123** dye (Scheme 2) for effective and better spectral coverage. [27] They invented a new generation DSSC, in which the dye-impregnated mesoscopic TiO_2 films were attached with porous paper to avoid direct contact between the PEDOT counter electrode and the redox

electrolyte. As a result, **XY1b:Y123** co-sensitized DSSC device showed a record-high PCE of 31.80% and P_{max} of 283 $\mu\text{W cm}^{-2}$ under 1000 lx of a white fluorescent tube light. The results are very exciting and the obtained device performance exceeds the silicon- and GaAs-based solar cells.

Along with C-bridged bithiophene, fluorene was also introduced to make new dyes for indoor DSSC application. For example, Wang and co-workers designed and synthesized a set of dyes **TKU1-TKU6** (**Scheme 3**) based on fluorene building block (**TKU2**, **4-6**) as compared to those without fluorene (**TKU1**, **TKU3**). [182] When compared to phenyl linker-based dyes (**TKU1** and **TKU2**), fluorene-based dyes (**TKU2**, **TKU4-6**) exhibited suitable absorption range (250–600 nm) for indoor DSSCs due to the incorporation of fluorene which can extend conjugation and make better donor to acceptor/anchor interactions. Dye (**TKU4**) containing alkoxy substituted diphenylamino donor showed intense absorption peaks in the short wavelength region (250–400 nm) might benefit for better light-harvesting than

dialkylamino unit containing dyes (**TKU2**, **TKU5-6**), which exhibit poor absorption in the similar absorption region mentioned above. Among them, **TKU-4** exhibits well matched absorption, and possesses alkoxy chains on the donor part, which is advantageous to give a larger V_{OC} of the DSSC device. These new dyes were examined as sensitizers for indoor DSSC devices under LED and T5 fluorescent lamps. The results showed better PCEs for the T5 light due to the better overlapping of **TKU** dyes (250–600 nm) with the emission of T5 light (400–650 nm) when compared to LED light (400–700 nm). Among these dyes, **TKU4** dye showed the highest PCE of 13.43% under a T5 light due to the red-shifted absorption when compared to those of other dyes.

Later, Li and co-workers reported a novel strong donor π -conjugated unit, tetraaryl-1,4-dihydroptyrrolo-[3,2-*b*]pyrroles and made a set of push-pull dyes (**LI127-LI130**) suitable for DSSC by incorporating alkoxy phenyl, triphenylethylene units as donors. [183] Among them, the dyes (**LI128** and **LI130**) containing thiophene linker to acceptor/anchor showed red-shifted absorption than phenyl linker containing dyes



Scheme 3. Chemical structures of organic sensitizers for indoor DSSCs.

(LI127 and LI129) due to the presence of phenyl linker leads to twisted conformation and then diminishes donor-acceptor interactions. Dyes containing triphenylethylene unit was well established for the suppression of aggregation and thus reduce the electron recombination at the TiO_2 /dye/electrolyte interface. Finally, LI-130 based indoor DSSC device exhibited the highest PCE of 11.6% under a LED light (1.39 mW cm^{-2}) due to the suppression of electron recombination and broad absorption spectrum when compared to other dyes. The result clearly indicates that the suppression of electron recombination is a crucial factor for greatly improving the PCE of the DSSC device. In this line, Lee and co-workers brilliantly incorporated the TiCl_4 blocking layers between the FTO/electrolyte interface to minimized the electron recombination. [184] They examined the DSSC device composed of MK2 dye and $\text{Co}(\text{bpy})_3^{2+/3+}$ redox electrolyte, and demonstrated that the compact blocking layer of TiCl_4 can effectively suppress the electron leakage over a wide range of light intensity under a T5 fluorescent light (1000 lx). The indoor DSSC device based on MK2 dye showed a better PCE of 15.3% under a T5 fluorescent lamp. This strategy paves a way to make an efficient device configuration and then better efficiency devices. Recently, the same group led by Lee utilized nanocomposite gel electrolytes to make QS-DSSC employing MK2 as dye, the new indoor DSSC device delivered an improved PCE up to 20.11% and P_{\max} of $13.12 \mu\text{W cm}^{-2}$ under room light conditions (200 lx). [185]

Unlike the outdoor DSSC device there is no need of matching solar spectrum in the case of indoor DSSC device, but it should response to the emission spectra of indoor light sources. [186] In this line, Lina and co-workers designed a set of D-A¹-π-A-configured dyes MD4-MD7 (Scheme 3) by incorporating thieno/benzo pyrazine as the A¹ group. [187] The thienopyrazine containing dyes (MD4, MD6) showed red-shifted absorption maxima as compared to those of benzopyrazine-based counterparts due to the strong intramolecular charge transfer feature. However, the benzopyrazine containing dyes MD5 and MD7 achieved higher PCE of 23.17% and 27.17%, respectively, as compared to that of thienopyrazine-based dyes MD4 (8.62%) and MD6 (16.86%) due to the effective electron injection to the conduction band of TiO_2 and the suppression of dark current. Very recently, Chang and co-workers designed new organic dyes (MM-1 to MM-6) with quinoxaline or quinoxalinoid as electron-accepting unit. Among them, MM-6 showed the highest PCE of 27.82% due to its better spectral coverage with indoor lighting. Since the co-sensitization can afford better performance, a co-sensitized dye system based on MM-6 and MM-3, delivered a better PCE of 30.5% under TL84 fluorescent lamp (2500 lx). The superior performance of device with co-sensitizers can be ascribed to the better dye-coverage on TiO_2 surface. [188]

In summary, the progresses on new organic dyes suitable for indoor DSSC devices are rather promising. So far, the indoor DSSC device based on a dye XY1 with benzothiadiazole and C-bridge bithiophene for panchromatic absorption achieves the best PCE of 28.90% under a Osram warm white fluorescent lamp at 1000 lx. The analogue XY1b was further investigated together with a co-sensitizer (Y123) for better

spectral coverage, achieving a record-high PCE up to 32% under a white fluorescent light (1000 lx). The required molecular π -conjugation for giving absorption in the range of 350–700 nm will largely limit the choice of aromatic units for constructing the desired DSSC dyes. New molecular design approaches that can result in high extinction coefficients in visible wavelength are crucial in this field. In addition, particular attentions should pay for the molecular features that can (1) lead to compact packing on TiO_2 with reduced flexibility of anchoring modes, (2) reduce electron recombination and dark current, (3) lower down the HOMO level and create more space for electrolyte development to eventually increase the V_{OC} . Overall, the development of new dyes with innovative molecular designs to obtain well-matched wide absorption of indoor light sources, and/or utilize co-sensitization methods will lead DSSC device to perform further better PCEs in the near future.

3.3. Organic donor/acceptor materials for indoor photovoltaics

The use of organic materials for PVs can also be realized by OSCs technology. The device configuration and working/operational principle of OSC are depicted in Fig. 11. The OSC device mainly consists of an active layer, which is sandwiched by two counter electrodes (anode and cathode). The working principle mainly involve four steps: (1) the absorption of solar light by either/both donor or acceptor in the active layer generates excitons, (2) excitons diffuse to reach to the donor/acceptor interface, (3) dissociation of excitons into hole and electron, (4) hole transports through donor domain to the anode and electron transports through acceptor domain to the cathode, connecting to the external circuit for producing a photocurrent. Importantly, the PCE of OSCs mainly depends on the donor and acceptor components of the active layer by following steps: (1) the broad and intense absorption either from donor or acceptor favors the better light harvesting of solar light, (2) suitable energy levels such as LUMO of donor slightly higher than LUMO acceptor ($\sim 0.3 \text{ eV}$) for effective charge transfer, (3) nanophase separation with face-on oriented crystalline blend films, (4) better charge carrier transportation in nanophase active layer. [189–200]

As compare to DSSC, OSCs are free from tedious and complicated issues of the interfaces between the organic active materials and the anode as well as the electrolyte. For the last two decades, the research concentrated on OSCs is the hot topic in the development of new PVs beyond Si-based ones. [189–200] In the OSC device, usually a blend active layer made from an electron donor (D) and an electron acceptor (A) enables broad spectral coverage for sunlight as well as indoor light. We need to carefully choose the suitable HOMO/LUMO matchup between D and A in order to achieve efficient photo-induced D-to-A or vice versa electron transfer as well as retain the device with a high V_{OC} . [189–200] After intensive research works implemented on the molecular structures and D/A morphology control as well as device engineering, the state-of-the-art PCE of OSCs is up to 16.5% [36,38,39].

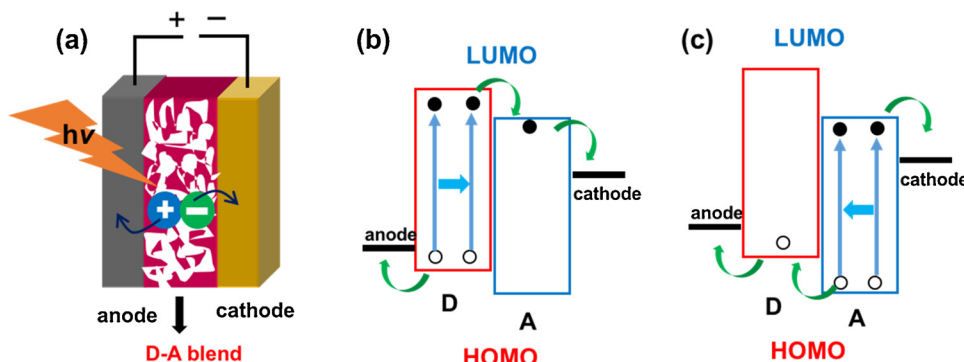


Fig. 11. (a) Typical schematic device configuration and working principle of OSCs (excitation takes place in (b) donor and acceptor (c)).

Simply from the D/A structure point of view, balancing the wide spectral response and good charge transportation with the favorable molecular interactions and crystallinity of active layer are the bottleneck challenge for the further PCE improvement. Among various molecular design strategies, the incorporation of fused and coplanar oligoarene systems either in donor or acceptor is the most successful approach for generating semi-crystalline blend films with good morphology. Fullerene derivatives are superior acceptors with good electron-transporting character while they exhibit poor spectral response toward sunlight. But for indoor OSCs, the selection of donor and acceptor is more flexible to fulfill the good spectral response and charge carrier transportation. In this line, several reports were made on developing new organic donor/acceptor materials for IPVs and the first seminal report came one decade ago [40]. However, these early studies of indoor OSCs only produced moderate PCEs. Nowadays, the progress of indoor OSCs has substantial improvement, where high PCE up to 28% under light source (1000 lx) was reported recently [42]. The growing momentum in this field may facilitate the commercialization of OSCs for indoor light energy harvesting in the near future.

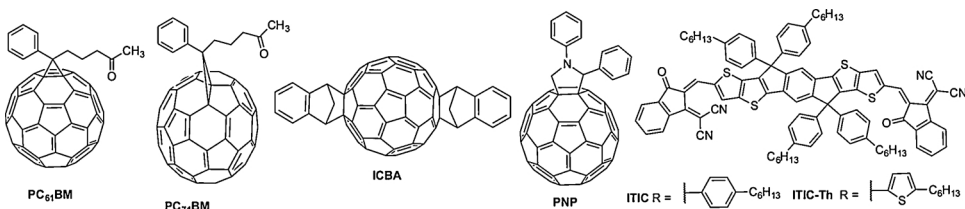
For IPV applications, fullerene-based acceptors are advantageous for their well-matching absorption range to indoor lightings and superior electron-transporting features. The popular fullerene-based acceptors (**PC₆₁BM**, **PC₇₁BM** and **ICBA**) are shown in Scheme 4. Among them, **PC₆₁BM** and **PC₇₁BM** were mostly used to blend with tailor-made either small or polymeric donor due to the commercial availability and easy device fabrication for achieving IPVs with good PCEs. Recently, non-fullerene acceptors are emerging as even more potential candidates due to their high flexibility of molecular designs that can tune the optical and electronic properties to well match with the indoor light sources. [199] In OSCs, the complimentary absorption of donor and acceptor blend enables broad spectral coverage ranging from UV-vis to NIR region. The molecular design strategy for polymeric/small molecular donors and acceptors with enlarged optical energy gaps needs to simultaneously consider the impacts of molecular structure on active layer morphologies, which are the most crucial factors for governing the overall PCE [189–200].

Initially, some reports based on optical simulations explained the appropriate absorption range of active materials toward indoor light, and the impact of R_{sh} on the final PCE of the IPV. The appropriate absorption ranges of active materials for IPVs are mainly on 350–700 nm, and thus the materials with absorption out of this region are not particularly useful for indoor light harvesting. [76] Caironi and co-workers designed a simple and scalable technique for the direct transfer of selective poly(3,4-ethylenedioxythiophene)/polystyrene sulfonate (PEDOT:PSS) onto a blend film of **P3HT:PC₆₁BM** for making OSCs. [67] The device was printed on a commercial temporary tattoo paper to simplify the fabrication process and to avoid surface treatments. As a result, the device showed a higher PCE of 7.5% under 500 lx of a fluorescent tube. Later, Kim and co-workers improved the PCE of an OSC device with **P3HT:ICBA** as the active blend to 8.8% under the irradiance of a LED light at 1000 lx. [201] The high PCE of **P3HT:ICBA** is due to the absorption of **P3HT** donor nicely overlaps with the LED emission peaks in addition to the better matching of donor and acceptor energy levels within the active layer. A low-cost un-doped ZnO film as transparent conducting electrode was reported by Shim and co-workers. The OSC with the active layer **P3HT:ICBA** on the ZnO transparent

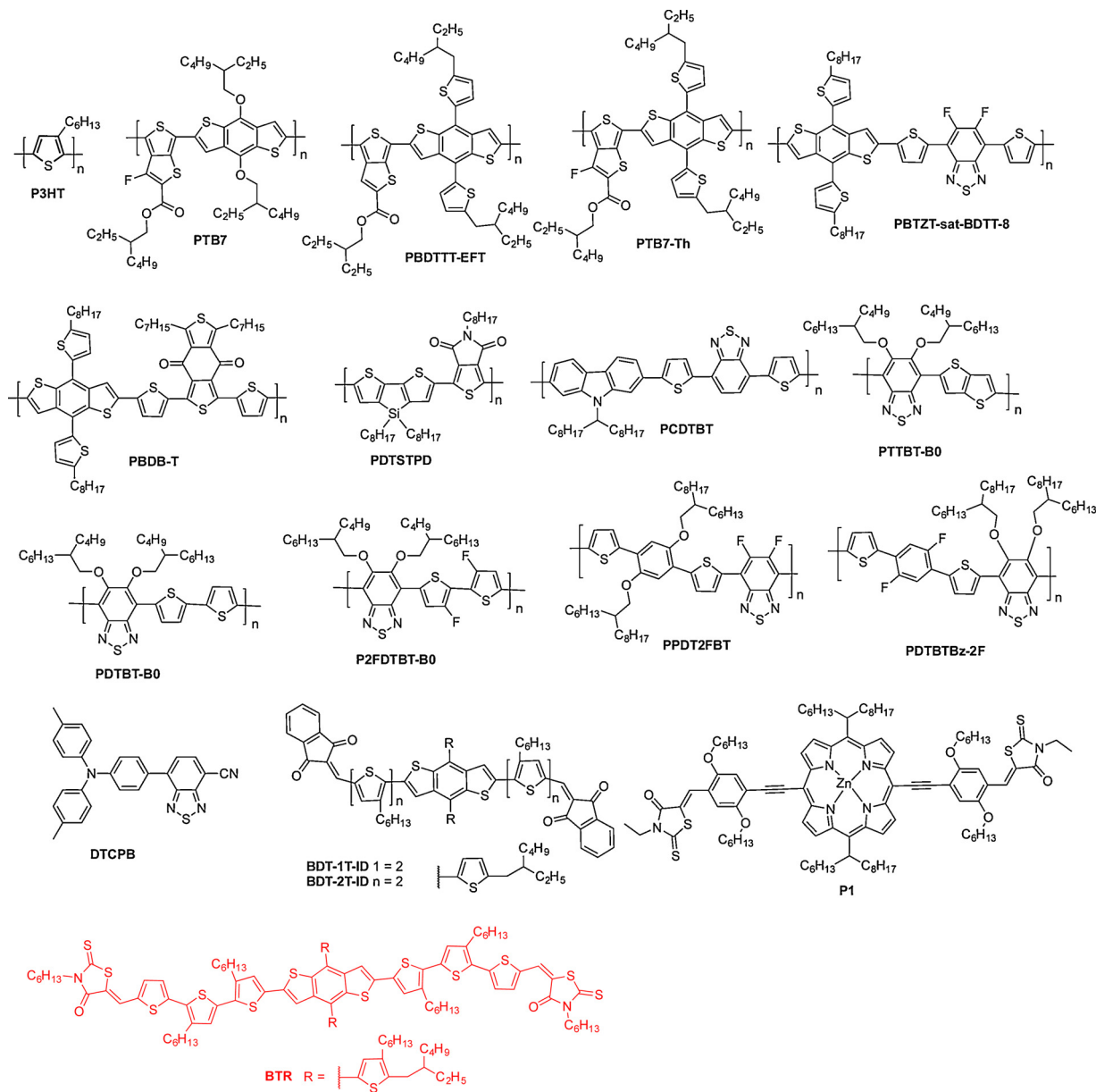
electrode produced a higher PCE of 9.5% under a LED lamp with a luminance of 500 lx when compared to its reference device (PCE of 8.5%) based on an ITO electrode. In addition, the undoped ZnO electrode can reduce production cost of OSC about 20%, revealing the potential for practical commercialization as compared to typical reference electrode such as ITO. [202] Very recently, Kim and co-workers incorporated quasi-amorphous ZnO/Ag/ZnO as the transparent conducting electrode for OSC incorporating the **P3HT:ICBA** blend as the active layer. [203] As a result, the device gave an enhanced PCE up to 12.1% due to excellent transparent conducting electrode property with transmittance (92%) in the visible region and smooth electrode surface. Later, they further modified the cathode layer by Ni-doped indium tin oxide which enables substantial resistance reduction and retains high transmittance and low cathode surface roughness. It results a boosting in PCE up to 14.6% under the 1000 lx LED [204].

In addition to **P3HT**, Chen and co-workers reported the use of a polymeric donor **PBDTTT-EFT** (Scheme 5) blending with three different acceptors (**PC₆₁BM**, **ICBA** and **PC₇₁BM**) for indoor OSC applications. [205] Among these six combinations, the OSC device with **P3HT:ICBA** blend showed the highest J_{SC} of $50 \mu\text{A cm}^{-2}$ and V_{OC} of 0.73 V, resulting a superior PCE of 13.76% and P_{max} of $22.5 \mu\text{W cm}^{-2}$ under the irradiance of a T5 light (500 lx) due to the better spectral coverage and high LUMO of **ICBA** acceptor. [68] Mori and co-workers used **PTB7-Thz** donor to blend with **PC₇₁BM** acceptor to improve the blend absorption and morphology. The OSC device with the active layer **PTB7-Thz:PC₇₁BM** showed a high FF of 0.74 and a PCE of 11.63% and P_{max} of $42.3 \mu\text{W cm}^{-2}$ under the illumination of a LED light (890 lx). [71] Similarly, the blend composed of **PTB7-Th:C70** showed two fold PCE (9.2%) under low illumination as compared to that measured under 1-sun illumination. The result indicates that there is a sub-linear dependence of J_{SC} on light intensity along with increasing FF at reduced illumination. [206] In another report, Tsoi and co-workers judiciously chosen the donors **P3HT**, **PTB7** and **PCDTBT** (Scheme 5) blending with **PC₇₁BM** to ensure the wide absorption and better alignment of energy levels of donor and acceptor. [66] All OSCs devices in this work showed similar J_{SC} , but the device with **PCDTBT** as donor showed a higher PCE (16.6%) thanking to the low HOMO which gives a higher V_{OC} of the device.

In order to minimize the dark current, optimizing device fabrication process is one of the most important issues to enhance the PCE of IPVs. In this line, Arias and co-workers reported the incorporation of polyethylenimine ethoxyl as ETL for the device configured with **PCDTBT:PC₇₁BM** blend as the active layer improved the PCE from 0.6% to 11.5% under 300 lx of fluorescent lamps. [69] For improving the spectral coverage, So and coworkers reported a ternary blend **PCDTBT:PDTSTPD:PC₇₁BM** to further enhanced the PCE to 20.80% and P_{max} of $15.4 \mu\text{W cm}^{-2}$ under fluorescent lamps at 300 lx. As compared to the previous binary blend, the ternary blend solar cells give a higher J_{SC} due to the better matching of the absorption of blend films with the emission spectra of indoor light sources. Moreover, the ternary blend films showed better hole-transporting properties which lead to higher FFs and then better PCEs. [55] By taking inspiration from this result, Shim and co-workers demonstrated the utilization of a quaternary BHJ blend composed of **PCDTBT:PTB7:PC₆₁BM:PC₇₁BM** for indoor light energy harvesting applications. [207] Quaternary BHJ was constructed mainly to improve the blend absorption, morphology,



Scheme 4. Chemical structures of electron transport materials for solar cell applications.



Scheme 5. Chemical structures of organic sensitizers for indoor OSCs.

and the charge transport properties of the photovoltaic device. The device with optimized blend **PCDTBT:PTB7:PC61BM:PC71BM** (5:5:3:12) showed a PCE of 10.6% due to high R_{sh} and low R_s under a white LED with illumination of 500 lx. For study the practical application of IPV, Colsman and co-workers integrated the solution-processed OSCs onto sunglasses equipping a microelectronic circuit to make a self-powered smart application. [208] For this application they used a ternary blend **PBTZT-stat-BDTT-8:PC61BM:PC71BM** and examined the device characteristics under different illuminated light sources. The device showed a highest PCE of 6.7% under the white light LED at 500 lx when compared to the low efficiency (0.06%) upon testing under the standard 1-sun illumination. It clearly demonstrates that the unique properties of this integrated indoor OSC can sustain as self-powered electronics and serve for consumer-oriented mobile applications. In a very recent report, Lee and co-workers made a ternary blend OSCs by adding a non-fullerene acceptor **EP-PDI** into a blend of **PTB7:PC71BM**. This ternary blend based OSCs improved the PCE to 15.68% due to their high absorption in the visible region and the crystalline property of **EP-PDI** which improves the charge transport

properties. [209] Extending this strategy further, Ko and co-workers made a semitransparent OSCs by using quaternary blend composed of donors (**PTB7-Th:PBDB-T**), fullerene acceptor (**PC71BM**) and non-fullerene acceptor (**ITIC-Th**) in order to efficiently cover the indoor absorption, leading the new OSC device to deliver a high PCE of 15.5% under a LED light illumination of 1000 lx. [210]

In OSC device, low R_s and high R_{sh} are the basic criteria to minimize the leakage currents for attaining high PCE. To fulfill these pre-requirements, the blend morphology should be semi-crystalline to balance the charge transport and recombination processes. Along this line, Kim and coworkers synthesized semi-crystalline alkox-ybenzothiadiazole-based polymers **PTTBT-BO**, **PDTBT-BO** and **P2FDTBT-BO** (Scheme 5). [211] These new polymeric donors were blended with **PC71BM** respectively and examined the device characteristics under standard 1-sun illumination as well as dim light conditions. The OSC device employing **P2FDTBT-BO:PC71BM** blend gave the improved PCE from 3.69% under standard 1-sun illumination to 8.33% under the dim light irradiance of 2.5 mW cm^{-2} mainly due to the exceptionally high R_{sh} . Among them, the device with **PDTBT-**

BO:PC71BM blend showed the highest PCE of 9.6% under dim light condition due to high R_{sh} as well as low R_s . In addition, they explored the feasibility of introducing a popular non-fullerene acceptor **ITIC** for blending with donors (**PTTBT-BO**, **PDTBT-BO**, and **P2FDTBT-BO**). Unfortunately, the resulting device only produced an inferior PCE of 6.5% due to the high R_s and low R_{sh} . Since the crystalline property is very important parameter, Shim and co-workers blended a wide gap polymer donor (**PPDT2FBT**) with **PC71BM** to achieve OSC device with a high PCE of 16.0% and P_{max} of $44.8 \mu\text{W cm}^{-2}$ due to the semi-crystallinity of blend. The device shows high R_s and low R_{sh} which results the improvement of J_{SC} ($117 \mu\text{A cm}^{-2}$) and V_{OC} (0.59 V) and FF (0.65) under a LED light illuminance of 1000 lx (Table 3). [212] Later, the same group modified the donor structure by inter-changing the position of fluorine and alkoxy groups for well-matching of the absorption along with the required semi-crystalline property [213]. As a result, OSC device based on **PDTBTBz-2F:PC71BM** blend achieved a high PCE of 23.1%, P_{max} of $66.0 \mu\text{W cm}^{-2}$ and high V_{OC} of 0.82 V under a LED source of 1000 lx illumination.

Instead of using polymeric donor, So and coworkers utilized a porphyrin-based donor **P1** to blend with **PC71BM**, this small molecule-based OSC showed a promising PCE up to 19.2% under 300 lx of a LED tube. [116] The superior efficiency is due to the better hole transport feature and reduced energetic defects of **P1:PC71BM** blend. More interestingly, this small-molecule based OSC device showed better stability up to 180 min (80% off from the peak PCE of 19.2%) as compared to that of device based on **PCDTBT:PC71BM** blend under the same testing conditions. The improvement on the stability of IPV cells is a

great challenge and needs to be solved by introducing suitable blend films together with device engineering techniques for future commercialization. In this regard, Tsoi and coworkers used a promising dithienobenzene-based small-molecule donor **BTR** as indoor light harvester in combination with **PC71BM** as electron acceptor for making indoor OSC device. [42] The indoor OSC device based on **BTR:PC71BM** blend achieved a record-high PCE up to 28.1% under a fluorescent lamp of 1000 lx, which is three times higher than that of the same device tested under 1-sun solar radiation. The high PCE of OSC device employing the blend of **BTR:PC71BM** as active layer is mainly ascribed to the well matching of blend absorption with the fluorescent lamp as well as the balance of crystallinity and phase separation of the blend film. Recently, Arai and co-workers modified the dithienobenzene core with indanediione as terminal acceptor units through oligothiophene bridge to make **BDT-nT-IDs** ($n = 1, 2$) as new electron donors for better matching the absorption toward the LED light. [214] The OSC device based on **BDT-2T-ID:PNP** blend achieved a high PCE of 16.2% and P_{max} of $12.3 \mu\text{W cm}^{-2}$. This device was applied for a real self-sustainable electronic application with a six series connected module that can generate a high output power surpassing $100 \mu\text{W}$ and a high V_{OC} (4.2 V) under indoor light conditions of 200 lx. Most of the reported indoor OSC device were fabricated by solution-processed method. A recent report by Wong and coworkers made a vacuum-deposited OSC device based on a D-A-A configured electron donor **DTCPB** composed of benzothiadiazole as central acceptor for red-shifting the absorption to visible region. The optimal device employing **DTCPB:C70** blend as the active layer showed a PCE $\sim 16\%$ under a TLD-840 fluorescent lamp

Table 3
Optical, electronic and photovoltaic properties of organic donor/acceptor based IPVs.

Indoor Light Source	Light Intensity (lux)	Organic donor	Organic acceptor	J_{SC} ($\mu\text{A cm}^{-2}$)	V_{OC} (V)	FF	PCE (%)	P_{max} ($\mu\text{W cm}^{-2}$)	Ref.
T5 fluorescent lamp	500	P3HT	PC61BM	36	0.47	0.62	7.48	–	[67]
LED	1000	P3HT	ICBA	147	0.69	0.62	8.80	–	[201]
TL5	500	P3HT	PC61BM	62	0.43	0.59	9.59	15.8	[68]
LED	500	P3HT	PC61BM	62	0.43	0.59	8.90	15.7	[68]
TL5	500	P3HT	ICBA	50	0.73	0.62	13.76	22.5	[68]
LED	500	P3HT	ICBA	50	0.73	0.63	13.05	22.9	[68]
LED	500	P3HT	ICBA	36	0.64	0.69	9.50	–	[202]
LED	500	P3HT	ICBA	44	0.68	0.68	12.10	–	[203]
LED	1000	P3HT	ICBA	104	0.56	0.60	14.60	–	[204]
TL5	500	PBDTTT-EFT	PC71BM	63	0.58	0.59	13.14	21.6	[68]
LED	500	PBDTTT-EFT	PC71BM	66	0.59	0.58	13.20	23.2	[68]
Fluorescent lamp	300	P3HT	PC61BM	21	0.41	0.56	5.80	4.8	[66]
Daylight color LED	890	PTB7-Th	PC71BM	92	0.62	0.74	11.63	42.3	[71]
Fluorescent lamp	300	PTB7	PC71BM	29	0.61	0.69	14.60	12.2	[66]
Fluorescent lamp	300	PCDTBT	PC71BM	28	0.72	0.69	16.60	13.9	[66]
LED	300	PCDTBT	PC71BM	28	0.70	0.46	8.70	9.0	[69]
CFL	300	PCDTBT	PC71BM	54	0.74	0.53	11.50	20.7	[69]
Incandescent bulb	300	PCDTBT	PC71BM	17	0.65	0.34	0.60	3.8	[69]
Fluorescent lamp	300	PCDTBT	PC71BM	31	0.70	0.56	16.50	12.2	[55]
Fluorescent lamp	300	PCDTBT:PDTSTPD	PC71BM	33	0.73	0.63	20.80	15.4	[55]
LED	300	PCDTBT	PC71BM	31	0.70	0.57	16.20	12.5	[55]
LED	300	PCDTBT:PDTSTPD	PC71BM	33	0.73	0.61	19.00	14.6	[55]
White LED	500	PCDTBT: PTB7	PC61BM:PC71BM	44	0.58	0.71	10.6	18.0	[207]
White LED	500	PBTZT-stat-BDTT-8	PC61BM :PC71BM	50	0.53	0.47	6.70	12.5	[208]
LED	500	PTB7	EP-PDI :PC70BM	57	0.65	0.69	15.68	–	[209]
LED	1000	PTB7-Th: PBDB-T	PC71BM: ITIC-Th	99	0.67	0.65	15.46	–	[210]
Dim light	2.5 ^a	PTTBT-BO	PC71BM	280	0.82	0.40	3.57	–	[211]
Dim light	2.5 ^a	PDTBT-BO	ITIC	130	0.84	0.60	2.67	–	[211]
Dim light	2.5 ^a	P2FDTBT-BO	PC71BM	360	0.75	0.77	9.60	–	[211]
Dim light	2.5 ^a	P2FDTBT-BO	ITIC	300	0.82	0.67	6.48	–	[211]
LED	1000	PPDT2FBT	PC71BM	117	0.59	0.65	16.00	44.8	[212]
LED	1000	PDTBTBz-2F	PC71BM	112	0.82	0.70	23.10	66.0	[213]
Fluorescent lamp	1000	BTR	PC71BM	133	0.79	0.75	28.10	78.2	[42]
White LED	200	BDT-2T-ID	PNP	24	0.75	0.68	16.20	12.3	[214]
LED	300	P1	PC71BM	30	0.76	0.66	19.15	14.9	[116]
TLD-840	800	DTCPB	C70	79	0.72	0.64	15.78	36.6	[215]

^amW cm⁻².

(800 lx). [215] The good device performance was attributed to the strong visible absorption of **DTCPB:C70** blend together with the anti-parallel dimeric crystal packing of **DTCPB** which favors the morphology for better charge transporting and reduced exciton recombination. This work was accomplished by adopting the mature vacuum deposition technology that has been commercialized for organic light-emitting diode (OLED) devices. In other words, this result may open a new opportunity for material development since the basic requirement of electron donor suitable for indoor OSCs is the visible light absorption, which can be feasibly achieved by conjugated molecule with limited molecular weight that is necessary for vacuum process.

In summary, the OSC-based IPV with an active layer composed of dithienobenzene-based donor **BTR** and fullerene acceptor **PC71BM** reported by Tsoi and co-workers delivered the best PCE of 28% so far under a fluorescent lamp (1000 lx). This work clearly reveals that achieving better and effective phase separation of nano-crystallized active layer is very important for developing efficient IPVs. Therefore, feasible approaches that enable organic materials to have appropriate crystalline sizes together with preferable face-on interactions in active layer can enhance the R_{sh} and high V_{oc} , thus high efficiency. Developing novel donors and acceptors in active layer by suitable molecular designs in conjunction with new fabrication techniques can further promote the progress of OSC-based IPVs in the near future.

3.4. Perovskite materials for indoor photovoltaics

For the last decade, the research activities for perovskite-based PVs are explosively booming. Interestingly, although the low band gap (1.6 eV) of $\text{CH}_3\text{NH}_3\text{PbI}_{3-x}\text{Cl}_x$ is able to perfectly cover the UV-vis absorption region, with additional absorption in IR region, which is anticipated to be additional for the most of the indoor lighting, perovskites are still perfectly suitable for indoor light sources mainly due to the low exciton binding energy and long charge carrier diffusion length as well as high carrier mobility. [44–46] The device structure of PSCs is basically configured with two types of architectures such as (a) mesoporous and (b) planar configuration (Fig. 12). The working principle is shown and explained in Fig. 12. Similar to DSSC configuration, mesoporous PSCs also fulfill the porous structure of TiO_2 adsorbed with perovskite materials and then covered with HTL. In this configuration, the mesoporous TiO_2 layer act as substrate to load the perovskite material as well as electron transportation and HTL for hole transportation. Since the perovskite posses long carrier diffusion length (1 μm) it allowed fabricating a dense packed planar perovskite film to harvest more light. For planar PSCs, perovskite film is sandwiched between ETL and HTL. It was either in the form of conventional PSCs (FTO/ETL/

perovskite/HTL/counter electrode) and inverted planar PSCs (FTO/HTL/perovskite/ETL/counter electrode) shown in Fig. 12. The conventional and inverted PSCs mainly differ in the exchange of the position of ETL and HTL near to anode and cathode. The ETLs are typical n-type oxide semiconductors (TiO_2 , ZnO , MgO and SnO_2) for conventional or fullerene derivatives for inverted PSCs, whereas the HTLs are typical organic electron-rich π -conjugated materials. The working principle of perovskite cells involves (1) the light absorption of perovskite generates exciton, which diffuses within perovskite crystalline grains, (2) the electron injects into electron ETL, (3) hole transfers to HTL, (4) the charge carriers are subsequently collected by the counter electrodes and generates photocurrent. [44–46,216] However, undesired electron recombination and back electron transfer can deteriorate the PCE of PSCs.

For the first time, Lin and co-workers reported perovskite ($\text{CH}_3\text{NH}_3\text{PbI}_{3-x}\text{Cl}_x$) as an active layer to construct PV cell under dim light conditions. [51] Various ETLs (**C60**, **C70** and **PC61BM**) were judiciously selected together with the optimization of fabrication process for controlling the traps in the active layer as well as carrier dynamics for better devices. The PSCs with two-step deposited **PC61BM** as ETL produced the highest PCE of 27.4% under the light source of a T5 fluorescent lamp (1000 lx) due to its low charge transfer resistance and then a high V_{oc} of 0.85 V. The structural nature of perovskite makes the high stability PSCs a great challenge. In this regard, photoactive polymers such as acrylate and epoxy polymers shown in Scheme 6 were used to encapsulated the perovskite to improve the thermal stability and effective hole extraction which lead to PCE of 20% and P_{max} of 64.9 $\mu\text{W cm}^{-2}$ under a Panasonic LED light (320 lx). The encapsulation of photoactive perovskite layer helps to double the external quantum efficiency under indoor lighting than outdoor conditions due to the better spectral matching of indoor light with the perovskite devices. It indicates that the photoactive polymers can be successfully integrated in perovskite devices and effectively extract the holes from the perovskite interface owing to its outstanding electron-blocking nature. [217] PSCs are more stable at low light intensity and show a photovoltaic response even at lower light intensities ($10^{-2} \text{ mW cm}^{-2}$) when compared to crystalline silicon solar cells. A constant current is observed at low light intensity that is originating from a capacitive current which typically leads to overestimate the performance of PSC (more than 100%) and DSSC (over 10%). In general, lower capacitance of PSC ($37.9 \mu\text{Fcm}^{-2}$) at the interfacial contacts results in the hysteresis gap observed in I-V curves of the device. In this context, MPPT technique combined with LED solar simulators with a wider range of light intensities suggest for better photovoltaic parameters. [166] Ishikawa and co-workers studied the photovoltaic parameters of PSCs under low light intensities and

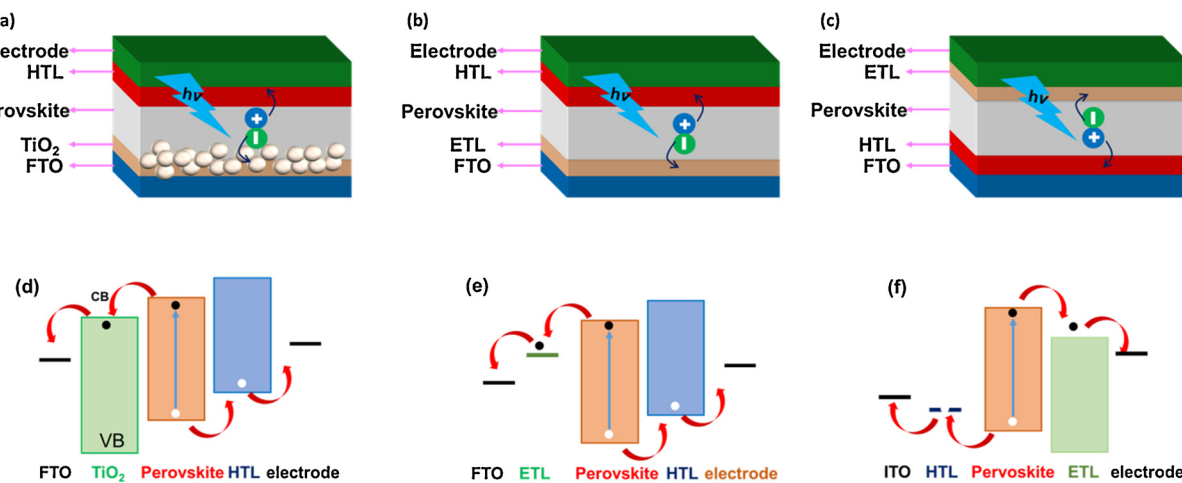
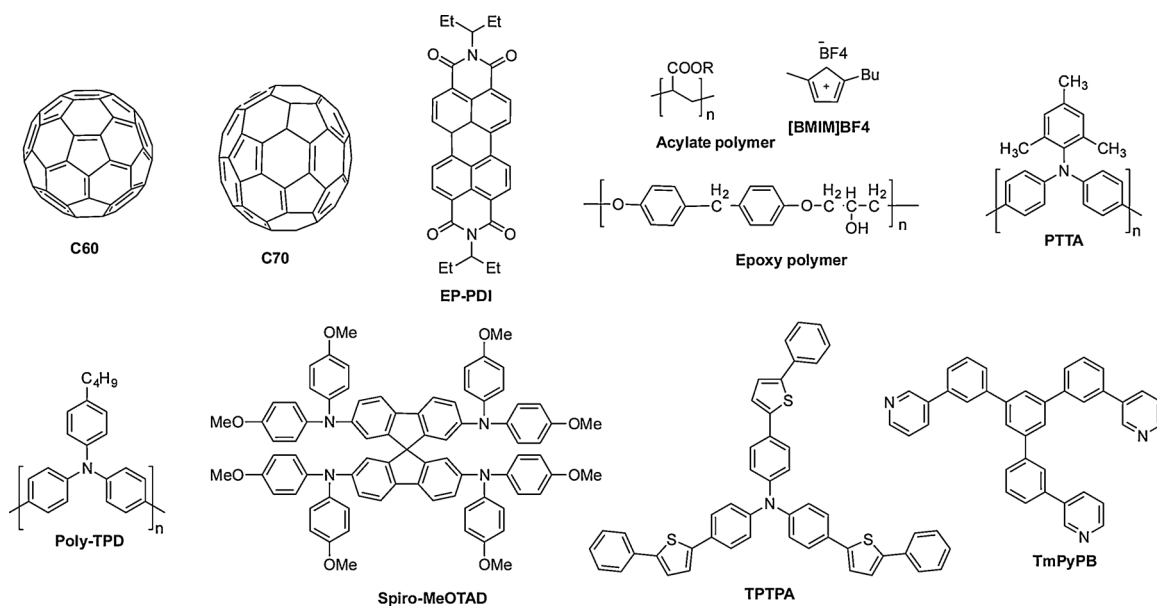


Fig. 12. Typical schematic device configuration of (a) mesoporous TiO_2 film, (b) planar and (c) inverted PSC architectures and their working principles (d, e, and f, respectively).



Scheme 6. Chemical structures of ETLs, HTLs and components in device for indoor perovskite solar cells.

found that the PSC devices exhibited higher V_{OC} even under 0.1 mW cm⁻² illumination. Under the various light intensities, the J_{SC} of the device is in proportional relation with light intensity, however, the V_{OC} is not proportional and remains unchanged at about 70% of its initial value. [218]

In order to get low defect densities of perovskite thin films, vacuum deposition technology has been utilized to make high quality perovskite thin films, which was combined with **C60** as the ETL to make PSCs. [219] The small area device based on the vacuum-deposited perovskite showed the better photovoltaic parameters (J_{SC} of 139 $\mu\text{A cm}^{-2}$, V_{OC} of 0.91 V, FF of 0.75 shown in Table 4) and high PCE of 30.1% and P_{max} of 94.9 $\mu\text{W cm}^{-2}$ under a fluorescent lamp illumination of 1000 lx as compared to that of solution-processed perovskite devices. In addition, these vacuum-fabricated PSCs showed remarkable stability up to one year with simple epoxy encapsulation in the absence of any desiccant. This result clearly indicates that vacuum-deposited PSCs are promising candidate for indoor light energy harvesting and may serve as potential power source for the future IoT applications.

In planar PSCs, the incorporation of suitable interfacial layers can boost the electron transport and extraction processes and reduce the sheet resistance to improve the PCE. Also, the interfacial layers can act as a protective layer in order to prevent the erosion of moisture and oxygen into the perovskite film, and thus improve the most desirable thermal stability. In this scenario, the developments of interfacial layers were extensively explored either in upper or lower layers near anode or cathode, respectively. For example, Wang and co-workers modified the interface between ETL (**PC61BM**) and cathode (Ag) by incorporating an ionic liquid of 1-butyl-3-methylimidazolium-tetrafluoroborate ([BMIM] BF₄) (shown in Scheme 6) to make PSCs with the device configuration of FTO/NiO_x/CH₃NH₃PbI₃/**PC61BM**/[BMIM]BF₄/Ag. [52] The incorporated [BMIM]BF₄ efficiently passivate the surface traps and facilitate the electron extraction and transportation, leading to a record-high PCE of 35.2% under 1000 lx illuminance of a fluorescent lamp.

In most of the perovskite PVs, **spiro-MeOTAD** (Scheme 6) is the most popular and extensively used HTL due to its good solubility, visible absorption, good film-forming nature, and high hole mobility. [50,216,220–227] Researchers taken this evergreen material in combination with newly developing/modifying electron-transporting materials for better PCEs. Along this line, Brown and co-workers extensively studied and developed various types of electron transport materials [225,226]. They constructed CH₃NH₃PbI₃:**spiro-MeOTAD**

based PSC by incorporating low temperature compact TiO₂ layer and mesoporous TiO₂ layers. In this device, the mesoporous TiO₂ layers can effectively work even under low light illumination due to its very low dark current and reverse dark currents. The obtained indoor perovskite PVs achieved a high PCE of 25.4% and P_{max} of 32.6 $\mu\text{W cm}^{-2}$ under 400 lx CFL illumination. Additionally, they made flexible PSCs by modifying the ETL with SnO₂/mesoporous-TiO₂ to deliver a PCE of 13.32% under a 400 lx LED illumination. [230] The device characteristics are ascribed to the presence of a mesoporous TiO₂ scaffold layer over SnO₂ that facilitates higher rectification ratios, lower R_S and higher R_{sh} . Later, the same group further improved the PCE up to 26.9% by using SnO₂/MgO composite ETLs of a device configured as ITO/SnO₂/MgO/CH₃NH₃PbI₃/**Spilo-MeOTAD**/Au, which was then examined under similar light conditions. [231] In this new device configuration, the thin MgO layer over SnO₂ favors the formation of uniform films (ITO/SnO₂/MgO), leading to the suppression of interfacial charge-carrier recombination, and thus afford better stability. Therefore, it is evident that the PCE of PSCs strongly depends on the purity of crystalline perovskite films and morphology control as well as the materials employed to encapsulated the perovskite layer.

The developments of real ambient fabrication techniques are emergently required for the commercialization of perovskite devices. [232] In this context, Feng and co-workers developed air knife assisted recrystallization technique by the immersion of nanoporous PbI₂ film in the methylammonium iodide/chloride bath. [233] In this way, the resulted perovskite film enhances the crystallinity with pure domains and low trap density, rendering the perovskite IPVs with an excellent PCE of 27% under a 2000 lx T5 fluorescent light illumination at ambient conditions. In another report, Tsai and co-workers studied indoor PSCs by a set of benchmark device architectures such as mesoporous perovskite and inverted perovskite with alternative HTLs, and carbon-based PSCs [234]. Among them, mesoporous perovskite with a typical HTL (**Spilo-OMeTAD**) exhibited a highest P_{max} of 115.6 $\mu\text{W cm}^{-2}$ under 1000 lx illuminance of fluorescent lamps. When the HTL was replaced by **PTAA** (Scheme 6) in the device, the P_{max} drops to almost zero under indoor lighting while both HTLs showed similar PCEs under 1-sun conditions. It indicates that the PCE of PSCs under indoor light sources are much influenced by their leakage currents. Similarly, in the case of inverted PSCs with **Poly-TPD** as a HTL achieved better P_{max} (indoor) than the one employed PEDOT:PSS due to the higher leakage current of PEDOT:PSS layer. However, the HTL-free carbon-based PSCs

Table 4
Optical, electronic and photovoltaic properties of perovskite IPVs.

Indoor Light Source	Light Intensity (lux)	Device configuration	J_{sc} ($\mu\text{A cm}^{-2}$)	V_{oc} (V)	FF	PCE (%)	P_{max} ($\mu\text{W cm}^{-2}$)	Ref.
T5 fluorescent lamp	1000	ITO/PEDOT:PSS/perovskite/one-step PC61BM/1,3,5-tri(m-pyrid-3-ylphenyl)benzene(TmPyPB)/Ag	134	0.76	26.00	—	—	[51]
T5 fluorescent lamp	1000	ITO/PEDOT:PSS/perovskite/two-step PC61BM/1,3,5-tri(m-pyrid-3-ylphenyl)benzene(TmPyPB)/Ag	132	0.84	27.40	—	—	[51]
T5 fluorescent lamp	1000	ITO/PEDOT:PSS/perovskite/C60/1,3,5-tri(m-pyrid-3-ylphenyl)benzene(TmPyPB)/Ag	109	0.70	0.57	5.50	—	[51]
T5 fluorescent lamp	1000	ITO/PEDOT:PSS/perovskite/C70/1,3,5-tri(m-pyrid-3-ylphenyl)benzene(TmPyPB)/Ag	105	0.57	0.46	10.00	—	[51]
LED	1000	$\text{CH}_3\text{NH}_3\text{PbI}_3$:spiro-MeOTAD	118	0.79	0.70	19.80	64.9	[217]
CFL	400	glass/TIO and glass/FTO of the type TCO/c-TiO ₂ /meso-TiO ₂ /CH ₃ NH ₃ PbI ₃ /Spiro-O-MeOTAD/Au	58	0.78	0.72	25.40	32.6	[229]
LED	400	ITO/TiO _x /CH ₃ NH ₃ PbI ₃ :spiro-MeOTAD/Au	34	0.63	0.77	12.10	16.0	[228]
Fluorescent lamp	1000	FTO/NiO _x /CH ₃ NH ₃ PbI ₃ /PC61BM/BMMIMBF ₄ /Ag	150	0.87	0.75	35.20	—	[52]
Fluorescent lamp	1000	FTO/c-TiO ₂ /m-TiO ₂ /ZrO ₂ /m-carbon/CH ₃ NH ₃ PbI ₃	14	1.10	0.66	18.00	10.0	[235]
LED	400	ITO/SnO ₂ /MgO/CH ₃ NH ₃ PbI ₃ :spiro-MeOTAD/Au	65	0.90	0.72	26.90	41.6	[231]
LED	400	SnO ₂ /meso-TiO ₂ /CH ₃ NH ₃ PbI ₃ :spiro-MeOTAD	40	0.84	0.53	13.32	19.2	[230]
T5 fluorescent light	2000	ITO/SnO ₂ /Perovskite/PC61BM/Bathocuproine (BCP)/Ag	240	0.90	0.75	27.00	—	[233]
Fluorescent lamp	1000	ITO/MoO ₃ /tris[4-(5-phenylthiophen-2-yl)phenyl]amine (TPPTPA)/perovskite/C60/1,3,5-tri(m-pyrid-3-yl-phenyl)benzene (TmPyPB)/Ag	135	0.88	0.75	30.10	94.9	[219]

exhibited a promising P_{max} (89.4 $\mu\text{W cm}^{-2}$) under 1000 lx. This configuration was further successfully utilized to make a large scale panel ($5 \times 5 \text{ cm}^2$) serving as a demonstration for the feasibility of practical applications. Watson and co-workers developed a promising printable perovskite device architecture based on mesoporous layer made of overlapping titania, zirconia and carbon layers for both the advantages of low-cost and outstanding stability. [235] Under a fluorescent lamp of 1000 lx, this printable PSCs exhibited a high PCE of 18% and P_{max} of 10.0 $\mu\text{W cm}^{-2}$ due to the patterning of the blocking layer (titania and zirconia) that improved both V_{oc} and FF. Also, these devices showed good stability even after working for hundred hours under 70% room humidity that still exhibited a PCE as high as 6.6%.

In conclusion, due to the remarkable optical and electronic properties, perovskites are currently performing excellent efficiency for PV applications under indoor conditions. The perovskite-based IPVs with a modification of ionic liquid on top of **PC61BM** produced a record PCE of 35% under a fluorescent lamp (1000 lx) was reported by Wang and his co-workers. The record-high efficiency indicates a bright direction of perovskite-based PVs for IPV applications. There are even more rooms for the innovative developments of new hole- and/or electron-transporting materials as well as interfacial materials to facilitate the exciton extraction efficiency, to control the quality and size of crystals, and to improve the stability. In spite of material engineering works, new inputs on fabrication processes and device structures are also important as we practically consider applying perovskite-based PVs for IPV applications.

4. Conclusions and prospects

In conclusion, the future large demand of sustainable energy source for low-power consumption applications will greatly stimulate the growth of IPVs technology. Since the indoor lights typically deliver lower light intensity with various emission spectra depending on the natures and lighting mechanisms, this review firstly classified the indoor lights and summarized their characteristics, and highlighted the cautious points for the determination of the efficiency for the IPV devices under ambient conditions. In order to escape from the general over-estimation/underestimation on the PCE of a specific IPV device, particular attentions should pay for the accuracy of calibrated lux meter by NIST-traceable calibration (e.g. Extech LT40-NIST) is recommended, and stable irradiance during the measurement and precisely fixed source-device distance. In addition, the prior knowledge of the light source spectrum is highly recommended for getting a more accurate P_{in} from L . Among the various indoor light sources, fluorescent and LED lamps perform as the most energy-saving lighting for our daily life, which also showed the highest PCE in most of the IPV cases owing to their narrower spectral widths without the low-photon-energy IR emission. In principle, all materials for outdoor PVs may also be useful for IPVs, but there are some fundamental requirements for IPV materials such as sufficient absorption range between the 350–700 nm with high molar extinction coefficient. Based on the reported works on various IPVs, this review classified the utilized materials into four different categories that mainly are inorganic silicon and III-V semiconductors, dye sensitizers, organic electronic donors and acceptors, and perovskites depending on their structural properties and working principles of photovoltaic device. The structure-property-efficiency relationship of the materials in individual class was highlighted together with their challenge and perspective. Among inorganic materials, gallium based materials (GaAs and InGaP) performed very impressive PCE at low irradiance levels due to the suitable optical energy gap nicely responding to indoor lightings, low dark current, and highest surface density. However, these materials are suffering from high production cost due to the difficulties on the purification as well as the formation of defect-free crystals. The whole production process essentially needs high energy and inevitably produces chemical wastes, both of them have substantial impacts on the global environment, setting up the

great challenges for further large scale applications. In addition, flexible IPV panels have advantages for fitting to the large scope of household applications such as smart windows and IoTs sensors. However, flexible inorganic material-based IPV needs a micro-meter thin active layer, which typically produces a lower PCE. The demanding and challenges will definitely stimulate the development of better inorganic materials produced by environmental benign methods and suitable flexible film technologies in the near future.

Since the indoor light intensity is much weaker as compared to that of the outdoor sunlight, the typical inferior photo-stability issue of organic materials for conventional solar PVs may not be as crucial as usual, giving a great opportunity for organic IPV material developments. In addition, the strategies to modulate the absorption profiles of organic materials are more feasible as considering them for IPV application adopting the light-to-current conversion mechanism based on DSSCs and OSCs. For DSSC-based IPVs, the best device with a PCE up to 32% has been successfully realized with a co-sensitizer composing of dithienocyclopentadiene based dyes (**XY1b:Y123**), indicating the potential of co-sensitized approach that can perform better spectral overlap with indoor lighting, perfect matching of energy levels and compact packing on TiO_2 to enhance J_{SC} and V_{OC} and then PCE. From the structural design points of view, the ideal dyes for DSSC with highly intense 350–700 nm absorption will largely limit the choice of aromatic units. Particular attentions should pay for the molecular features that can (1) satisfy the spectral response to indoor lights, (2) lead to compact packing on TiO_2 with reduced flexibility of anchoring modes, (3) reduce electron recombination and dark current, (4) lower down the HOMO level to create more space for electrolyte development that eventually increases the V_{OC} . For a further practical application, the DSSC-based IPVs need to face the long-standing challenges concerning on the stability.

For OSC-based IPVs, the champion case that gave the best PCE of 28% was achieved by employing the active blend composed of a central symmetric donor (**BTR**) with dithienobenzene as electron rich central moiety and rhodamine as terminal group in combination with a fullerene acceptor **PC71BM**. The excellent performance was attributed to the suitable nanophase separation and face-on orientation in the active layer. The fullerene acceptors are still dominant in IPV applications due to their well-matching absorption range and superior electron-transporting features. However, the emergence of non-fullerenes acceptors may create a big momentum for promoting the progress of OSC-based IPVs. Nevertheless, for further enhancing the efficiency of OSCs for IPVs, the molecular structure engineering implementing on the polymeric/small molecular donors and acceptors with enlarged optical energy gaps needs to simultaneously consider the impacts of molecular structure on the active layer morphology that can lead to the formation of appropriate crystalline sizes together with preferable face-on alignment in active layer to give high R_{sh} and then high V_{OC} . In addition, new fabrication techniques that can subtly optimize the morphology of blend film using ternary compositions are also beneficial for further improving the performance. It is generally believed that OSC-based IPVs have the best opportunity to satisfy the demanding on flexible panels. However, flexible OSCs still showed the relatively lower PCEs which need to significantly improve for practical applications. Because the reported stability tests are still limited, hence, OSCs-based IPVs also need to face the poor stability issue for the further progress in the near future.

Among these emerging photovoltaic materials, perovskites (e.g. $\text{CH}_3\text{NH}_3\text{PbI}_3$) are superior due to the high crystallinity for good charge transport, better spectral coverage and the low exciton binding energy. The best perovskite-based IPV with a PCE of 35% was reported with good stability by incorporation of an ionic liquid acting as both electron transport and protective layer to effectively passivate the surface of the perovskite film. This excellent result implies the bright prospect of perovskite for IPV application if the stability issue can be nicely solved. In addition, the developments of new hole- and/or electron-

transporting materials as well as interfacial materials to facilitate the exciton extraction efficiency, together with new inputs on fabrication processes to control the quality and size of perovskite crystals, and to improve the stability, and new device structures are essential and important as we consider applying perovskite for practical IPV applications. In spite of the high efficiency IPVs that can be achieved by Pb-based perovskites, the Pb issues on the environmental impacts are still under debating. In this regard, more research efforts on Pb-free perovskites for giving comparable efficiency should be strongly invested in the near future.

Overall, the steady improvements of the performance of various IPVs reveal this indoor light harvesting technology has the possibility for practical commercialization as sustainable power source. To reach to the final goal there are still some major challenges such as hysteresis effect in the current-voltage curves, poor morphology of active layers, low R_{sh} and high R_s and exciton recombination, waiting for feasible solutions from material developments, fabrication processes, and device architectures point of view. This review may benefit to create/generate innovative ideas for conquering these challenges.

Declaration of Competing Interest

The authors declare that they have no known competing financial interests or personal relationships that could have appeared to influence the work reported in this paper.

Acknowledgements

This work was supported by the Ministry of Science and Technology, Taiwan (MOST-107-2811-M-002-3137, 107-2113-M-002-019-MY3, 107-2119-M-131-001) and the RGC of Hong Kong [N_HKBU202/16]; and Hong Kong Baptist University [FRG2/17-18/078].

References

- [1] R.A. Potyrailo, Chem. Rev. 116 (2016) 11877–11923.
- [2] Y.K. Tan, S. Member, S.K. Panda, S. Member, IEEE Trans. Ind. Electron. 58 (2011) 4424–4435.
- [3] E.M. Compher, M.C. Gupta, W.C. Wilson, E.I. Madaras, Sol. Energy 85 (2011) 1899–1905.
- [4] J. Gubbi, R. Buyya, S. Marusic, M. Palaniswami, Future Gener. Comput. Syst. 29 (2013) 1645–1660.
- [5] L.D. Xu, W. He, S. Li, IEEE Trans. Ind. Inform. 10 (2014) 2233–2243.
- [6] I. Lee, K. Lee, Bus. Horiz. 58 (2015) 431–440.
- [7] Y. Aoki, Org. Electron. 48 (2017) 194–197.
- [8] I.C.L. Ng, S.Y.L. Wakenshaw, Int. J. Res. Mark 34 (2017) 3–21.
- [9] P.P. Ray, Comp. Inform. Sci. 30 (2018) 291–319.
- [10] B.L.R. Stojkoska, K.V. Trivodaliev, J. Clean. Prod. 140 (2017) 1454–1464.
- [11] F.-C. Chen, Adv. Opt. Mater. 7 (2019) 1800662.
- [12] P. Pérez-Higueras, J.P. Ferrer-Rodríguez, F. Almonacid, E.F. Fernández, Renew. Sustain. Energy Rev. 94 (2018) 143–153.
- [13] C.L. Cutting, M. Bag, D. Venkataraman, J. Mater. Chem. C 4 (2016) 10367–10370.
- [14] I. Mathews, G. Kelly, P.J. King, R. Frizzell, 2014 IEEE 40th Photovolt. Spec. Conf. PVSC vol 2014, (2014) 510–513.
- [15] Y. Li, N.J. Grabham, S.P. Beeby, M.J. Tudor, Sol. Energy 111 (2015) 21–29.
- [16] E. Coronel, A. Hultqvist, Prog. Photovolt Res. Appl. 17 (2009) 115–125.
- [17] T.E. Girish, Sol. Energy Mater. Sol. Cells 90 (2006) 2569–2571.
- [18] P. Bhatnagar, R.K. Nema, Renew. Sustain. Energy Rev. 23 (2013) 224–241.
- [19] J. Qi, Y. Zhang, Y. Chen, Renew. Energy 66 (2014) 337–345.
- [20] M.A. Green, Prog. Photovoltaics Res. Appl. 17 (2009) 183–189.
- [21] K. Yoshikawa, H. Kawasaki, W. Yoshida, T. Irie, K. Konishi, K. Nakano, T. Uto, D. Adachi, M. Kanematsu, H. Uzu, K. Yamamoto, Nat. Energy 2 (2017) 17032.
- [22] K.B. Hamrick, Am. Math. Mon. 103 (1996) 633–639.
- [23] V. Fthenakis, R.A. Meyers (Ed.), Encyclopedia of Sustainability Science and Technology, Springer, New York, NY, 2012.
- [24] B. O'Regan, M. Grätzel, Nature 353 (1991) 737–740.
- [25] K. Kakiage, Y. Aoyama, T. Yano, K. Oya, J.I. Fujisawa, M. Hanaya, Chem. Commun. 51 (2015) 15894–15897.
- [26] S. Burnside, S. Winkel, K. Brooks, V. Shklover, M. Grätzel, A. Hinsch, R. Kinderman, C. Bradbury, A. Hagfeldt, H. Pettersson, J. Mater. Sci. Mater. Electron. 11 (2000) 355–362.
- [27] Y. Cao, Y. Liu, S.M. Zakeeruddin, A. Hagfeldt, M. Grätzel, Joule 2 (2018) 1108–1117.
- [28] D. Newell, M. Duffy, R. Twohig, Proc. 29th Annu. IEEE Appl. Power Electron. Conf. Expo. (2014), pp. 3155–3159.
- [29] N.H. Reich, W.G.J.H.M. van Sark, W.C. Turkenburg, Renew. Energy 36 (2011)

- 642–647.
- [30] C.W. Tang, Appl. Phys. Lett. 48 (1986) 183–185.
- [31] B. Guo, W. Li, G. Luo, X. Guo, H. Yao, M. Zhang, J. Hou, Y. Li, W.Y. Wong, ACS Energy Lett. 3 (2018) 2566–2572.
- [32] H. Zhang, H. Yao, J. Hou, J. Zhu, J. Zhang, W. Li, R. Yu, B. Gao, S. Zhang, J. Hou, Adv. Mater. 30 (2018) 1800613.
- [33] S. Zhang, Y. Qin, J. Zhu, J. Hou, Adv. Mater. 30 (2018) 1800868.
- [34] Y. Firdaus, V.M. Le Corre, J.I. Khan, Z. Kan, F. Laquai, P.M. Beaujuge, T.D. Anthopoulos, Adv. Sci. 6 (2019) 1802028.
- [35] K. Feng, J. Yuan, Z. Bi, W. Ma, X. Xu, G. Zhang, Q. Peng, IScience 12 (2019) 1–12.
- [36] J. Yuan, Y. Zhang, L. Zhou, G. Zhang, H.-L. Yip, T.-K. Lau, X. Lu, C. Zhu, H. Peng, P.A. Johnson, M. Leclerc, Y. Cao, J. Ulanski, Y. Li, Y. Zou, Joule 3 (2019) 1140–1151.
- [37] H. Yao, Y. Cui, D. Qian, C.S. Ponseca, A. Honarfar, Y. Xu, J. Xin, Z. Chen, L. Hong, B. Gao, R. Yu, Y. Zu, W. Ma, P. Chabera, T. Pullerits, A. Yartsev, F. Gao, J. Hou, J. Am. Chem. Soc. 141 (2019) 7743–7750.
- [38] X. Che, Y. Li, Y. Qu, S.R. Forrest, Nat. Energy 3 (2018) 422–427.
- [39] Y. Cui, H. Yao, J. Zhang, T. Zhang, Y. Wang, L. Hong, K. Xian, B. Xu, S. Zhang, J. Peng, Z. Wei, F. Gao, J. Hou, Nat. Commun. 10 (2019) 2515.
- [40] B. Minnaert, P. Veelaert, Proc. SPIE 7722 (2010) 77221P.
- [41] B. Minnaert, P. Veelaert, Adv. Sci. Technol. 74 (2010) 170–175.
- [42] H.K.H. Lee, J. Wu, J. Barbé, S.M. Jain, S. Wood, E.M. Speller, Z. Li, F.A. Castro, J.R. Durrant, W.C. Tsui, J. Mater. Chem. A 6 (2018) 5618–5626.
- [43] J. Wang, K. Liu, L. Ma, X. Zhan, Chem. Rev. 116 (2016) 14675–14725.
- [44] S. Luo, W.A. Daoud, J. Mater. Chem. A 3 (2015) 8992–9010.
- [45] M.L. Petrus, J. Schlipf, C. Li, T.P. Gujar, N. Giesbrecht, P. Müller-Buschbaum, M. Thelakkat, T. Bein, S. Hüttner, P. Docampo, Adv. Energy Mater. 7 (2017) 1700264.
- [46] F. Wang, Y. Cao, C. Chen, Q. Chen, X. Wu, X. Li, T. Qin, W. Huang, Adv. Funct. Mater. 28 (2018) 1803753.
- [47] A.M. Askar, K. Shankar, J. Nanosci. Nanotechnol. 16 (2016) 5890–5901.
- [48] A. Kojima, K. Teshima, Y. Shirai, T. Miyasaka, J. Am. Chem. Soc. 131 (2009) 6050–6051.
- [49] N.J. Jeon, H. Na, E.H. Jung, T.Y. Yang, Y.G. Lee, G. Kim, H.W. Shin, S. Il Seok, J. Lee, J. Seo, Nat. Energy 3 (2018) 682–689.
- [50] M.M. Lee, J. Teuscher, T. Miyasaka, T.N. Murakami, H.J. Snaith, Science 338 (2012) 643–647.
- [51] C.Y. Chen, J.H. Chang, K.M. Chiang, H.L. Lin, S.Y. Hsiao, H.W. Lin, Adv. Funct. Mater. 25 (2015) 7064–7070.
- [52] M. Li, C. Zhao, Z.-K. Wang, C.-C. Zhang, H.K.H. Lee, A. Pockett, J. Barbé, W.C. Tsui, Y.-G. Yang, M.J. Carnie, X.-Y. Gao, W.-X. Yang, J.R. Durrant, L.-S. Liao, S.M. Jain, Adv. Energy Mater. 8 (2018) 1801509.
- [53] LEDtronics, CIE 1931 Chromaticity Diagram, URL: (2008) <http://www.ledtronics.com/html/1931ChromaticityDiagram.htm>.
- [54] Y. Ohno, M. Fein, Vision Experiment on White Light Chromaticity for Lighting, in: the 9th Biannual Joint Meeting of the CIE/USA and CNC/CIE, California Lighting Technology Center (CLTC), URL: <https://cltc.ucdavis.edu/sites/default/files/files/publication/2-yoshi-ohno-mira-fein-white-light-chromaticity-vision-experiment.pdf>.
- [55] H. Yin, J.K.W. Ho, S.H. Cheung, R.J. Yan, K.L. Chiu, X. Hao, S.K. So, J. Mater. Chem. A 6 (2018) 8579–8585.
- [56] Revolution Lighting Technologies, Inc, Tangled up in Blue: Unraveling the Effects of LED Lighting on Our Health and Safety, URL: Revolution Lighting Technologies, Inc., 2019, https://www.rvlti.com/wp-content/uploads/2017/08/AN009_Tangled-up-in-Blue.pdf.
- [57] Y.-M. Shang, G.-S. Wang, D.H. Sliney, C.-H. Yang, L.-L. Lee, Int. J. Ophthalmol. 10 (2017) 191–202.
- [58] F. Viénnot, E. Mahler, L. Serreault, M. Harrar, J. Ezraty, P. Pérignon, A. Bricoune, Discriminating colours under LED illumination, Proceedings of the 10th Congress of the International Colour Association, International Colour Association (AIC), (2019), pp. 33–36.
- [59] C.Y. Chen, Z.H. Jian, S.H. Huang, K.M. Lee, M.H. Kao, C.H. Shen, J.M. Shieh, C.L. Wang, C.W. Chang, B.Z. Lin, C.Y. Lin, T.K. Chang, Y. Chi, C.Y. Chi, W.T. Wang, Y. Tai, M. De Lu, Y.L. Tung, P.T. Chou, W.T. Wu, T.J. Chow, P. Chen, X.H. Luo, Y.L. Lee, C.C. Wu, C.M. Chen, C.Y. Yeh, M.S. Fan, J. De Peng, K.C. Ho, Y.N. Liu, H.Y. Lee, C.Y. Chen, H.W. Lin, C. Te Yen, Y.C. Huang, C.S. Tsao, Y.C. Ting, T.C. Wei, C.G. Wu, J. Phys. Chem. Lett. 8 (2017) 1824–1830.
- [60] L. Halonen, M. Puolakkka, M. Ayama, J. Bodrogi, E. Burini, D. Crawford, K. ChangSoon, O. DaPos, T. Goodman, N. Itoh, C. Knight, L. Leetzw, M. Rea, K. Sagawa, J. Schanda, F. Viénnot, S. Völker, L. Yandan, E. Yandek, Recommended System for Mesopic Photometry Based on Visual Performance: Technical Report (CIE 191:2010), Commission Internationale de l'Eclairage (CIE), 2010.
- [61] T. Goodman, T. Bergen, P. Blattner, Y. Ohno, J. Schanda, T. Uchida, The Use of Terms and Units in Photometry-Implementation of the CIE System for Mesopic Photometry (CIE TN 004:2016), Commission Internationale de l'Eclairage (CIE), 2016.
- [62] Commission Internationale de l'Eclairage (CIE), Characterization of the Performance of Illuminance Meters and Luminance Meters (ISO 19476:2014, CIE S 023/E:2013), International Organization for Standardization, 2014.
- [63] Commission Internationale de l'Eclairage (CIE), Colorimetry – Part 1: CIE Standard Colorimetric Observers (ISO 11664-1:2007, CIE S 014-1/E:2006), International Organization for Standardization, 2007.
- [64] E.F. Schubert, Light-emitting Diodes, 2 ed., Cambridge University Press, 2006.
- [65] M.S. Rea, Value Metrics for Better Lighting, SPIE Press Bellingham, WA, 2013.
- [66] H.K.H. Lee, Z. Li, J.R. Durrant, W.C. Tsui, Appl. Phys. Lett. 108 (2016) 253301.
- [67] N. Piva, F. Greco, M. Garbugli, A. Iacchetti, V. Mattoli, M. Caironi, Adv. Electron. Mater. 4 (2018) 1700325.
- [68] S.-S. Yang, Z.-C. Hsieh, M.L. Keshtov, G.D. Sharma, F.-C. Chen, Sol. RRL 1 (2017) 1700174.
- [69] B.P. Lechêne, M. Cowell, A. Pierre, J.W. Evans, P.K. Wright, A.C. Arias, Nano Energy 26 (2016) 631–640.
- [70] Y.-C. Liu, H.-H. Chou, F.-Y. Ho, H.-J. Wei, T.-C. Wei, C.-Y. Yeh, J. Mater. Chem. A 4 (2016) 11878–11887.
- [71] S. Mori, T. Gotanda, Y. Nakano, M. Saito, K. Todori, M. Hosoya, Jpn. J. Appl. Phys. 54 (2015) 071602.
- [72] Y.S. Tingare, N.S. Vinh, H.-H. Chou, Y.-C. Liu, Y.-S. Long, T.-C. Wu, T.-C. Wei, C.-Y. Yeh, Adv. Energy Mater. 7 (2017) 1700032.
- [73] Shenzhen Myledy Co., Ltd, LED Color Consistency, URL: (2017) <https://myledy.com/led-color-consistency/>.
- [74] J.A. Veitch, S.L. McColl, Light. Res. Technol. 27 (1995) 243–256.
- [75] L. Castaner, S. Silvestre, Modelling Photovoltaic Systems Using PSpice, John Wiley and Sons, 2002.
- [76] R. Stein, T. Ameri, P. Schilinsky, C. Waldauf, G. Dennler, M. Scharber, C.J. Brabec, Sol. Energy Mater. Sol. Cells 95 (2011) 3256–3261.
- [77] Japanese Industrial Standards Committee, General Rules of Recommended Lighting Levels (Amendment 1) [JIS Z 9110:2011], Japanese Industrial Standards Committee, 2011.
- [78] A. Ferrero, J.L. Velázquez, A. Pons, J. Campos, Opt. Express 26 (2018) 18633–18643.
- [79] Deutsches Institut für Normung (DIN), Klasseneinteilung Von Beleuchtungsstärkeund Leuchtdichtemessgeräte. DIN 5032 Lichtmessung. Teil 7 (Classification of Illuminance and Luminance Measuring Equipment. DIN Photometry. Part 7), DIN, 1985.
- [80] T. Goodman, G. Heidel, G. Muray, Y. Ohno, G. Sauter, J. Schanda, J. Steudtner, R. Young, Measurement of LEDs (CIE 127.2007), Commission Internationale de l'Eclairage (CIE), 2007.
- [81] Commission Internationale de l'Eclairage (CIE), Colorimetry – Part 2: CIE Standard Illuminants for Colorimetry (ISO 11664-2:2007(E)/CIE S 014-2/E:2006), International Organization for Standardization, 2007.
- [82] P. Csuti, B. Kránicz, J. Schanda, Comparison of the goodness of fit of photometers to the $V(\lambda)$ function using real LED spectra, CIE Expert Symposium on LED Light Sources: Physical Measurement and Visual and Photobiological Assessment (x026:2005), Commission Internationale de l'Eclairage (CIE), 2004, pp. 98–101.
- [83] R. Young, K. Muray, C. Jones, Quantifying photometric spectral mismatch uncertainties in LED measurements, Proceedings of the 2nd CIE Expert Symposium on LED Measurement, CIE x022:2001, Commission Internationale de l'Eclairage (CIE), (2001).
- [84] M. Clark, Spectral handheld light meters for accurate measurements of LED lighting, LED Event 2016, federatie van technologiebranches (FHI), 2016.
- [85] F. Sametoglu, Opt. Eng. 46 (2007) 093607.
- [86] T. Bergen, P. Blattner, Photometry standardization developments for OLEDs and LEDs, LED Professional Review vol 41, (2019), pp. 24–28 URL: https://www.ledprofessional.com/downloads/LpR41_716785.pdf.
- [87] I. Perre, Is measuring LEDs with a lux meter accurate? Professional Lighting Summit 2014, Institution of Lighting Professionals, (2014) URL: <https://www.slideshare.net/theipl/pls-2014-is-measuring-ledluminance-with-a-lux-meter-accurate>.
- [88] T. Pulli, T. Dönsberg, T. Poikonen, F. Manoocheri, P. Kärhä, E. Ikonen, Light Sci. Appl. 4 (2015) 1–7.
- [89] V. Shrotriya, G. Li, Y. Yao, T. Moriarty, K. Emery, Y. Yang, Adv. Funct. Mater. 16 (2006) 2016–2023.
- [90] National Institute of Standards and Technology (NIST), NIST Policy on Metrological Traceability, URL: (2018) <https://www.nist.gov/traceability/nist-policy-metrological-traceability>.
- [91] Y. Ohno, J. Res. Inst. Stand. Technol. 102 (1997) 323–331.
- [92] J.L. Gardner, J. Res. Inst. Stand. Technol. 109 (2004) 305–318.
- [93] J. Pan, Q. Li, Y. Zong, Y. Ohno, Measurement of Spectral Properties of Photometers and Colorimeters (CIE Div. 2 Reportship R2-38), Commission Internationale de l'Eclairage (CIE), 2011.
- [94] G. Eppeldauer, J. Gardner, T. Goodman, S. Kaplan, Y. Ohno, Palmer, T. Saito, G. Sauter, A. Sperling, S. Winter, Y. Zong, Spectral Responsivity Measurement of Detectors, Radiometers and Photometers (CIE 202:2011), Commission Internationale de l'Eclairage (CIE), 2011.
- [95] Gigahertz-Optik, Spectral Mismatch Correction Factor a^*/F^* , URL: (2012) <https://www.gigahertz-optik.de/en-us/service-and-support/knowledge-base/spectral-mismatch-factor-a-f>.
- [96] Commission Internationale de l'Eclairage (CIE), Test Method for LED Lamps, LED Luminaires and LED Modules (CIE S 025/E:2015), CIE, 2015.
- [97] PassMark Software, LEDBenchmark: FAQ - Comparison of LED and CFL Light Warm up Times, URL: (2013) <http://www.ledbenchmark.com/faq/CFL-LED-warm-up-time.html>.
- [98] W. Shockley, H.J. Queisser, J. Appl. Phys. 32 (1961) 510–519.
- [99] M. Freunek, M. Freunek, L.M. Reindl, IEEE J. Photovolt. 3 (2013) 59–64.
- [100] M. Freunek (Müller), M. Freunek, L.M. Reindl, IEEE J. Photovolt. 3 (2013) 1459–1464.
- [101] J. Halme, P. Mäkinena, Energy Environ. Sci. 12 (2019) 1274–1285.
- [102] A. Raj, D. Steinberg, J. Electrochem. Soc. 165 (2018) B3130–B3136.
- [103] O.A. Rosyid, AIP Conf. Proc. 1712 (2016) 020004.
- [104] M. Scharber, D. Mühlbacher, M. Koppe, P. Denk, C. Waldauf, A. Heeger, C. Brabec, Adv. Mater. 18 (2006) 789–794.
- [105] E. Zimmermann, P. Ehrenreich, T. Pfadler, J.A. Dorman, J. Weickert, L. Schmidt-Mende, Nat. Photonics 8 (2014) 669–672.
- [106] K. Emery, T. Moriarty, Accurate measurement of organic solar cell efficiency, Proc. SPIE 7052, Organic Photovoltaics IX, 70520D, 26 August (2008), <https://doi.org/10.1117/12.799606>.
- [107] A. Virtanen, H. Müllejans, E. Dunlop, Prog. Photovolt: Res. Appl. 19 (2011) 11–20.
- [108] S. Trost, K. Zilberman, A. Behrendt, A. Polywka, P. Görnn, P. Reckers, J. Maibach, T. Mayer, T. Riedl, Adv. Energy Mater. 3 (2013) 1437–1444.
- [109] J. Kim, G. Kim, Y. Choi, J. Lee, S. Heum Park, K. Lee, J. Appl. Phys. 111 (2012) 114511.

- [110] D. Chen, C. Zhang, Z. Wang, J. Zhang, S. Tang, W. Wei, L. Sun, Y. Hao, *Org. Electron.* 15 (2014) 3006–3015.
- [111] J. Symonowicz, M. Morawski, M. Dusza, P. Peksa, A. Sieradzki, F. Granek, *Org. Electron.* 52 (2018) 32–41.
- [112] W. Xu, R. Xia, T. Ye, L. Zhao, Z. Kan, Y. Mei, C. Yan, X.W. Zhang, W.Y. Lai, P.E. Keivanidis, W. Huang, *Adv. Sci.* 3 (2015) 1–7.
- [113] T. Kusumi, T. Kuwabara, K. Fujimori, T. Minami, T. Yamaguchi, T. Taima, K. Takahashi, T. Murakami, V.A.S.A. Rachmat, K. Marumoto, *ACS Omega* 2 (2017) 1617–1624.
- [114] R.B. Dunbar, B.C. Duck, T. Moriarty, K.F. Anderson, N.W. Duffy, C.J. Fell, A. Ho-Baillie, J. Kim, D. Vak, T. Duong, Y. Wu, K. Weber, A. Pascoe, Y.-B. Cheng, Q. Lin, P.L. Burn, R. Bhattacharjee, H. Wang, G.J. Wilson, *J. Mater. Chem. A* 5 (2017) 22542–22558.
- [115] C.M. Proctor, T.-Q. Nguyen, *Appl. Phys. Lett.* 106 (2015) 083301.
- [116] H. Yin, S. Chen, S.H. Cheung, H.W. Li, Y. Xie, S.W. Tsang, X. Zhu, S.K. So, *J. Mater. Chem. C* 6 (2018) 9111–9118.
- [117] M. Chegaar, A. Hamzaoui, A. Namoda, P. Petit, M. Aillerie, A. Herguth, *Energy Procedia* 36 (2013) 722–729.
- [118] P.-J. Ribeyron, *Nat. Energy* 2 (2017) 17067.
- [119] B. Minnaert, P. Veelaert, *Energies* 7 (2014) 1500–1516.
- [120] M.A. Green, K. Emery, Y. Hisikawa, W. Warta, E.D. Dunlop, *Prog. Photovoltaics Res. Appl.* 23 (2015) 805–812.
- [121] J. Zhao, A. Wang, M.A. Green, F. Ferrazza, *Appl. Phys. Lett.* 73 (1998) 1991–1993.
- [122] N.H. Reich, W. Van Sark, E. A. Alsema, S.Y. Kan, S. Silvester, A. Van Der Heide, R.W. Lof, R. Schropp, *20th Eur. Photovolt. Sol. Energy Conf.* (2005), pp. 4–7.
- [123] J. Peng, L. Lu, H. Yang, T. Ma, *Renew. Energy* 80 (2015) 316–323.
- [124] N.H. Reich, W.G.J.H.M. van Sark, E.A. Alsema, R.W. Lof, R.E.I. Schropp, W.C. Sinke, W.C. Turkenburg, *Sol. Energy Mater. Sol. Cells* 93 (2009) 1471–1481.
- [125] A. El Amrani, M. El Amraoui, A. El Abbassi, C. Messaoudi, *Superlattices Microstruct.* 75 (2014) 39–46.
- [126] M. Foti, C. Tringali, A. Battaglia, N. Sparta, S. Lombardo, C. Gerardi, *Sol. Energy Mater. Sol. Cells* 130 (2014) 490–494.
- [127] H. Aguas, T. Mateus, A. Vicente, D. Gaspar, M.J. Mendes, W.A. Schmidt, L. Pereira, E. Fortunato, R. Martins, *Adv. Funct. Mater.* 25 (2015) 3592–3598.
- [128] M.-H. Kao, C.-H. Shen, P. Yu, W.-H. Huang, Y.-L. Chueh, J.-M. Shieh, *Sci. Rep.* 7 (2017) 12706.
- [129] M.L. Tsai, D.S. Tsai, L. Tang, L.J. Chen, S.P. Lau, J.H. He, *ACS Nano* 11 (2017) 4564–4570.
- [130] M. Rasheduzzaman, P.B. Pillai, A.N.C. Mendoza, M.M. De Souza, *2016 10th Int. Symp. Commun. Syst. Networks Digit. Signal Process., IEEE*, (2016), pp. 1–6.
- [131] A. Teran, M. Dejarld, J. Hwang, W. Lim, J. Wong, D. Blaauw, Y. Lee, J. Millunchick, J. Phillips, *Device Res. Conf. - Conf. Dig. DRC* vol 48, (2014) 251–252.
- [132] A.S. Teran, S. Member, E. Moon, S. Member, W. Lim, S. Member, G. Kim, I. Lee, D. Blaauw, J.D. Phillips, S. Member, *IEEE Trans. Electron Devices* 63 (2016) 2820–2825.
- [133] A.S. Teran, J. Wong, W. Lim, G. Kim, Y. Lee, D. Blaauw, J.D. Phillips, *IEEE Trans. Electron Devices* 62 (2015) 2170–2175.
- [134] J. Russo, W. Ray, M.S. Litz, *Appl. Energy* 191 (2017) 10–21.
- [135] D.L. Bätzner, A. Romeo, H. Zogg, A.N. Tiwari, *Pvsec* (2001) 1–4.
- [136] V. Bermudez, A. Perez-Rodriguez, *Nat. Energy* 3 (2018) 466–475.
- [137] B. Minnaert, P. Veelaert, *Thin Solid Films* 519 (2011) 7537–7540.
- [138] B. Minnaert, P. Veelaert, *I-SUP 2010 Innov. Sustain. Prod. Proc.* (2010), pp. 8–12.
- [139] A. Mishra, M.K.R. Fischer, P. Bäuerle, *Angew. Chemie Int. Ed.* 48 (2009) 2474–2499.
- [140] J.-H. Yum, E. Baranoff, S. Wenger, M.K. Nazeeruddin, M. Grätzel, *Energy Environ. Sci.* 4 (2011) 842–857.
- [141] Y. Wu, W. Zhu, *Chem. Soc. Rev.* 42 (2013) 2039–2058.
- [142] M. Liang, J. Chen, *Chem. Soc. Rev.* 42 (2013) 3453–3488.
- [143] S. Chaurasia, C.-J. Liang, Y.-S. Yen, J.T. Lin, *J. Mater. Chem. C* 3 (2015) 9765–9780.
- [144] J. Zheng, K. Zhang, Y. Fang, Y. Zuo, Y. Duan, Z. Zhuo, X. Chen, W. Yang, Y. Lin, M.S. Wong, F. Pan, *ACS Appl. Mater. Interfaces* 7 (2015) 25341–25351.
- [145] B. Pashaei, H. Shahroosvand, M. Graetzel, M.K. Nazeeruddin, *Chem. Rev.* 116 (2016) 9485–9564.
- [146] M. Graetzel, *Acc. Chem. Res.* 42 (2009) 1788–1798.
- [147] D. Kumar, K.T. Wong, *Mater. Today Energy* 5 (2017) 243–279.
- [148] S.C. Pradhan, A. Hagfeldt, S. Soman, *J. Mater. Chem. A* 6 (2018) 22204–22214.
- [149] E. Gabrielson, H. Ellis, S. Feldt, H. Tian, G. Boschloo, A. Hagfeldt, L. Sun, *Adv. Energy Mater.* 3 (2013) 1647–1656.
- [150] H. Jiang, Y. Wu, A. Islam, M. Wu, W. Zhang, C. Shen, H. Zhang, E. Li, H. Tian, W.H. Zhu, *ACS Appl. Mater. Interfaces* 10 (2018) 13635–13644.
- [151] Y. Wu, W.H. Zhu, S.M. Zakeeruddin, M. Grätzel, *ACS Appl. Mater. Interfaces* 7 (2015) 9307–9318.
- [152] S. Kim, J.K. Lee, S.O. Kang, J. Ko, J.H. Yum, S. Fantacci, F. De Angelis, D. Di Censo, K. Nazeeruddin, M. Grätzel, *J. Am. Chem. Soc.* 128 (2006) 16701–16707.
- [153] L.Y. Lin, C.H. Tsai, K.T. Wong, T.W. Huang, L. Hsieh, S.H. Liu, H.W. Lin, C.C. Wu, S.H. Chou, S.H. Chen, A.I. Tsai, J. Org. Chem. 75 (2010) 4778–4785.
- [154] K.R. Justin Thomas, A. Venkateswararao, C.-P. Lee, K.-C. Ho, *Dyes Pigm.* 123 (2015) 154–165.
- [155] A. Venkateswararao, K.R. Justin Thomas, C.P. Lee, K.C. Ho, *Asian J. Org. Chem.* 4 (2015) 69–80.
- [156] J.H. Chen, C.H. Tsai, S.A. Wang, Y.Y. Lin, T.W. Huang, S.F. Chiu, C.C. Wu, K.T. Wong, *J. Org. Chem.* 76 (2011) 8977–8985.
- [157] D. Joly, M. Godfroy, L. Pellejà, Y. Kervella, P. Maldivi, S. Narbey, F. Oswald, E. Palomares, R. Demadrille, *J. Mater. Chem. A* 5 (2017) 6122–6130.
- [158] C.Y. Lo, D. Kumar, S.H. Chou, C.H. Chen, C.H. Tsai, S.H. Liu, P.T. Chou, K.T. Wong, *ACS Appl. Mater. Interfaces* 8 (2016) 27832–27842.
- [159] K.R.J. Thomas, A. Venkateswararao, R. Balasaravanan, C.T. Li, K.C. Ho, *Dyes Pigm.* 165 (2019) 182–192.
- [160] H.C. Ting, C.H. Tsai, J.H. Chen, L.Y. Lin, S.H. Chou, K.T. Wong, T.W. Huang, C.C. Wu, *Org. Lett.* 14 (2012) 6338–6341.
- [161] H.J. Snaith, *Adv. Funct. Mater.* 20 (2010) 13–19.
- [162] F. De Rossi, T. Pontecorvo, T.M. Brown, *Appl. Energy* 156 (2015) 413–422.
- [163] V. Stockhausen, L. Andrade, D. Ivanou, B. Stannowski, A. Mendes, *Sol. Energy Mater. Sol. Cells* 191 (2019) 451–458.
- [164] H. Pettersson, T. Gruszecki, *Sol. Energy Mater. Sol. Cells* 70 (2001) 203–212.
- [165] H. Lindström, A. Holmberg, E. Magnusson, L. Malmqvist, A. Hagfeldt, *J. Photochem. Photobiol. A* 145 (2001) 107–112.
- [166] L. Cojocaru, S. Uchida, K. Tamaki, P.V.V. Jayaweera, S. Kaneko, J. Nakazaki, T. Kubo, H. Segawa, *Sci. Rep.* 7 (2017) 11790.
- [167] C.H. Huang, Y.W. Chen, C.M. Chen, *ACS Appl. Mater. Interfaces* 10 (2018) 2658–2666.
- [168] C.P. Lee, C.A. Lin, T.C. Wei, M.L. Tsai, Y. Meng, C.T. Li, K.C. Ho, C.I. Wu, S.P. Lau, J.H. He, *Nano Energy* 18 (2015) 109–117.
- [169] G. Kapil, Y. Ogomi, S.S. Pandey, T. Ma, S. Hayase, *J. Nanosci. Nanotechnol.* 16 (2016) 3183–3187.
- [170] B. Boro, B.M. Rajbongshi, S.K. Samdarshi, *J. Mater. Sci. Mater. Electron.* 27 (2016) 9929–9940.
- [171] S. Venkatesan, I.P. Liu, W.N. Hung, H. Teng, Y.L. Lee, *Chem. Eng. J.* 367 (2019) 17–24.
- [172] T.K. Chang, Y. Chi, *RSC Adv.* 7 (2017) 42013–42023.
- [173] J.M. Ji, H. Zhou, H.K. Kim, *J. Mater. Chem. A* 6 (2018) 14518–14545.
- [174] K.S.K. Reddy, Y.C. Chen, C.C. Wu, C.W. Hsu, Y.C. Chang, C.M. Chen, C.Y. Yeh, *ACS Appl. Mater. Interfaces* 10 (2018) 2391–2399.
- [175] K.S.K. Reddy, Y.-C. Liu, H.-H. Chou, K. Kala, T.-C. Wei, C.-Y. Yeh, *ACS Appl. Mater. Interfaces* 10 (2018) 39970–39982.
- [176] S.M. Feldt, E.A. Gibson, E. Gabrielson, L. Sun, G. Boschloo, A. Hagfeldt, *J. Am. Chem. Soc.* 132 (2010) 16714–16724.
- [177] C.L. Wang, P.T. Lin, Y.F. Wang, C.W. Chang, B.Z. Lin, H.H. Kuo, C.W. Hsu, S.H. Tu, C.Y. Lin, *J. Phys. Chem. C* 119 (2015) 24282–24289.
- [178] M.C. Tsai, C.L. Wang, C.W. Chang, C.W. Hsu, Y.H. Hsiao, C.L. Liu, C.C. Wang, S.Y. Lin, C.Y. Lin, *J. Mater. Chem. A* 6 (2018) 1995–2003.
- [179] H.H. Chou, Y.C. Liu, G. Fang, Q.C. Cao, T.C. Wei, C.Y. Yeh, *ACS Appl. Mater. Interfaces* 9 (2017) 37786–37796.
- [180] M. Freitag, J. Teuscher, Y. Saygili, X. Zhang, F. Giordano, P. Liska, J. Hua, S.M. Zakeeruddin, J.E. Moser, M. Grätzel, A. Hagfeldt, *Nat. Photonics* 11 (2017) 372–378.
- [181] Y. Liu, Y. Cao, W. Zhang, M. Stojanovic, M.I. Dar, P. Péchy, Y. Saygili, A. Hagfeldt, S.M. Zakeeruddin, M. Grätzel, *Angew. Chemie Int. Ed.* 57 (2018) 14125–14128.
- [182] C.H. Chen, P.T. Chou, T.C. Yin, K.F. Chen, M.L. Jiang, Y.J. Chang, C.K. Tai, B.C. Wang, *Org. Electron.* 59 (2018) 69–76.
- [183] J. Wang, Z. Chai, S. Liu, M. Fang, K. Chang, M. Han, L. Hong, H. Han, Q. Li, Z. Li, *Chem. - A Eur. J.* 24 (2018) 18032–18042.
- [184] I.P. Liu, W.H. Lin, C.M. Tseng-Shan, Y.L. Lee, *ACS Appl. Mater. Interfaces* 10 (2018) 38900–38905.
- [185] S. Venkatesan, I.-P. Liu, C.-W. Li, C.-M. Tseng-Shan, Y.-L. Lee, *ACS Sustain. Chem. Eng.* 7 (2019) 7403–7411.
- [186] I. Juhasz junger, D. Werner, E. Schwenzfeier-Hellkamp, A. Ehrmann, *Optik (Stuttgart)*, 177 (2019) 8–12.
- [187] M.B. Desta, N.S. Vinh, C. Pavan Kumar, S. Chaurasia, W.T. Wu, J.T. Lin, T.C. Wei, E. Wei-Guang Diau, *J. Mater. Chem. A* 6 (2018) 13778–13789.
- [188] S.H. Park, A. Roy, S. Beaupré, S. Cho, N. Coates, J.S. Moon, D. Moses, M. Leclerc, K. Lee, A.J. Heeger, *Nat. Photonics* 3 (2009) 297–303.
- [189] M.L. Jiang, J. Wen, Z. Chen, W.-H. Tsai, T. Lin, T.J. Chow, Y.J. Chang, *ChemSusChem* (2019), <https://doi.org/10.1002/cssc.201900505> asap.
- [190] Y.-J. Cheng, S.-H. Yang, C.-S. Hsu, *Chem. Rev.* 109 (2009) 5868–5923.
- [191] G. Denner, M.C. Scharber, C.J. Brabec, *Adv. Mater.* 21 (2009) 1323–1338.
- [192] M.T. Dang, L. Hirsch, G. Wantz, *Adv. Mater.* 23 (2011) 3597–3602.
- [193] A. Mishra, P. Bäuerle, *Angew. Chemie Int. Ed.* 51 (2012) 2020–2067.
- [194] Y. Lin, Y. Li, X. Zhan, *Chem. Soc. Rev.* 41 (2012) 4245–4272.
- [195] L. Dou, J. You, Z. Hong, Z. Xu, G. Li, R.A. Street, Y. Yang, *Adv. Mater.* 25 (2013) 6642–6671.
- [196] Y. Huang, E.J. Kramer, A.J. Heeger, G.C. Bazan, *Chem. Eng. Rev.* 114 (2014) 7006–7043.
- [197] L. Lu, T. Zheng, Q. Wu, A.M. Schneider, D. Zhao, L. Yu, *Chem. Eng. Rev.* 115 (2015) 12666–12731.
- [198] K.A. Mazzio, C.K. Luscombe, *Chem. Soc. Rev.* 44 (2015) 78–90.
- [199] A. Venkateswararao, S.W. Liu, K.T. Wong, *Mater. Sci. Eng. R Rep.* 124 (2018) 1–57.
- [200] R. Xue, J. Zhang, Y. Li, Y. Li, *Small* 14 (2018) 1801793.
- [201] P. Vincent, S.C. Shin, J.S. Goo, Y.J. You, B. Cho, S. Lee, D.W. Lee, S.R. Kwon, K.B. Chung, J.J. Lee, J.H. Bae, J.W. Shim, H. Kim, *Dyes Pigm.* 159 (2018) 306–313.
- [202] J.S. Goo, J.H. Lee, S.C. Shin, J.S. Park, J.W. Shim, J. Mater. Chem. A 6 (2018) 23464–23472.
- [203] B.R. Lee, J.S. Goo, Y.W. Kim, Y.J. You, H. Kim, S.K. Lee, J.W. Shim, T.G. Kim, *J. Power Sources* 417 (2019) 61–69.
- [204] Y.W. Kim, J.S. Goo, T.H. Lee, B.R. Lee, S.C. Shin, H. Kim, J.W. Shim, T.G. Kim, *J. Power Sources* 424 (2019) 165–175.
- [205] S.-S. Yang, Z.-C. Hsieh, M.L. Keshtov, G.D. Sharma, F.-C. Chen, *Sol. RRL* 1 (2017) 1770143.
- [206] K. Tada, *Phys. Status Solidi* 214 (2017) 1700018.
- [207] S.C. Shin, P. Vincent, J.H. Bae, J.J. Lee, M. Nam, D.H. Ko, H. Kim, J.W. Shim, *Dyes Pigm.* 163 (2019) 48–54.
- [208] D. Landerer, D. Bahro, H. Röhm, M. Koppitz, A. Mertens, F. Manger, F. Denk, M. Heidinger, T. Windmann, A. Colsmann, *Energy Technol.* 5 (2017) 1936–1945.
- [209] R. Singh, S.-C. Shin, H. Lee, M. Kim, J.W. Shim, K. Cho, J. Lee, *Chem. Eur. J.* 25 (2019) 6154–6161.
- [210] M. Nam, H.Y. Noh, J.H. Kang, J. Cho, B.K. Min, J.W. Shim, D.H. Ko, *Nano Energy*

- 58 (2019) 652–659.
- [211] S.Y. Park, Y. Li, J. Kim, T.H. Lee, B. Walker, H.Y. Woo, J.Y. Kim, *ACS Appl. Mater. Interfaces* 10 (2018) 3885–3894.
- [212] S.C. Shin, C.W. Koh, P. Vincent, J.S. Goo, J.H. Bae, J.J. Lee, C. Shin, H. Kim, H.Y. Woo, J.W. Shim, *Nano Energy* 58 (2019) 466–475.
- [213] Y. You, C.E. Song, Q.V. Hoang, Y. Kang, J.S. Goo, D. Ko, J. Lee, W.S. Shin, J.W. Shim, *Adv. Funct. Mater.* (2019) 1901171.
- [214] R. Arai, S. Furukawa, Y. Hidaka, H. Komiya, T. Yasuda, *ACS Appl. Mater. Interfaces* 11 (2019) 9259–9264.
- [215] C.H. Chen, H.C. Ting, Y.Z. Li, Y.C. Lo, P.H. Sher, J.K. Wang, T.L. Chiu, C.F. Lin, I.S. Hsu, J.H. Lee, S.W. Liu, K.T. Wong, *ACS Appl. Mater. Interfaces* 11 (2019) 8337–8349.
- [216] Z. Yu, L. Sun, *Adv. Energy Mater.* 5 (2015) 1500213.
- [217] K. Kawata, K. Tamaki, M. Kawaraya, *J. Photopolym. Sci. Technol.* 28 (2015) 415–417.
- [218] I. Raifuku, Y. Ishikawa, S. Ito, Y. Uraoka, *J. Phys. Chem. C* 120 (2016) 18986–18990.
- [219] C.Y. Chen, W.H. Lee, S.Y. Hsiao, W.L. Tsai, L. Yang, H.L. Lin, H.J. Chou, H.W. Lin, *J. Mater. Chem. A* 7 (2019) 3612–3617.
- [220] D. Bi, W. Tress, M.I. Dar, P. Gao, J. Luo, C. Renévier, K. Schenk, A. Abate, F. Giordano, J.-P. Correa Baena, J.-D. Decoppet, S.M. Zakeeruddin, M.K. Nazeeruddin, M. Grätzel, A. Hagfeldt, *Sci. Adv.* 2 (2016) e1501170.
- [221] S. Gangala, R. Misra, *J. Mater. Chem. A* 6 (2018) 18750–18765.
- [222] Z. Hawash, L.K. Ono, Y. Qi, *Adv. Mater. Interfaces* 5 (2018) 1700623.
- [223] L. Kegelmann, P. Tockhorn, C.M. Wolff, J.A. Márquez, S. Caicedo-Dávila, L. Korte, T. Unold, W. Lövenich, D. Neher, B. Rech, S. Albrecht, *ACS Appl. Mater. Interfaces* 11 (2019) 9172–9181.
- [224] H.-S. Kim, C.-R. Lee, J.-H. Im, K.-B. Lee, T. Moehl, A. Marchioro, S.-J. Moon, R. Humphry-Baker, J.-H. Yum, J.E. Moser, M. Grätzel, N.-G. Park, *Sci. Rep.* 2 (2012) 591.
- [225] X. Li, D. Bi, C. Yi, J.-D. Décoppel, J. Luo, S.M. Zakeeruddin, A. Hagfeldt, M. Grätzel, *Science* 353 (2016) 58–62.
- [226] H.D. Pham, Z. Wu, L.K. Ono, S. Manzhos, K. Feron, N. Motta, Y. Qi, P. Sonar, *Adv. Electron. Mater.* 3 (2017) 1700139.
- [227] Y. Wang, H. Qu, C. Zhang, Q. Chen, *Sci. Rep.* 9 (2019) 459.
- [228] G. Lucarelli, F. Di Giacomo, V. Zardetto, M. Creatore, T.M. Brown, *Nano Res.* 10 (2017) 2130–2145.
- [229] F. Di Giacomo, V. Zardetto, G. Lucarelli, L. Cinà, A. Di Carlo, M. Creatore, T.M. Brown, *Nano Energy* 30 (2016) 460–469.
- [230] J. Dagar, S. Castro-Hermosa, M. Gasbarri, A.L. Palma, L. Cina, F. Matteocci, E. Calabro, A. Di Carlo, T.M. Brown, *Nano Res.* 11 (2018) 2669–2681.
- [231] J. Dagar, S. Castro-Hermosa, G. Lucarelli, F. Cacialli, T.M. Brown, *Nano Energy* 49 (2018) 290–299.
- [232] S.S.-Y. Juang, P.-Y. Lin, Y.-C. Lin, Y.-S. Chen, P.-S. Shen, Y.-L. Guo, Y.-C. Wu, P. Chen, *Front. Chem.* 7 (2019) 1–9.
- [233] R. Cheng, C.-C. Chung, H. Zhang, Z. Zhou, P. Zhai, Y.-T. Huang, H. Lee, S.-P. Feng, *Small* 15 (2019) 1804465.
- [234] H.K.H. Lee, J. Barbé, S.M.P. Meroni, T. Du, C.-T. Lin, A. Pockett, J. Troughton, S.M. Jain, F. De Rossi, J. Baker, M.J. Carnie, M.A. McLachlan, T.M. Watson, J.R. Durrant, W.C. Tsoi, *Sol. RRL* 3 (2019) 1800207.
- [235] F. De Rossi, J.A. Baker, D. Beynon, K.E.A. Hooper, S.M.P. Meroni, D. Williams, Z. Wei, A. Yasin, C. Charbonneau, E.H. Jewell, T.M. Watson, *Adv. Mater. Technol.* 3 (2018) 1800156.



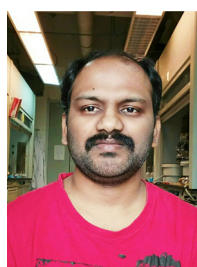
Shu K. SO obtained his bachelor degree from Hamilton College and PhD in Physics from Cornell University. In Cornell, he did research on surface physics and chemistry of small molecules on metal and semiconductor surfaces. He was a postdoctoral fellow in the Chemistry Department of the University of Toronto where he used scanning tunneling microscope to study surface photochemistry. In 1992, he joined the Department of Physics, Hong Kong Baptist University. He is now the Acting Head and a Professor of Physics, and is heading the Department in the focused research areas in advanced materials and in biological physics. His major research interest is in the physics and the chemistry of thin film materials including transport and defect study of organic films, fabrication of organic solar cells and thin film transistors, surface and optical spectroscopies of materials, and pulsed laser deposition. He has made notable contributions to the carrier transport study of organic and polymeric thin films for OLEDs and OPV applications, and the study of defects in organic semiconductors and perovskite materials. His recent interests are in the niche applications of OPV cells in, e.g., for indoor light harvesting.



Shun-Wei Liu received the Ph.D. degree from the Graduated Institute of Photonics and Optoelectronics, National Taiwan University, in 2010. After this, he joined the Institute of Chemistry, Academia Sinica, Taiwan, and served as a Special Research Technician. In 2011, he joined the Department of Electronic Engineering, Ming Chi University of Technology (MCUT). He is currently a full professor as well as the director of the organic electronics research center in MCUT. His current research interests are in the area of understanding the fundamental physics of organic materials and their relevance in novel optoelectronic devices, i.e., organic photovoltaic driven image devices, ITO-free organic light-emitting diodes, transparent electronics, and thin-film encapsulation technology. Until now, Dr. Liu has published over 130 international journal papers. He also won a “Ta-Yao Wu Memorial Award” and “Award for Excellent Contribution in Technology Transfer” in Taiwan (2018). The details of S. -W. Liu's research team can be found on the website (<https://organicelectronics.mcut.edu.tw/>).



Ken-Tsung Wong is Professor at Department of Chemistry, National Taiwan University; Adjunct Faculty, Institute of Atomic and Molecular Science, Academia Sinica, Taiwan. Ken obtained his B. S. degree from Catholic Fu-Jen University in 1989, Ph.D. degree from National Taiwan University in 1993. Ken conducted his postdoctoral researches at University of Illinois at Urbana-Champaign in 1995–1996 and Université Louis Pasteur, Strasbourg in 1996–1998 before he joined the Department of Chemistry at National Taiwan University as an assistant professor in 1998. Ken was promoted to an associate professor four years later (2002) and professor in 2006. Ken established a strong interdisciplinary research program engaging domestic and international collaborations. His research mainly focuses on the molecular design and synthesis of novel π -conjugated organic materials for optoelectronic applications such as OLED, electrogenerated chemiluminescence (ECL), solid-state light-emitting electrochemical cells (LECs), organic photovoltaic devices, and organic materials for nano-structures and their applications.



Addanki Venkateswararao obtained his B. Sc. from Acharya Nagarjuna University, India in 2005, M.Sc. from same university in 2007, and then Ph.D. from Indian Institute of Technology Roorkee, India in 2015 under the supervision of Prof. K.R. Justin Thomas. He worked as a research associate at Indian Institute of Chemical Technology, India and moved to Ming Chi University of Technology, Taiwan as a postdoctoral fellow. In 2018, he joined the research laboratory led by Prof. Ken-Tsung Wong at National Taiwan University, Taiwan, as a postdoctoral fellow. His current research involves in organic light emitting diodes, dye sensitized solar cells, organic solar cells, and perovskite solar cells.



Johnny K. W. HO is a PhD student in Physics under the supervision of Professor S. K. So at Hong Kong Baptist University. He will graduate with a doctoral degree in 2020. His research interests include electrical properties of organic semiconductors and organometallic hybrid perovskite materials as well as device physics of thin film transistors and organic photovoltaics. His current investigation focus is on indoor organic photovoltaics and perovskite transistors.